MINISTÉRIO DA CIÊNCIA, TECNOLOGIA E INOVAÇÕES
INSTITUTO NACIONAL DE PESQUISAS ESPACIAIS

sid.inpe.br/mtc-m21d/2022/10.31.17.37-TDI

EXTREME PRECIPITATION EVENTS ON THE EAST COAST OF BRAZIL'S NORTHEAST: OBSERVATIONAL, NUMERICAL, AND DIAGNOSTIC ANALYSIS

Saulo Barros Costa

Doctorate Thesis of the Graduate Course in Meteorology, guided by Dr. Dirceu Luis Herdies, approved in November 10, 2022.

URL of the original document:
<http://urlib.net/8JMKD3MGP3W34T/47T8KPS>

INPE
São José dos Campos
2022

PUBLISHED BY:

Instituto Nacional de Pesquisas Espaciais - INPE
Coordenação de Ensino, Pesquisa e Extensão (COEPE)
Divisão de Biblioteca (DIBIB)
CEP 12.227-010
São José dos Campos - SP - Brasil
Tel.:(012) 3208-6923/7348
E-mail: pubtc@inpe.br

MINISTÉRIO DA CIÊNCIA, TECNOLOGIA E INOVAÇÕES
INSTITUTO NACIONAL DE PESQUISAS ESPACIAIS

sid.inpe.br/mtc-m21d/2022/10.31.17.37-TDI

EXTREME PRECIPITATION EVENTS ON THE EAST COAST OF BRAZIL'S NORTHEAST: OBSERVATIONAL, NUMERICAL, AND DIAGNOSTIC ANALYSIS

Saulo Barros Costa

Doctorate Thesis of the Graduate Course in Meteorology, guided by Dr. Dirceu Luis Herdies, approved in November 10, 2022.

URL of the original document:
<http://urlib.net/8JMKD3MGP3W34T/47T8KPS>

INPE
São José dos Campos
2022

Cataloging in Publication Data

Costa, Saulo Barros.

C823e Extreme precipitation events on the east coast of brazil's northeast: observational, numerical, and diagnostic analysis / Saulo Barros Costa. – São José dos Campos : INPE, 2022.

xxiv + 101 p. ; (sid.inpe.br/mtc-m21d/2022/10.31.17.37-TDI)

Thesis (Doctorate in Meteorology) – Instituto Nacional de Pesquisas Espaciais, São José dos Campos, 2022.

Guiding : Dr. Dirceu Luis Herdies.

1. WRF configurations. 2. Weather analyses. 3. Natural disasters. I.Title.

CDU 551.509:504.4

MINISTÉRIO DA CIÊNCIA, TECNOLOGIA E INOVAÇÕES

INSTITUTO NACIONAL DE PESQUISAS ESPACIAIS

DEFESA FINAL DE TESE SAULO BARROS COSTA
BANCA Nº283/2022 , REGISTRO 139580/2017

No dia 10 de novembro de 2022, as 09h00, Videoconferência, o(a) aluno(a) mencionado(a) acima defendeu seu trabalho final (apresentação oral seguida de arguição) perante uma Banca Examinadora, cujos membros estão listados abaixo. O(A) aluno(a) foi **APROVADO(A)** pela Banca Examinadora, por unanimidade, em cumprimento ao requisito exigido para obtenção do Título de Doutor em Meteorologia. **O trabalho precisa da incorporação das correções sugeridas pela Banca e revisão final pelo(s) orientador(es).**

Título:" Extreme precipitation events on the east coast of Brazil's Northeast: observational, numerical, and diagnostic analysis ".

Membros da Banca

Dr. Dirceu Luis Herdies - Presidente - INPE
Dr. Luis Gustavo Gonçalves de Gonçalves - Membro Interno - INPE
Dr. Silvio Nilo Figueroa Rivero - Membro Interno - INPE
Dr. Pedro Leite da Silva Dias - Membro Externo - USP
Dr. Helber Gomes Barros - Membro Externo - UFAL
Dr. Diego Oliveira de Souza - Membro Externo - CEMADEM

Documento assinado eletronicamente por **Dirceu Luís Herdies**, **Pesquisador**, em 18/11/2022, às 10:11 (horário oficial de Brasília), com fundamento no § 3º do art. 4º do Decreto nº 10.543, de 13 de novembro de 2020.

Documento assinado eletronicamente por **Pedro Leite da silva dias (E)**, **Usuário Externo**, em 18/11/2022, às 17:14 (horário oficial de Brasília), com fundamento no § 3º do art. 4º do Decreto nº 10.543, de 13 de novembro de 2020.

Documento assinado eletronicamente por **Helber Barros Gomes (E)**, **Usuário Externo**, em 21/11/2022, às 16:34 (horário oficial de Brasília), com fundamento no § 3º do art. 4º do Decreto nº 10.543, de 13 de novembro de 2020.

Documento assinado eletronicamente por **Silvio Nilo Figueroa Rivero**, **Pesquisador**, em 21/11/2022, às 18:01 (horário oficial de Brasília), com fundamento no § 3º do art. 4º do Decreto nº 10.543, de 13 de novembro de 2020.

Documento assinado eletronicamente por **Diego Oliveira de Souza**, **Tecnologista**, em 24/11/2022, às 13:41 (horário oficial de Brasília), com fundamento no § 3º do art. 4º do Decreto nº 10.543, de 13 de novembro de 2020.

Documento assinado eletronicamente por **LUIS GUSTAVO GONÇALVES DE GONÇALVES (E)**, **Usuário Externo**, em 07/12/2022, às 11:21 (horário oficial de Brasília), com fundamento no § 3º do art. 4º do Decreto nº 10.543, de 13 de novembro de 2020.

A autenticidade deste documento pode ser conferida no site https://sei.mcti.gov.br/verifica.html, informando o código verificador **10579330** e o código CRC **4DA02BE5**.

Referência: Processo nº 01340.009008/2022-67 SEI nº 10579330

"*Poverty is both a driver and consequence of disasters and the processes that further disaster risk-related poverty are permeated with inequality. Socio-economic inequality is likely to continue to increase and with it disaster risk for those countries, communities, households, and businesses that have only limited opportunities to manage their risks and strengthen their resilience. The geography of inequality expresses itself at all scales: between regions and countries, within countries and inside cities and localities.*"

United Nations

"I dedicate it to my family and colleagues at CEMADEN. I also dedicate it to all those who believe in the transforming power of knowledge and that a strong country is built by strengthening public institutions, investment in science and technology, social inclusion policies, and increased access to health and quality education. I dedicate to the people who protect themselves and their surroundings by getting vaccinated, to those who understand the limitation of natural resources and, therefore, the importance of preserving them, to those who respect other people's way of loving, to those who understand the need for a better distribution of land, to those who preach respect for native peoples and also to those who do not burden God with questions of customs nor use His name to fight what they cannot understand. Finally, I dedicate to all the Brazilian researchers who are naturally highly resilient and maintain the hope that better days are ever closer."

ACKNOWLEDGEMENTS

This work had the collaboration and enthusiasm of many people. One of the main ones was Dr. Dirceu Herdies, my advisor. This work was only possible thanks to Dirceu's guidance and incentive. Thank you for the countless meetings, your constant availability, and the many scientific discussions and personal advice. Thank you for completely understanding my necessities and limitations; thank you for believing in my capacity even in the moments that I, taken by the students' insecurity, came to doubt. Thank you for pushing me forward and for the many opportunities offered. Thank you for your respect and consideration along this path. I am sure that this partnership does not end here.

Thanks to Dr. Diego Souza from CEMADEN for his help with the numerical simulations. All simulations were performed in the system he acquired, designed, and maintained, without which this work would not have been completed.

I thank the Graduate Program in Meteorology at INPE (PGMET) for the opportunity. I thank all the secretaries and librarians for their cordiality, dedication, and professionalism.

This project did not receive direct support from any funding agency, but its importance will not be neglected. Thanks to the Coordination of Superior Level Staff Improvement (CAPES), the National Council for Scientific and Technological Development (CNPQ), and all the state research support agencies for supporting the research at INPE, contributing to national development, and enduring. Thanks to the Agência Pernambucana de Águas e Clima (APAC) for the availability of radar data. Thanks to the National Center for Monitoring and Early Warning of Natural Disasters (CEMADEN), my home, especially Dr. Marcelo Seluchi, for the encouragement and incentive.

Thank you to the people who have supported and missed me the most on this journey, my dearest Nina and Fiona. I hope to fill them with pride and promise to be more present. Only you know and fully understand all the challenges and trials we have been through. Thank you, Anna Laura, for your logistical support, emotional and spiritual support, and various reconsiderations. Without you, this work would be impossible.

My deepest thanks to the two most important people for realizing this work, José and Nina, my parents. When I was approved in PGMET, already with the obligations of a constituted family and without exclusive dedication to research, they were the ones who left the distant and warm Maceió and came to São José dos Campos to save me, and I, at 35 years old, returned to my parent's home. Thank you for taking care of my family and me, the housework, the financial support, the organizing of our routine, and providing the ideal conditions and structures for family life and well-being in which I could dedicate myself as much as possible to this work. Your care and unconditional love inspire me and make me want to be better and better. I hope I can live up to your dedication when you need to and can repay you for all this love.

ABSTRACT

The Northeast of Brazil (NEB) is the region with the highest number of municipal decrees of emergency declarations caused by weather events in the period from 2013 to 2022 and with the highest rate of natural disasters per risk area. In the NEB, the city of Recife and its metropolitan region are the biggest localities with populations in risk areas. Focusing on this region, three years of natural disaster alert issuance data, from 2017 to 2019, were used to analyze and characterize severe rainfall events in the eastern state of Pernambuco. The disaster records could be grouped into 24 extreme severe weather systems that were analyzed in detail with satellite, weather model, radar, and rain gauge data. Among the natural disaster events analyzed, four events of extreme precipitation were chosen for simulations with the WRF model in high resolution (2.5 km) and diagnostics analyses. First, a set of configurations of the model was tested, including 11 microphysics (MPH) schemes, 9 planetary boundary layer (PBL) schemes, 6 cumulus (CUM), and 5 surface (SFC) schemes. Then, through diagnostic analysis, the conditional instability, the moisture supply at low levels, and the support of the medium and high levels in storm formation were verified. The observational analysis indicated that the warnings were concentrated during the rainy season and in a narrow coastal belt. The main systems responsible for the heavy precipitation were the ITCZ and high pressure on the surface that blocked the trade winds and favored convection. Small-sized multicell were the types of radar reflectivity cores lasting longer than 24 hours that caused the heaviest rainfall in the region. The model's configurations were verified by 298 rain gauges with hourly registrations through statistical metrics such as bias, MSE, standard deviation, and Pearson's correlation, and demonstrated that the MPH schemes of Thompson Aerosol-Aware and NSSL + CCN, ACM2, MYJ for the PBL, KFCuP for CUM, and RUC for SFC were considered the best. All the cases were better with CUM parametrizations turned on. In all cases, diagnostics analyses highlighted the strong moisture flux convergence at the low levels, the presence of wind shear on the middle layer, weak cyclonic vorticity advection at high levels, and CAPE values around 1500 J/kg, in addition to an inverse relationship between wind shear action and CAPE values. This work is part of the national strategy for monitoring, diagnosing, and modeling information that can minimize or even prevent damage caused by severe precipitation events.

Keywords: WRF configurations. Weather analyses. Natural disasters.

EVENTOS DE PRECIPITAÇÃO EXTREMA NA COSTA LESTE DO NORDESTE DO BRASIL: ANÁLISE OBSERVACIONAL, NUMÉRICA E DIAGNÓSTICA

RESUMO

O Nordeste do Brasil (NEB) é a região com maior número de decretos municipais de emergência causados por eventos meteorológicos no período de 2013 a 2022 e com a maior taxa de desastres naturais por área de risco. No NEB, a cidade de Recife e sua região metropolitana são as maiores localidades com população em áreas de risco. Com foco sobre essa região, três anos de dados de envio de alertas de desastres naturais, de 2017 a 2019, foram usados para analisar e caracterizar eventos de chuva severa no leste do estado de Pernambuco. Os registros de desastres puderam ser agrupados em 24 casos de sistemas de tempo severo que foram analisados em detalhes com dados de satélite, de modelo, de radar e de pluviômetros. Entre os eventos de desastres naturais analisados, quatro ventos de precipitação extrema foram escolhidos para simulações com o modelo WRF com alta resolução (2,5 km) e análises diagnósticas. Primeiro, um conjunto de configurações do modelo foram testadas, incluindo 11 esquemas de microfísica (MPH), 9 esquemas de camada limite planetária (PBL), 6 esquemas de cumulus (CUM) e 5 esquemas de superfície (SFC). Em seguida, através das análises diagnósticas, a instabilidade condicional, o fornecimento de umidade em baixos níveis e o suporte de médio e altos níveis na formação das tempestades foram verificados. As análises observacionais indicaram que os alertas se concentraram durante a estação chuvosa e na estreita faixa litorânea. Os principais sistemas responsáveis pelas fortes precipitações foram a ZCIT e uma alta pressão na superfície responsável pelo bloqueio dos ventos alísios e favorecer a convecção. Multicélulas de tamanho pequeno foram os tipos de núcleos de refletividade de radar com duração superior a 24 horas que mais causaram chuvas fortes na região. As configurações do modelo foram verificadas através de 298 pluviômetros com registros horários de chuva através de métricas estatísticas como o viés, MSE, desvio padrão e a correlação de Pearson e demonstraram que os esquemas de MPH de Thompson Aerosol-Aware e NSSL + CCN, de PBL ACM2 e MYJ, KFCuP para CUM e RUC para SFC foram considerados os melhores. Todos os casos foram melhores com a parametrização de CUM ligada. Em todos os casos, as análises diagnósticas destacaram a forte convergência do fluxo de umidade em baixos níveis, a presença de cisalhamento do vento na média camada, fraca advecção de vorticidade ciclônica em altos níveis e valores de CAPE em torno de 1500 J/kg, além de uma relação inversa entre o cisalhamento do vento e os valores de CAPE. Esse trabalho se insere dentro da estratégia nacional de monitoramento, diagnóstico e modelagem de informações que podem minimizar ou até mesmo prevenir danos causados por eventos de chuva severa.

Palavras-chave: Configurações do WRF. Análise de tempo. Desastres naturais.

LIST OF FIGURES

Pág.

LIST OF TABLES

Pág.

LIST OF ACRONYMS AND ABBREVIATIONS

ACM2	Asymmetric Convective Model
AL	Alagoas
AMO	Atlantic Multidecadal Oscillation
APAC	Agência Pernambucana de Águas e Clima
BA	Bahia
BEWS	Brazilian Early Warning System
CAPE	Convective Available Potential Energy
CAPPI	Constant Altitude Plan Position Indicator
CCN	Cloud Condensation Nuclei
CE	Ceará
CEMADEN	Centro Nacional de Monitoramento e Alertas de Desastres Naturais
CENAD	Centro Nacional de Gerenciamento de Riscos e Desastres
CNM	Confederação Nacional de Municípios
CEPED[1]	Centro Universitário de Estudos e Pesquisas sobre Desastres
CINE	Convective Inhibition
EL	Equilibrium Level
EtaFerr	Eta (Ferrier)
EWD	Easterly Wave Disturbances
G3	Grell-3
GF	Grell-Freitas
GFS	Global Forecast System
HLF	High Layer Flow
HPS	High Pressure on the Surface
HYSPLIT	Hybrid Single-Particle Lagrangian Integrated Trajectory
IBGE	Instituto Brasileiro de Geografia e Estatistica
INPE	Instituto Nacional de Pesquisas Espaciais
ITCZ	Intertropical Convergence Zone
KainF	Kain-Fritsch

[1] Later this acronym was changed, currently it means “Centro de Estudos e Pesquisas em Engenharia e Defesa Civil”.

KFCuP	Kain-Fritsch-Cumulus Potential
LAI	Leaf Area Index
LCL	Lifting Condensation Level
LFC	Level of Free Convection
LSM	Land-Surface Model
MA	Maranhão
MCS	Mesoscale Convective System
MFC	Moisture Flux Convergence
MLF	Medium Layer Flow
MULT	Multicellular
MYJ	Mellor-Yamada-Janjic scheme
MYNN2	Mellor-Yamada Nakanishi and Niino Level 2.5
MYNN3	Mellor-Yamada Nakanishi and Niino Level 3
NASA	North Atlantic Subtropical Anticyclone
NCEP	National Centers for Environmental Prediction
NEB	Northeast of Brazil
MJO	Madden–Julian oscillation
NoahMP	Noah Multi-Physics
NOAA	National Oceanic and Atmospheric Administration
NSSL	National Severe Storms Laboratory
NTiedtke	New Tiedtke Scheme
NWP	Numerical Weather Prediction
PB	Paraíba
PBL	Planetary Boundary Layer
PE	Pernambuco
PI	Piauí
PPI	Plan Position Indicator
PurdLin	Purdue Lin
QNSE	Quasi-Normal Scale Elimination
RE	Relative Error
READY	Real-time Environmental Applications and Display sYstem
RHI	Range-Height Indicator
RMS	Root Mean Square Error
RN	Rio Grande do Norte

RUC	Rapid Update Cycle
SASA	South Atlantic Subtropical Anticyclone
SE	Sergipe
ShinH	Shin-Hong scheme
UTCV	Upper Tropospheric Cyclonic Vortices
SMS3D	Subgrid Mixing Scheme
SST	Sea Surface Temperature
TDS	Thermal Diffusion Scheme
TEMF	Total Energy - Mass Flux
TpsonAA	Thompson Aerosol-Aware
UCM	Urban Canopy Model
UNI	Unicellular
WDM6	WRF Single-Moment 6-class
WDM7	WRF Double-Moment 7-class
WRF	Weather Research and Forecasting
WSM5	WRF Single-Moment 5-class
WSM6	WRF Single-Moment 6-class
WSM7	WRF Single-Moment 7-class
YSU	Yonsei University Scheme

SUMMARY

Pág.

1 INTRODUCTION

Natural disasters include all geophysical, meteorological, and climate events like earthquakes, volcanic activity, landslides, drought, wildfires, storms, and flooding, which can cause loss of life or property and kill globally on average 45,000 people per year (RITCHIE; ROSER, 2014). In South America, between 1960 and 2009, 60% of deaths due to natural disasters were associated with earthquakes and volcanic activity and around 32% were related to meteorological events (HIDALGO NUNES, 2011). However, when the number of individuals affected is analyzed instead of the number of deaths, the vast majority of non-fatal victims (88%) are the most affected by climate or severe weather phenomena. According to the last World Risk Report (ALEKSANDROVA et al., 2021), a report that classifies 181 countries based on their potential to be subjected to extreme events, Brazil ranks 116th, which does not classify it as one of the most vulnerable countries to suffer from extreme events. Meanwhile, despite being a country that does not suffer from a high recurrence of tropical cyclones on its coastline and is not hit by major earthquakes, Brazil constantly suffers from prolonged droughts, floods, flash floods, and landslides (ASSIS DIAS et al., 2018).

Brazil's historic socioeconomic development is characterized by different uses and occupations of the land, which reveals a heterogeneous population distribution of its territory. These processes of disorderly occupation, when exposed to natural climate variability and the natural susceptibility of the regions, are subject to occurrences of disasters connected to landslides and floods (ASSIS DIAS et al., 2018), which in turn, are the types of disasters that cause the most deaths in Brazil (CEPED, 2012). Numerous studies have investigated the occurrence of floods, flash floods, and landslide episode, motivated by severe weather events capable of providing large rainfall totals (AVELAR et al., 2013; LUIZA et al., 2013; ÁVILA et al., 2016; MARENGO; ESPINOZA, 2016; METODIEV et al., 2018; ESPINOZA et al., 2021).

Observational evidence that extreme hydrometeorological events, responsible for significant precipitation accumulations, have become more frequent and intense in recent decades is a reality (SMITHSON, 2002). Extreme events are also components of natural climate variability and their quasi-periodicity and intensity, whether natural or induced by human activities, may change (FIELD et al., 2012). Such phenomena can impact

society depending on the existence of vulnerabilities at the site, which highlights the importance of the social development component in the characterization of natural disasters (MARCHEZINI et al., 2018).

From a physical perspective, Brazil is more easily affected by disasters of this nature due to its location in the tropical region (DEBORTOLI et al., 2017), where latent heat release is the primary energy source for the meteorological systems. This release occurs in association with convective cloud systems, although much precipitation also comes from stratiform cloud regions within mesoscale systems. More broadly, there is a strong interaction among cumulus convection, the mesoscale, and large-scale circulations in tropical areas. Furthermore, the distribution of diabatic heating in the tropics is influenced by variations in sea surface temperature, which in turn, is strongly influenced by the atmospheric circulations. Therefore, understanding tropical circulations requires consideration of equatorial wave dynamics, interactions between cumulus convection and mesoscale circulations with large-scale and ocean-atmosphere interactions (HOLTON; HAKIM, 2013).

The Northeast of Brazil (NEB) is widely affected by prolonged drought, flooding, and landslide events. The high population density in urban areas is the main determinant of vulnerability to natural hazards in the region, largely driven by the poor land use and planning that characterize Brazilian cities. Despite the importance of drought events, severe rainfall events have the potential to affect all segments of society, impacting health, education, housing, the economy, and the provision of basic services (MATIAS RIBEIRO et al., 2021). A study conducted by the World Bank indicates that the disaster-related costs of only four major events that occurred between 2008 and 2011 totaled approximately R$15.3 billion (TORO et al., 2014). Of these 4 events, 2 were located on the east coast of the NEB. In the context of climate change, the eastern portion of the NEB is signaled as one of the most affected regions due to its high vulnerability and exposure (DEBORTOLI et al., 2017; MARENGO et al., 2021). The main metropolitan regions, tourist resorts, and critical infrastructure in NEB are in this region.

In an attempt to mitigate the action of extreme rainfall events, several initiatives worldwide have been created to attenuate material losses and primarily human losses (UNDRR, 2013). In this context, the meteorological and hydrological services are central

to forecasting the most varied types of extreme events (WMO, 2013). In Brazil, an initiative to try mitigating episodes of severe rainfall was the creation of the National Center for Monitoring and Early Warning of Natural Disasters (CEMADEN, acronym in Portuguese) (ALVALÁ et al., 2019) with the primary mission of anticipating the occurrence of severe rainfall events in the previously monitored municipalities by issuing natural disaster warnings. CEMADEN currently uses a weather radar network with more than 40 radars, operates more than 4,000 rain gauges, and has around one thousand soil moisture sensors and hydrological stations distributed throughout the country (HORITA; DE ALBUQUERQUE; MARCHEZINI, 2018). Since 2011, CEMADEN has sent out more than 19,000 flood, flash flood, and landslide warnings throughout Brazil. Among the main means of monitoring the action of heavy rainfall are the use of surface and upper-air maps, radar and meteorological satellites, numerical weather modeling, and continuous weather analysis (AHRENS; SAMSON, 2011).

1.1 Motivation

The NEB is the region with the highest number of municipal ordinances of abnormalities due to severe weather events in the period from 2013 to 2022 (until April 05) and it is the region with the highest rate of events per risk area (CEMADEN, 2019; CNM, 2022). The metropolitan region of the city of Recife is the region with the highest population coverage in risk areas and the second highest in number of people in risk areas (IBGE, 2018). The eastern part of the state of Pernambuco is influenced by several synoptic and mesoscale systems capable of developing into large thunderstorms causing heavy precipitation events. These characteristics of high regional susceptibility and the possibility of severe rainfall episodes were determining factors for the choice of this region in this study.

1.2 Purpose

The objective of this work is, based on the warnings issued by CEMADEN and the history of occurrence of extreme precipitation events with high social impact, to identify and analyze the main mechanisms in rainfall events that trigger large rainfall totals on the east coast of the NEB, more specifically the eastern part of the state of Pernambuco. To this end, this research seeks to answer the following questions:

1) What are the main synoptic and mesoscale systems associated with severe rainfall on the east coast of the NEB?

2) What are the main characteristics of severe rainfall, for both rain rates and total accumulations, based on rain gauge and radar observations?

3) From a numerical modeling standpoint, what is the most suitable model configuration for the region?

4) How is the behavior of meteorological variables associated with severe rainfall events in the region?

To answer these questions, we used three years of data from warnings issued with occurrence records, which in turn were grouped according to the acting meteorological system and subsequently selected four cases for numerical simulation with the Weather Research and Forecasting (WRF) model and analysis of the meteorological parameters associated with the formation, intensification, and dissipation of severe thunderstorms. In this way, we sought to collaborate with the following specific objectives:

1) To contribute to the synoptic and mesoscale climatology of severe rainfall events in the region through rain gauge and radar data;

2) Identify the physical schemes in the WRF model, specifically the schemes that most impact rainfall production (cloud microphysics, planetary boundary layer, cumulus, and surface), best suited for the region;

3) Describe the behavior of meteorological variables associated with severe storms, such as atmospheric instability, moisture supply, and lifting mechanisms.

Thus, this work has the following structure: Chapter 2 presents a review of the main synoptic and mesoscale systems active in the NEB, a review of the main features of the microphysics, planetary boundary layer, cumulus and surface layer physical schemes used in the WRF model and finally a review of the main meteorological parameters used to describe severe storms, Chapter 3 presents the methodology and data used in the research, Chapter 4 shows the results of the synoptic climatology and the main mesoscale

features found, Chapter 5 describes the best model settings found for the four extreme events, Chapter 6 shows the analysis of the meteorological variables for the four simulated severe rainfall events, and Chapter 7 summarizes the conclusions and suggests research for future work.

2 LITERATURE REVIEW

2.1 Synoptic and mesoscale systems in the NEB

The variability in rainfall distribution in the NEB is pronounced. In the north of the region, the rainy season occurs mainly between March and April; in the south, the rains occur mainly during the period from December to February; in the eastern part of the region, the rainy season is from May to July (RAO; DE LIMA; FRANCHITO, 1993). Its rainfall regime results from the complex interaction between the relief, the geographic position, the nature of its surface and the acting pressure systems (KAYANO; ANDREOLI, 2009). The main precipitation mechanisms are conditioned by the influence of the South Atlantic Subtropical Anticyclone (SASA) and North Atlantic Subtropical Anticyclone (NASA) (HASTENRATH, 1991), the action of the Intertropical Convergence Zone (ITCZ) (WALISER; GAUTIER, 1993), cold fronts (KOUSKY, 1979), Upper Tropospheric Cyclonic Vortices (UTCV) (KOUSKY; GAN, 1981), the Easterly Wave Disturbances (EWD) (GOMES et al., 2015) and by the effects of sea and land breezes (MOLION; BERNARDO, 2002) (Figure 2.1). This complexity is reflected in rainfall's great spatial, seasonal, and interannual variability.

SASA and NASA are semi-permanent persistent high-pressure systems that spend most of the year in subtropical latitudes. They are characterized by anticyclonic wind circulation, subsidence, and divergence near the surface (HASTENRATH, 1991). The SASA presents seasonal variability retracting to the east during the summer and extending over southeastern Brazil during the winter, where, on the NEB coast, it contributes to the intensification of easterly runoff and trade winds that converge over the coast and favor precipitation (REBOITA et al., 2019). NASA presents a more irregular behavior but is responsible for the northeast trade winds. The convergence between the southeast and northeast trade winds favors the ITCZ, the upward movements, and the consequent formation of precipitation and follows the areas where the sea surface temperature (SST) is higher. Studies that considered the SST anomaly in the Pacific and Atlantic oceans showed a positive relationship between increased rainfall in the eastern NEB with a warm pool in the southwest Atlantic (UVO et al., 1998; HOUNSOU-GBO et al., 2019).

Figure 2.1 – Main synoptic systems in the NEB.

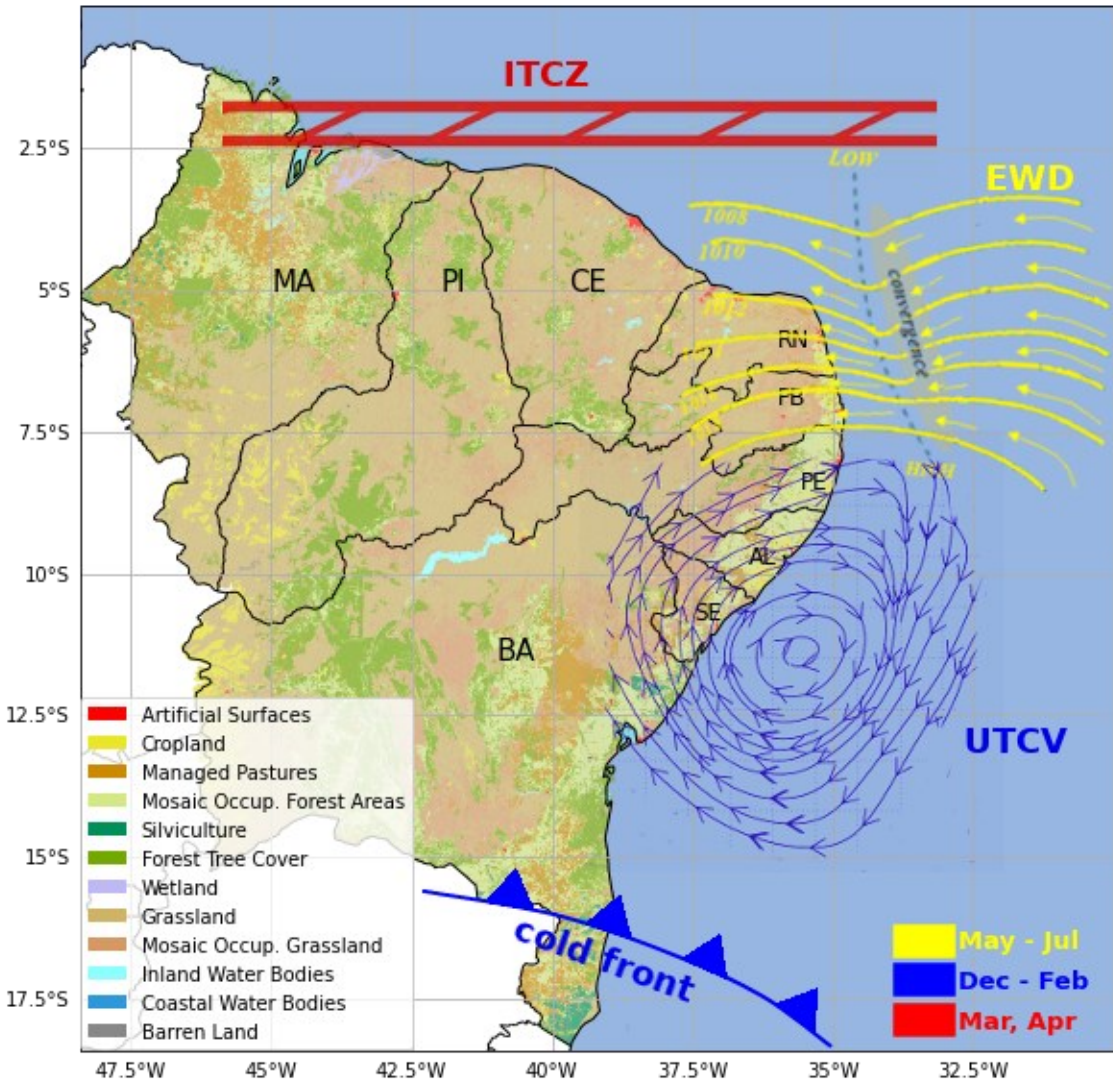

Schematic representation of the main meteorological systems acting in the NEB according to the months of the year. The position of the systems in the figure indicates the possibility of their occurrence in the indicated region according to the months of the year, not excluding the possibility of occurrence in nearby regions. Cold fronts and ITCZ can extend throughout the troposphere; EWDs typically occur in the low troposphere, and UTCVs at high levels. The political division of the states in the Northeast region: BA – Bahia; SE – Sergipe; AL – Alagoas; PE – Pernambuco; PB – Paraíba; RN – Rio Grande do Norte; CE – Ceará; PI – Piauí; MA – Maranhão. Land use and occupation, according to IBGE (2020).

The ITCZ establishes itself under the equatorial trough and is an upward branch of the Hadley cell. Thus it is perceived not as a transient phenomenon but an important part of the general circulation of the atmosphere and shows significant time variabiity in

intensity, position and orientation. This permanent low-pressure feature marks the meteorological equator where the trade winds, filled with heat and moisture from the surface, converge to form a zone of increased convection, cloudiness, and precipitation (FLETCHER, 1945; WALISER; GAUTIER, 1993) and it is modulated by the Madden–Julian oscillation (MJO) and local instabilities (FERREIRA; SCHUBERT, 1997). The favored moisture transport and increased convection are important for the rainfall regime in the NEB, which in turn has been studied by several authors (MOURA; SHUKLA, 1981; RAO; MARQUES, 1984; MARENGO et al., 2012; CORREIA FILHO et al., 2019). According to Uvo et al. (1998), the longer permanence of the ITCZ in its northernmost or southernmost position determines the quality of the rainy season in the northern NEB. In this region, rainfall is probably abundant if its migration northward begins in late April and early May. Thus, the portions of the north of Maranhão and Piauí, the entire states of Ceará and Rio Grande do Norte, and the hinterlands of Paraíba and Pernambuco are the sections that receive most of the ITCZ influence in Brazil. In these areas, maximum precipitation occurs in March and April (MELO; CAVALCANTI; SOUZA, 2009).

A frontal system is a transition zone between two air masses with different densities, temperatures, and humidity (AHRENS; HENSON, 2019). The displacement of cold fronts, when colder air advances over warmer air, occurs from higher latitudes toward lower latitudes. In South America, near central Argentina, cold fronts occur almost weekly and decrease their frequency toward the equator, being little observed in southern Bahia, where, on average, about 5 to 10 systems reach 15°S each year (KOUSKY, 1979; CAVALCANTI; KOUSKY, 2003). Even acting with less periodicity in the southern NEB, these systems and their remnants are largely responsible for the total accumulated precipitation observed from November to March in this sector.

The eastern NEB is primarily influenced by UTCVs, EWDs, and sea and land breeze circulations. UTCVs are a closed cyclonic circulation at high-tropospheric levels, with a cold core where good weather occurs, presenting a direct thermal circulation between the center and its periphery, where usually is intense convective activity (KOUSKY; GAN, 1981). The tropical vortices, common in the NEB and adjacent Atlantic Ocean, occur more frequently from December to February, are persistent, with a lifetime that can exceed 10 days in duration, and therefore can favor/inhibit precipitation in the regions

under the influence of its periphery/center, respectively (DE MORAIS; GAN; YOSHIDA, 2021).

EWDs are disturbances, most widely perceived in the wind field, caused by the westward motion of a low tropospheric trough that occur at tropical latitudes in the vicinity of the equator around the world (DUNN, 1940; GOMES et al., 2015; AHRENS; HENSON, 2019). They are widely studied in the Tropical Atlantic region because of their importance for the rainfall regime in West Africa and for monitoring the storms that occur in this region, as tropical storms and occasional hurricanes are formed from these systems. In Brazil, they can reach the northern and eastern coasts of the NEB, interact with the local circulation to increase convergence at low levels and cause heavy rainfall, contributing to at least 60% of the rainfall that occurs on the eastern coast of the NEB from April to August (TORRES; FERREIRA, 2011; GOMES et al., 2019).

Land-sea breezes are shallow cells of direct thermal circulation ruled by the horizontal pressure gradient configured due to the heating difference between the surfaces of the continent and the ocean. Many coastal areas in the NEB have maximum convective activity at nighttime due to the convergence between ocean outflow and the land breeze. Other areas may have a diurnal maximum due to the development and advection of the sea breeze up to 300 km inland (KOUSKY, 1980). In the NEB east coast, this circulation is mainly associated with the zonal wind, presents a penetration in the continent between one and two degrees meridional and the maximum/minimum of its daily cycle, which represents a potential land/sea breeze, occurs around 07h00UTC/19hUTC (DE SOUZA; OYAMA, 2017).

2.2 Model setup

The numerical weather prediction (NWP) equations models are solved at different grid points on the model as a discretized approximation to the partial derivatives through, finite differencing, finite volume differencing (when the dynamical and thermodynamical properties are integrated in strcutured or non-structured volumes), Galerkian methods (finite elements and spectral methods) (FLETCHER, 1984), on a regular grid or unstructured grid, like the new generation models. However, many processes are difficult to describe completely, especially if they occur at scales smaller than the model's resolution. For that, parameterization processes are used to represent by

approximation, as well as possible, the behavior of particles based on physical laws and empirical observations (GETTELMAN; ROOD, 2016). In that way, models depend on various physical packages, some of which use approximations for relatively small processes compared to the model grid. Therefore, atmospheric characteristics can vary greatly, and the optimal combination of these physical packages varies by region (JEWORREK; WEST; STULL, 2021).

In atmospheric modeling, precipitation processes are fundamentally associated with cloud microphysics parameterizations, which govern the formation, growth and dissipation of cloud particles (KESSLER, 1969); cumulus parameterizations, representing a series of functions, for example, vertical distribution of heating/cooling and drying/moistening, convection mass transport, generation of the liquid and ice phases of water, interactions with the planetary boundary layer (PBL), interactions with radiation, and mechanical interactions with the mean flow (ARAKAWA, 2004); PBL parameterizations, that can modulate the representation of turbulent mixing in the lower troposphere through the kinematic and thermodynamic vertical profiles that directly influence the buoyancy representation and vertical wind shear, in addition to the evolution of precipitation (HONG; NOH; DUDHIA, 2006; COHEN et al., 2015); and land surface parameterization, that control heat and moisture fluxes of the soil and provide the model with the inputs of heat, moisture and ground radiation that affect the input variables for other parameterizations and which, despite being less investigated in NWP sensitivity studies, play an important role in the diurnal precipitation cycle (WONG; ROMINE; SNYDER, 2020; JEWORREK; WEST; STULL, 2021).

2.2.1 Cloud microphysics schemes

The microphysical processes that govern cloud particle formation, growth, and dissipation on small scales are central to how moist convection develops and evolves (STENSRUD, 2007). Two important aspects of the cloud microphysics parameterizations are the number of changing water phases (Figure 2.2) and the number of different interactions between cloud and precipitation particles that must be considered since these shapes and sizes influence how the particles interact with each other (Figure 2.3).

The main types of cloud microphysics particles observed are cloud droplets, raindrops, ice crystals, aggregates, sleet, and ice particles. Liquid cloud droplets form when water

saturation exceeds above freezing to about – 40 °C. However, the formation of cloud droplets depends on the presence of small-hygroscopic particles that constitute the cloud condensation nuclei (CCN). Its rapid growth depends on processes such as collision and coalescence. Since cloud droplets coexist in a wide size range, collision and coalescence processes intensify, and depending on the efficiency of this process, raindroplets are formed. Ice crystals and aggregates may form when the temperature within the cloud is below freezing. However, this freezing may not occur immediately and evidence suggests the coexistence of liquid droplets and ice crystals between 0 and –40°C with the need for the presence of an ice nucleus (as CCNs are required for cloud droplet formation).

Figure 2.2 – Representation of the number of changing water phases for a microphysics scheme.

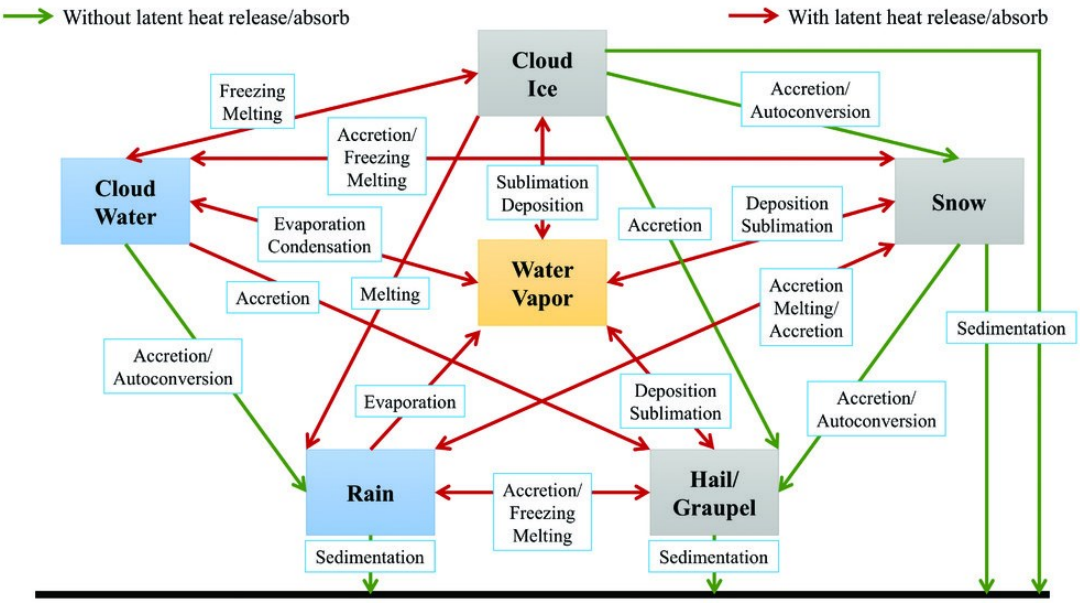

The yellow box indicates prognostic water vapor, the blue boxes indicate prognostic liquid-phase water species, and the gray boxes indicate prognostic solid-phase water species. Red arrows indicate processes involving heating/cooling from phase changes, while green arrows indicate conversion and sedimentation processes.

Source: Zhou et al. (2019).

Ice crystals are typically observed starting at temperatures of –15°C and there are three main forms: columns, plates, and dendrites (Figure 2.3). They can grow by the Bergeron-Findeisen process, which occurs due to saturation vapor pressure concerning water is higher than saturation vapor pressure with respect to ice, any cloud that is saturated with respect to water is supersaturated with respect to ice, as ice crystals grow by vapor

deposition they reduce the environmental supersaturation with respect to water until the air becomes subsaturated and liquid drops begin to evaporate, this evaporation then increases the supersaturation with respect to ice, and causes ice crystal growth (STENSRUD, 2007). The coalescing collision process also acts on the ice crystals producing the aggregates.

Figure 2.3 – The ice crystal morphology diagram.

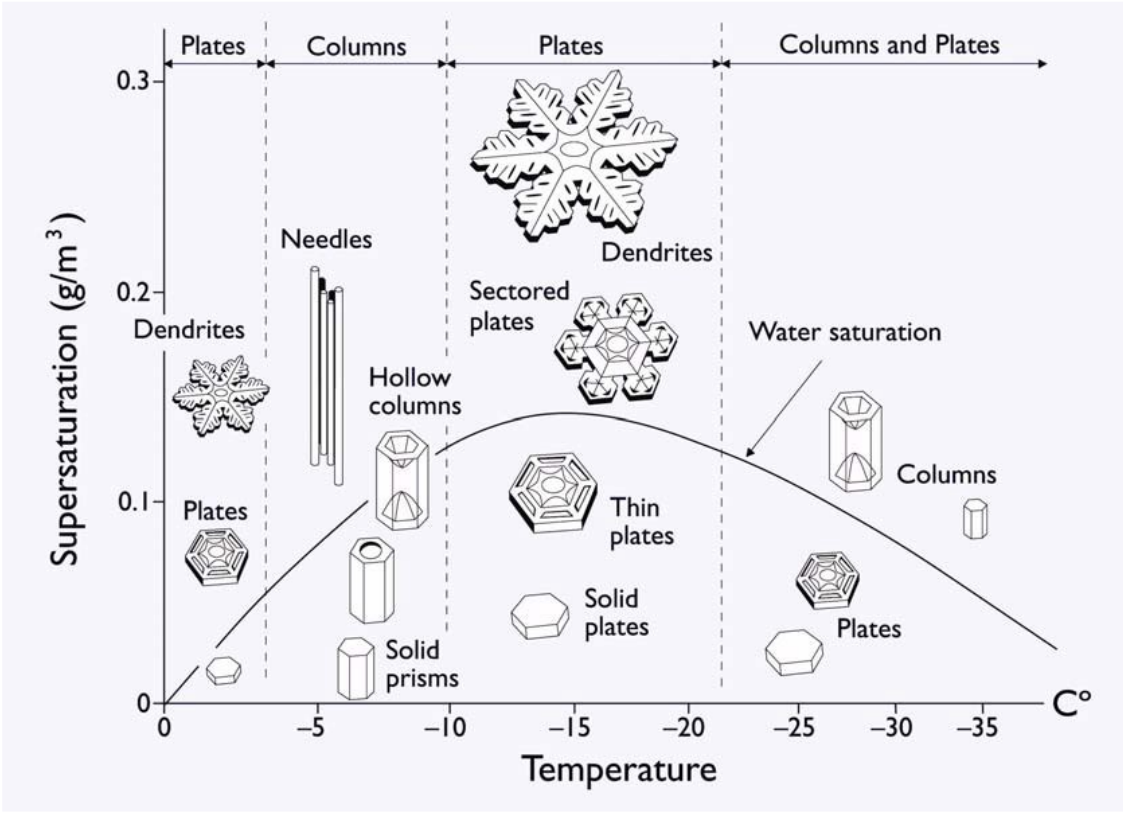

How the morphology of ice crystals growing from water vapor in air at a pressure of one bar changes with temperature and supersaturation.

Source: Libbrecht (2008).

Rime ice particles, graupel, and hail occur as ice crystals collide and coalesce with supercooled cloud droplets at environmental temperatures below freezing. The ice particle is a rimed when the features of the original ice particle can be distinguished and graupel when the opposite occurs. As graupel particles fall through the liquid cloud, they continue to grow by riming and in cases of extreme riming hailstones are formed.

Bulk microphysical models have been used to represent the spectrum of hydrometeors through a distribution function, such as an exponential or gamma-type function. In the

models that only one moment of the distribution is predicted (usually mixing ratio) are called single-moment schemes, while the other moments are diagnosed or prescribed. Schemes that use two moments in the hydrometeor distribution, mixing ratio and the concentration number, are called double – moments scheme (MEYERS et al., 1997). Prediction of two moments of the distribution allows more degrees of freedom of the hydrometeor spectra for each category, improving the prediction of complex microphysical processes.

The equations that govern the evolution of the microphysical variables all follow a similar structure:

$$\frac{\partial \chi}{\partial t} = -\hat{u} \cdot \vec{\nabla}\chi + \frac{1}{\rho}\frac{\partial(\rho V \chi)}{\partial z} + S_\chi + \Delta * (\chi) \qquad (2.1)$$

where $\chi \in q_c, q_r, N_c, N_r, q_i, q_{rim}, B_{rim}, N_i$, ($q_c$ - mass mixing ratio for cloud droplets, q_r - mass mixing ratio for rain, N_c - total number mixing ratio for cloud droplets, N_r - total number mixing ratio for rain, q_i - total (deposition plus rime) mass mixing ratio for ice, q_{rim} - rime mass mixing ratio for ice, B_{rim} - bulk rime volume, N_i - total number mixing ratio for ice), **t** is time, ρ is the air density, **u** is the 3D wind vector, z is height, $V\chi$ is the appropriately weighted fall speed for quantity χ, $S\chi$ is the source/sink term and includes various microphysical processes (condensation, autoconversion, accretion, evaporation, ice initiation, ice and snow aggregation, accretion by frozen particles, melting, and deposition), and $\Delta^*(\chi)$ is the subgrid-scale mixing operator (MORRISON; MILBRANDT, 2015).

Several studies have investigated the contribution of cloud microphysics and cumulus schemes in severe rainfall events (TAPIADOR et al., 2012; MAHBUB ALAM, 2014; JEWORREK; WEST; STULL, 2019; LU et al., 2019), with some results indicating that: i) the additional computational cost of using more sophisticated schemes does not always turn into a better forecast; ii) higher contribution from cloud microphysics compared to cumulus for high-resolution simulations; iii) dependence of rainfall on the mixing ratio of rainwater concentrated between low and mid-levels; and iv) different uses of physical parameterizations can cause a higher scatter in the ensemble prediction than the scatter caused by initially perturbed conditions.

2.2.2 Cumulus schemes

In NWP, it is called “gray zone” a range of model resolutions over which it is ambiguous whether or not the process should be parameterized, where parameterization schemes were designed to represent the subgrid scale processes that are not explicitly resolved because they are spatially or temporally too small scale, too complex and expensive, or not well understood (JEWORREK; WEST; STULL, 2019). Jeworrek et al. (2019), in a comprehensive review of cumulus and microphysics parameterizations across the convective gray zone, obtained better results for high-resolution simulations with the cumulus parameterization on, but caution that small-scale detailing and noise can contribute to decreased forecasting ability and that therefore each model configuration should have its own evaluation. Further studies have shown that activating the cumulus parameterization to high resolution can improve precipitation forecasting (GAO et al., 2017; ON; KIM; KIM, 2018), while others showed significant improvement in explicitly calculated convection in complex terrain regions and trivial in the flat areas (WAGNER et al., 2018).

The main classes of cumulus parameterization schemes are the adjustment type (BETTS; MILLER, 1986), moisture convergence (KUO, 1974), and the mass-flux type, with closure based on thermodynamical adjustment, (ARAKAWA; SCHUBERT, 1974). The convective adjustment scheme determines reference profiles of temperature and dewpoint toward which it nudges the model soundings at individual grid points. The first step is to locate the most unstable model parcel within approximately the lowest 200 hPa above the ground. They lift this parcel to its lifting condensation level (LCL), which they define as cloud base. From there, the parcel is lifted moist adiabatically until the equilibrium level (EL) is reached. Cloud top is then defined as the highest model level at which the parcel is still buoyant, typically just below the EL. If the parcel is not buoyant at any level, convection is not activated, and the scheme moves on to the next grid column. Suppose the cloud is less than 200 hPa deep, the scheme attempts to initiate shallow convection. Otherwise, they check to see if deep convection can be activated (BALDWIN; KAIN; KAY, 2002).

Moisture convergence schemes are computationally less demanding than other schemes, which likely is one reason for their continued usage. They related convective activity to

total column moisture convergence, in this way, convective activity is controlled by the moisture convergence over a deep layer encompassing the entire troposphere (EMANUEL; RAYMOND, 1993). In mass-flux schemes, clouds are idealized as plumes that all entrain environmental air as they rise and detrain only at the cloud top. Deviations from the grid-mean vertical motion are negative (downward) outside the clouds in the surrounding environment (compensating subsidence), this implies that mass going up in convective clouds is exactly balanced by this compensating subsidence in the local environment. Thus, these schemes are concerned with transferring mass from one vertical level to another (KWON; HONG, 2017).

The trigger functions are a set of criteria in the convective parameterization scheme used to initiate parameterized convection (KAIN; FRITSCH, 1992). Overall, the trigger functions consider the perturbations based on low-level vertical motion, parcel buoyancy, moisture convergence, perturbations based on local average moisture advection, CAPE, cloud depth threshold value, and moist sounding needed (CHOI et al., 2015). The environment's response to convective heating is extremely sensitive to its vertical distribution. It is also important for understanding the interactions between clouds and their environment, which most affect their heating and drying (KAIN; FRITSCH, 1990). Most schemes use simple one-dimensional entraining plume models to represent the thermodynamic and mass flux characteristics of individual clouds. These models constrain the mass flux profile by imposing a fixe rate of entrainment, or rate of increase of mass flux, with height.

2.2.3 Planetary boundary layer schemes

Moisture, heat, and momentum exchanges occur within the PBL through mixing associated with turbulent eddies. These eddies influence how the thermodynamic and kinematic structures of the lower troposphe evolve. Such eddies operate on a spatiotemporal scale that cannot be explicitly represented at the grid scale and time step applied in most models. As such, their effects are expressed via the use of PBL parameterization schemes (STULL, 1988). There are two major components of the process by which turbulence is represented: the order of turbulence closure and whether a local or nonlocal mixing approach is employed (COHEN et al., 2015).

The unknown term in the turbulence modeling equations is always one order above the maximum among the other terms, so the turbulence closure requires empirically relating the unknown term of moment $n+1$ to lower-moment known terms. This is referred to as nth - order turbulence closure. In first-order closure, only the prognostic equations for the means of the variables are retained and the turbulent fluxes are parameterized (STULL, 1988). As the order of the closure increases, the parameterizations include more equations for the higher moments. Thus, for 1.5-order closure, the parameterizations typically include equations not only for the standard prognostic variables, but also the potential temperature variance and the turbulent kinetic energy (STENSRUD, 2007). On the other hand, the second-order closure also has predictive equations for all remaining covariance terms.

The PBL schemes also differ according to the depth over which the known affects a given point. Local closure schemes, only the vertical levels that are directly adjacent to a given point directly affect variables at the given point. The opposite happens to nonlocal closure schemes where multiple vertical levels within the PBL can be used to determine variables at a given point (Figure 2.4). Large eddies can transport heat upward from the diurnally heated surface layer regardless of the localized stability maxima and produce countergradient fluxes. Nonlocal schemes account for these countergradient fluxes and, thus, generally represent deep PBL circulations accurately (STULL, 1991; COHEN et al., 2015).

Figure 2.4 – Schematic representations of the exchange among model layers in the local (ACM) and nonlocal (ACM2) closure schemes.

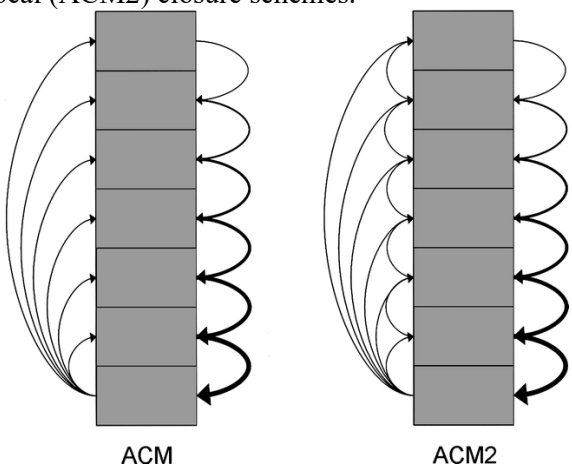

Source: Pleim (2007).

Some studies have verified the influence of PBL schemes (JIA; ZHANG, 2020; FALASCA et al., 2021) indicating that schemes with the nonlocal resolution are more susceptible to unstable stratifications producing stronger turbulent mixing, as schemes with local resolution are applicable to stable stratifications and produce less turbulent mixing.

2.2.4 Land – surface schemes

The land-surface models (LSMs) use atmospheric information from the surface layer scheme, radiative forcing from the radiation scheme, and precipitation forcing from the microphysics and convective schemes, with internal information on the land's state variables and land-surface properties, to provide heat and moisture fluxes over land points and sea-ice points (SKAMAROCK et al., 2019). The most robust land-surface models have treatment for vegetation, soil, snow, and water bodies. Characteristics such as the amount and type of vegetation in one grid cell, carbon budget, the number of soil layers for temperature and moisture, and the elevation of the terrain are also considered (JIN; MILLER; SCHLEGEL, 2010).

Three important vegetation parameters are the green vegetation fraction, the leaf area index (LAI), and the vegetation type or class. The green vegetation fraction is defined as the grid cell fraction wherein midday downward solar insolation is intercepted by photosynthetically active green canopy (CHEN et al., 1996). Traditionally, the LAI was sought in table files according to the vegetation type, by now, most of the models can use the satellite-based LAI, that are a 12 monthly climatology in general (LI et al., 2019). Vegetation types are also derived from satellite data and a simple biosphere model vegetation categorization consists of 16 land cover classes (LOVELAND et al., 2000).

The depth and density of the rooting zone determine the soil moisture available for exchanges with the first meters of the atmosphere. Once the upper soil layers become dry, they can act as a barrier to further upward moisture transport through the soil. Vegetation can overcome this barrier illustrating the importance of the amount, the type, and the variability of vegetation to the latent heat flux and moisture (STENSRUD, 2007).

The regional climate system is often disturbed by land-surface and land use changes due to human activities (e.g.,agricultural expansion, urbanization) and natural processes. Studies like He et al. (2017) and López-Bravo et al. (2018) suggest that the uncertainties

of the surface models, like changes in the extent of urban areas and changes associated with dynamic and thermodynamic variables, have induced local circulations and influenced the temperature, precipitation, and wind fields.

Stensrud et al. (2009) predicted that by the middle of 2020 decade, due to the usefulness of high-resolution forecasts and the rapid and continuous increase in computing power, the NWP would become an important component of the convective scale warning system. The high resolution of the models could provide information about the evolution and structure of the storms, and it was essential that the models were initiated with a very accurate representation of the convection to obtain the necessary correspondence between forecast and observed. The challenges in achieving this goal included improvements in data assimilation methods, increased use of radar observations, improvements in the parameterization schemes of the models, in addition to a complete understanding of the forces that initiate and organize severe storms, as well as the environmental parameters that allow its identification and monitoring (JORGENSEN; WECKWERTH, 2003).

2.3 Weather analysis

2.3.1 Ingredients for severe weather

Severe storm events develop quickly and have significant consequences for society and the economy. In this way, it is essential to quickly recognize the development and conditions that lead to the formation of such events. This is done efficiently through studies that determine the atmospheric environment before and during the occurrence of a storm (FABRY, 2015). Heavy precipitation is the result of sustained high rainfall rates or long lasting systems. In turn, high rainfall rates involve the rapid ascent of air containing substantial water vapor and depend on the precipitation efficiency. The length of an event is associated with its speed of movement and the size of the system (DOSWELL; BROOKS; MADDOX, 1996). The main triggering factors for their occurrence are the presence or combination of conditional instability, moisture, and the initial lifting mechanism.

Instability determines the potential for air to accelerate vertically. The requirements for moisture and conditionally unstable lapse rates can be understood in terms of convective available potential energy (CAPE). The lift is needed to initiate the convection because the atmosphere is never sufficiently unstable the convective overturning can begin

spontaneously. Substantial negative buoyancy must often be overcome before a rising parcel reaches its level of free convection (LFC). The origins of this required lift are unlikely to be found in large-scale ascent. The magnitude of large-scale vertical motion (few centimeters per second) is simply too small to accomplish the needed lift in a reasonable time. Disregarding the cases where convection develops is a region of extensive cloudiness, like the cold fronts, we can conclude that the lift needed to start deep convection is generally a product os mesoscale process (DOSWELL, 1987).

Wind shear shapes storms and influences their evolution. When environmental wind shear is limited, mostly isolated cells that do not interact in organized ways are observed. As shear increases, specific organized interactions are promoted, and storm systems generally become larger, more complex, and more persistent (FABRY, 2015). The life of a single cell is limited by the collapse of its precipitation core, which is filled with heavy hydrometeors, onto its updraft, and by undercutting of the updraft from its source of potentially buoyant air by cold outflow driven by the evaporation of precipitation (Figure 2.5). Vertical wind shear increases a storm's longevity by counteracting these two detrimental processes (MARKOWSKI; RICHARDSON, 2010). The lifting mechanism such as a cold front, a sea breeze, or smaller scale convergence patterns, and the synoptic-scale environment associated with it also determine the location, shape, and extent of the convection.

Environments with various combinations of CAPE and wind shear, which can occur at all times and in all seasons, are capable of producing severe weather. Sherburn and Parker (2014) presented a climatology for the severe weather environment, starting from high shear values and low CAPE values, and introduced new parameters such as lapse rate at low and mid-levels and wind and shear at multiple levels as statistically more skillful indicators for severe weather forecasting (Figure 2.6).

Westermayer et al. (2017), with the goal of exploring the relationship between atmospheric parameters and the occurrence of convective thunderstorms, used six years of reanalysis data and found that instability is important up to a certain amount. Approximate CAPE values between 200 and 400 $J.kg^{-1}$ were more important for the occurrence of lightning strikes than larger values. The availability of moisture in the lower troposphere had a greater influence on the occurrence of thunderstorms and wind shear

played an important role, but only when it occurred at low or very high values, with a lower probability of occurrence for intermediate values.

Figure 2.5 – Role of wind shear in storm development.

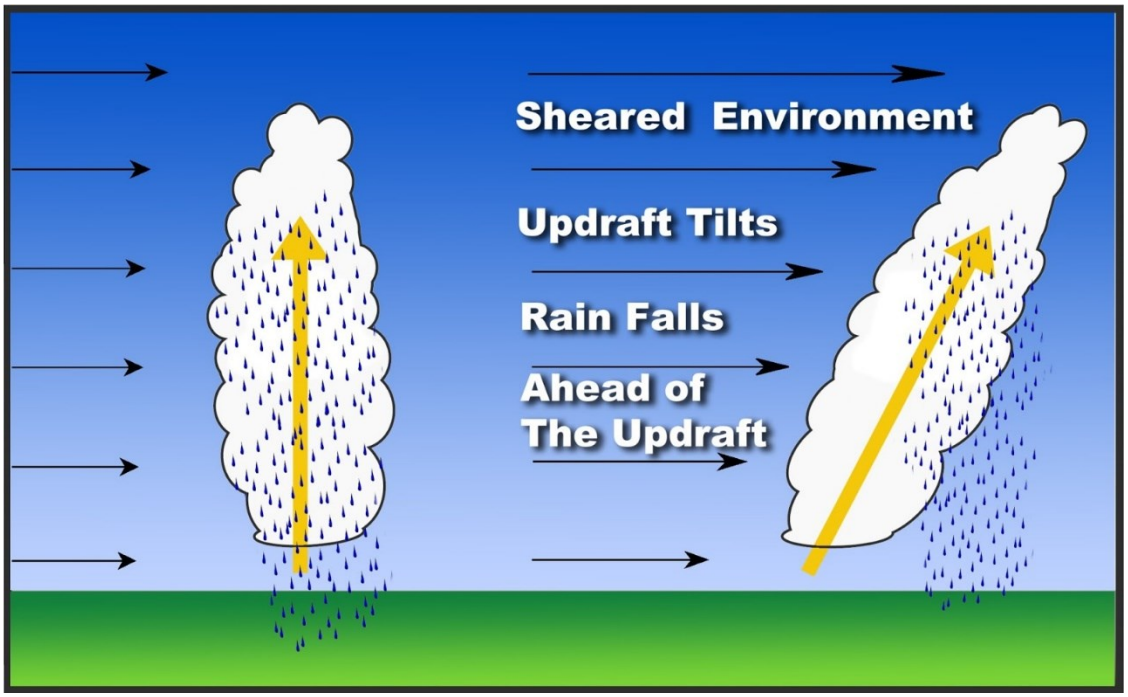

The storm experiencing little or no wind shear will produce a vertical updraft, which will quickly get killed off by falling rain. However, the storm experiencing strong wind shear will develop a tilted updraft with the rain falling away from the updraft (available on https://www.weather.gov/ilx/swop-springtopics).

Source: NWS/NOAA (2020).

Taszarek et al. (2021) states that the long-term trend of the environment characteristic of severe storms, in other words, conditional instability, availability of moisture at low levels, wind initiation, and shear mechanism, follow only partially the expectations of the warming climate, that is, despite the increased instability, the environment may be less favorable for thunderstorms due to stronger inhibition energy and lower moisture availability.

Poletti et al. (2017) also presented a study based on meteorological indices for predicting severe storms. They used a tool, based on a checklist, which considered physical and thermodynamic processes directed at storm formation, evolution, and organization. One of the main conclusions was the recognition of the seasonal dependence of some indices,

suggesting the formulation of a new version for the identification tool, one for the warm season and one for the cold season.

Figure 2.6 – Organization of individual convective storms and lines of systems of convective storms as a function of CAPE and shear.

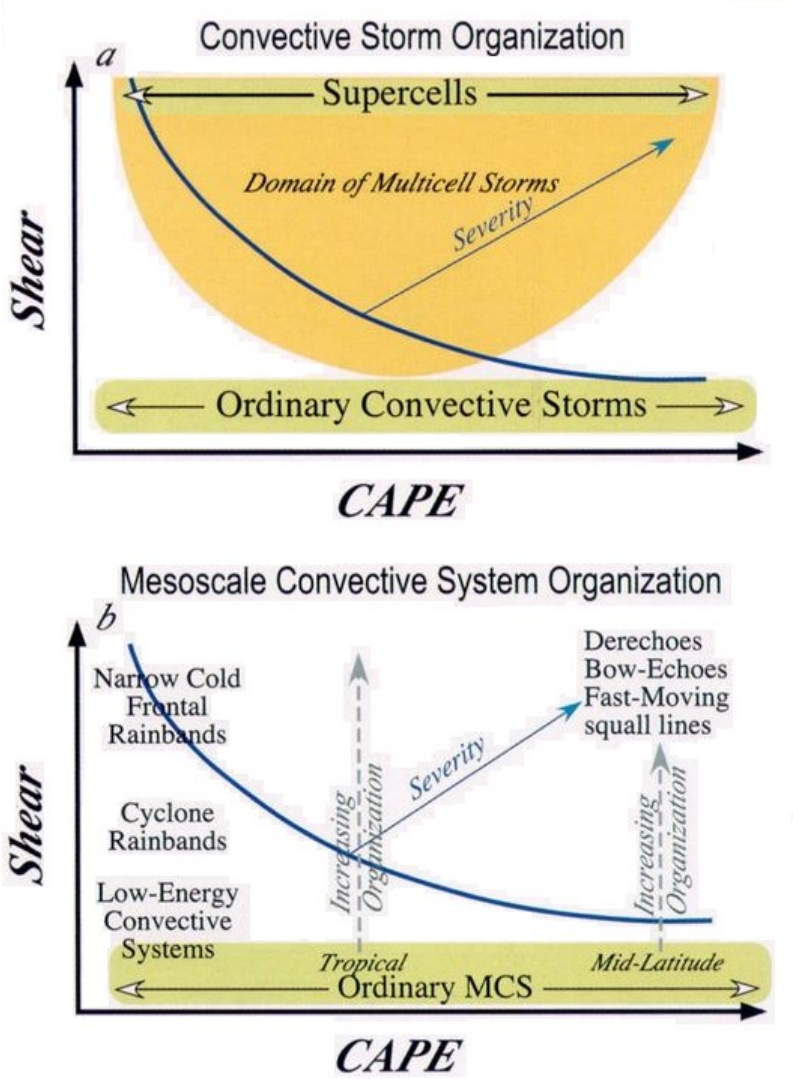

(a) Schematic depiction of convective storm types usually associated with typical vertical wind shear and CAPE environments: the approximate range of multicellular storms is shown by the shaded region; (b) mesoscale convective system organization usually associated with similar CAPE-shear regimes. The curved line running from the upper left to the lower right of each plot indicates the approximate dividing line between severe and nonsevere storms. Although the axis values are meant to be schematic, a typical range of CAPE is probably 0-5000 J kg^{-1} and the range of shear is probably 0-20 ms^{-1} over the lowest 2.5 km of height.

Source:Jorgensen and Weckwerth (2003).

In this way, Fabry (2015) has summarized the main ingredients necessary for a severe storm to occur: 1) a high-CAPE value; 2) some initial resistance to convection or convective inhibition (CINE); 3) a continuous supply of moisture; 4) some support from the high levels; 5) wind shear, especially at low and medium levels; and 6) convergence at low levels to break the CINE resistance local. Instability determines the potential for vertical air acceleration, whereas wind shear shapes the storm and influences its evolution. Finally, a lifting mechanism, such as a cold front, sea breeze, or smaller scale convergence patterns, also determine the location, shape, and extent of the convection. In the NEB case, smaller scale convergence patterns are caused by the changes in the frinction as the low level air parcels flow from the ocean into the continent. Further instability is associated to the local topography with a elevation of the order of a few hundred meters parallel to the coast and apprximately perpendicular to the prevailing SE trades (SILVA DIAS, 2022).

2.3.2 Storm morphology by weather radar

Storms produce various severe weather phenomena detectable by weather radar. Convective processes within a thunderstorm are relatively fast, most lasting less than an hour. In this interval, updrafts and downdrafts are generated, which can result in precipitation and locally strong winds. Dozens of cells can be represented within the coverage of a single radar, and despite the small spatial and temporal scales of these storms, radars can monitor them almost instantaneously. This ability is the main factor why radar networks have been installed in many countries (FABRY, 2015).

The first classifications of the reflectivities observed by radar on clustered structures refer to Marwitz (1972a, 1972b, 1972c), who classified the storms studied into supercells, multicells, and severely sheared storms. Numerous studies have used radar (PARKER; JOHNSON, 2000), radar and satellite (JIRAK; COTTON; MCANELLY, 2003), and even radar and rain gauge (BALDWIN; KAIN; LAKSHMIVARAHAN, 2005) reflectivity data to categorize, especially mesoscale convective systems, by their mode of organization (Figure 2.7). No matter which classification system is used, the classification of convective system morphology can be difficult. Some subjectivity is inherent in the classification since some systems exhibit aspects of multiple morphologies with changes occurring both spatially and temporally (DUDA; GALLUS, 2010). Li et al. (2021) argues

that the different modes of organization are related to their formation and the prevailing thermodynamic mechanisms, and that prior knowledge of their morphology can increase the predictability of systems.

Figure 2.7 – Schematic reflectivities illustrating the morphologies of the nine organizational modes.

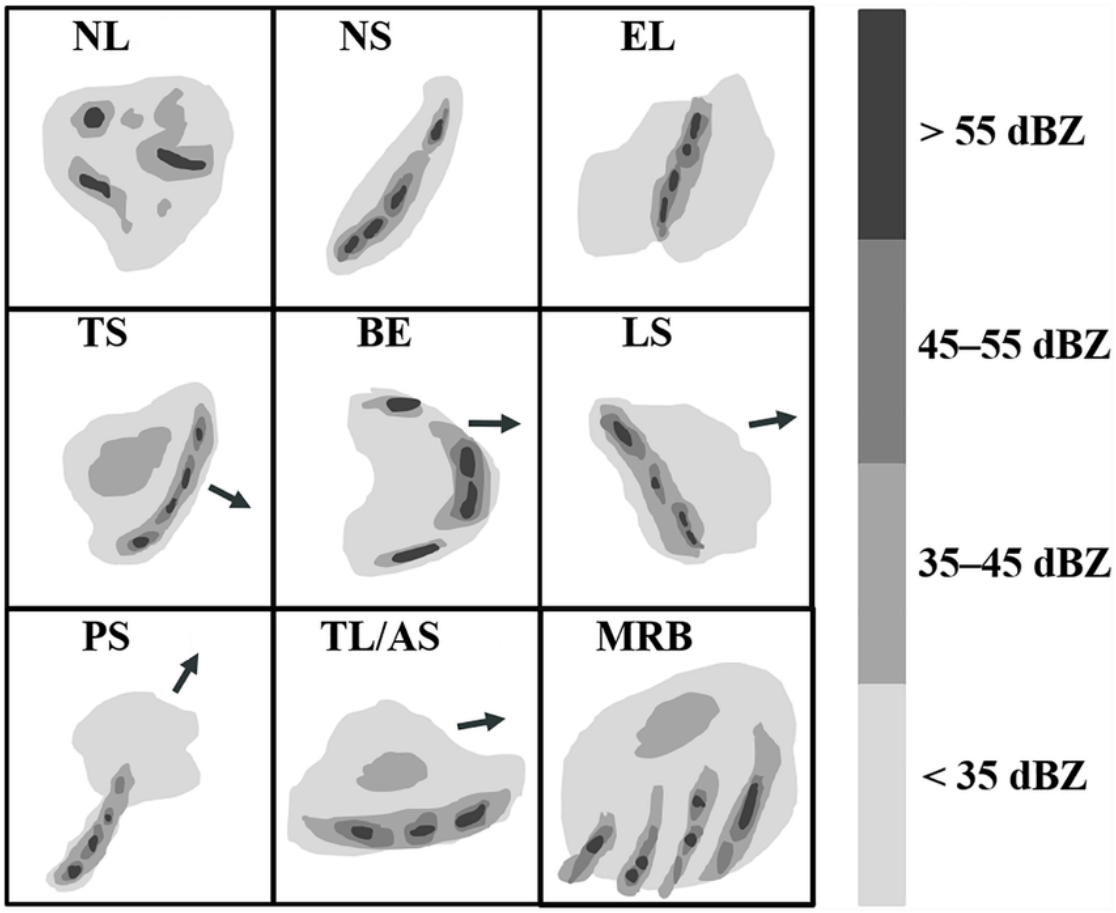

This classification of mesoscale convective systems (MCSs) considers the arrangement of convective and stratiform regions, the morphology of convective reflectivities and the direction of the motion of the convective system. The arrow indicates the direction of the movement of the MCS. NL - nonlinear mode, TS - trailing stratiform precipitation, NS - no stratiform precipitation, LS - leading stratiform precipitation, PS - parallel stratiform precipitation, EL - embedded lines, BE - bow echoes, TL/AS - training line/adjoining stratiform, and MRB - multiple rain bands.

Source: Adapted from Li et al. (2021).

Among the main radar products for surveillance strategies, the most common are azimuth or Plan Position Indicator (PPI) scans at different elevation angles, the Constant Altitude

Plan Position Indicator (CAPPI), which is a representation of the radar reflectivity at a specific ground level, the vertical sections or Range-Height Indicator (RHI), which are sections extending across all elevations at a fixed position.

3 METHODOLOGY

3.1 The study area

The NEB represents 21.25% of Brazilian territory, with three predominant climate types (ALVARES et al., 2013): (i) humid coastal, from the coast of the state of Bahia to the coast of the state of Rio Grande do Norte, (ii) tropical, in parts of the states of Bahia, Ceará, Maranhão, and Piauí, and (iii) tropical semi-arid, in the countryside of all the states of the region except Maranhão (Figure 3.1). The region presents high temperatures, with an annual average between 20 °C and 28 °C, and a small thermal amplitude. The rainfall is irregular, with annual values higher than 2000 mm in the coastal region and less than 500 mm in the inland areas (CENAD, 2012). The NEB had the highest number of abnormalities, as declared by municipal ordinances, in the period from 1 January 2013 to 5 April 2022, and was also the region with the highest rate of events per risk area (CEMADEN, 2019; CNM, 2022). The metropolitan region of Recife (municipalities with a red background in Figure 3.1c) has the largest coverage of the population in risk areas and the second-highest number of people in risk areas (IBGE, 2018).

3.2 Data set

CEMADEN maintains a platform (Brazilian Early Warning System (BEWS)) for registering the occurrence of natural disasters in Brazil (ASSIS DIAS et al., 2020). Via this platform, details about geohydrological disaster events, such as locality, date and time of the opening and closing of the alerts, the description of the event, alert levels, accuracy of time and location, magnitude or scope of the alerts, human damage, and the sources of the information records, are registered. Not all municipalities are part of the national strategy for monitoring extreme rainfall events, either because they do not have the minimum structure necessary for monitoring or because they do not have areas classified as high risk. The municipalities monitored in eastern Pernambuco state can be seen in Figure 3.1c.

Through this database were obtained the records of the occurrences of 24 severe rainfall events for the east of the state of Pernambuco for the years 2017, 2018, and 2019. CEMADEN's automatic rain gauge network was used to analyze the rainfall intensity in Pernambuco. The total quantity varied according to the date of the analyzed event due to

the constant equipment maintenance, but it has a maximum number of 298 rain gauges and a minimum of 170, represented by the red dots in Figure 3.1b.

Figure 3.1 – The study area.

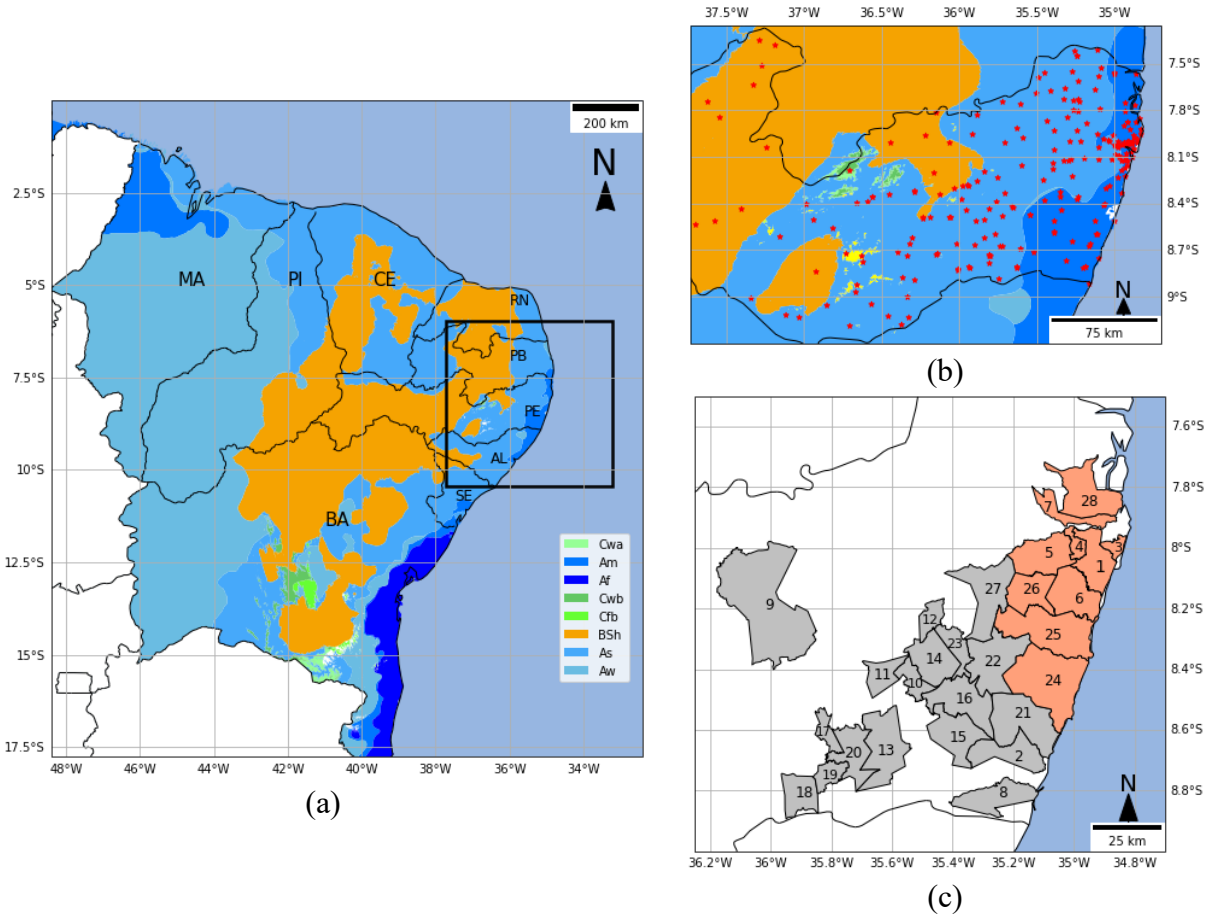

(a) Koppen's climate classification for the nine states of NEB (BA – Bahia, SE – Sergipe, AL – Alagoas, PE – Pernambuco, PB – Paraíba, RN – Rio Grande do Norte, CE – Ceará, PI – Piauí, and MA – Maranhão); the black rectangle is the region where the numerical simulations were performed using the WRF model. (b) A zoom-in representation of the eastern Pernambuco state; the red dots are the 298 rainfall stations used to verify the simulations. (c) The 28 monitored municipalities affected by natural disasters in this study (1 – Recife, 2 – Rio Formoso, 3 – Olinda, 4 – Camaragibe, 5 – São Lourenço da Mata, 6 – Jaboatão dos Guararapes, 7 – Abreu e Lima, 8 – Barreiros, 9 – Caruaru, 10 – Cortês, 11 – Barra de Guabiraba, 12 – Chã Grande, 13 – Palmares, 14 – Amaraji, 15 – Gameleira, 16 – Ribeirão, 17 – Belém de Maria, 18 – São Benedito do Sul, 19 – Jaqueira, 20 – Catende, 21 – Sirinhaém, 22 – Escada, 23 – Primavera, 24 – Ipojuca, 25 – Cabo de Santo Agostinho, 26 – Moreno, 27 – Vitória de Santo Antão, and 28 – Igarassu).

Figure 3.2 – Study area and radar characteristics.

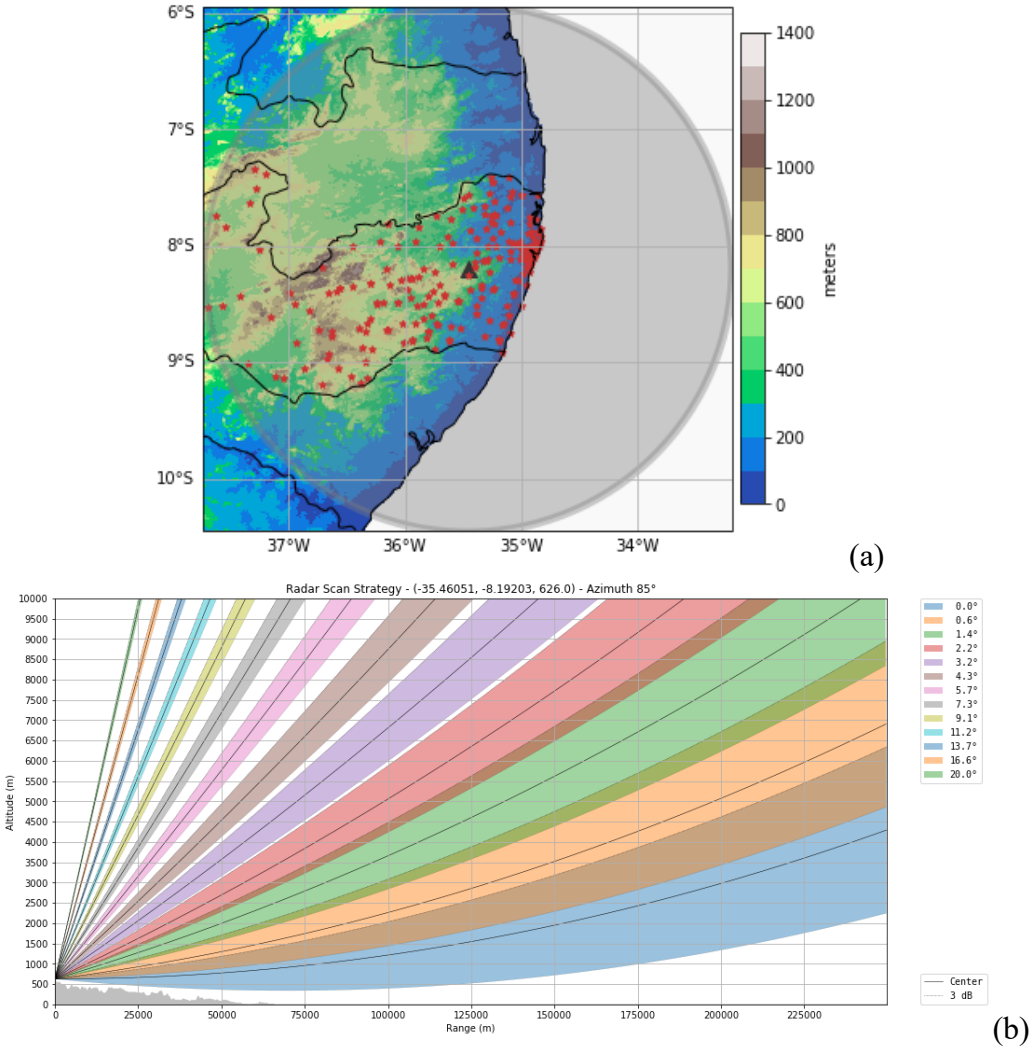

(a) The orography of the study area is in meters. The gray triangle denotes the radar's position and range arc (shaded gray circle). Red points mark the position of the rainfall stations; (b) radar action strategy with 13 elevations ranging from 0 to 20 degrees in the azimuth 85 degrees.

Also, radar data from the Agência Pernambucana de Águas e Clima (APAC) was used to verify the intensity and morphology of the storms. This radar is installed at latitude 8.19203°S and longitude 35.46051°W, in the municipality of Chã Grande and at an altitude of 626 meters (Figure 3.2a). It is a dual-polarized S-band Doppler radar with 13 elevation angles, a horizontal range of 250 km in the surveillance mode, a spatial resolution of 250 m in polar coordinates, an azimuthal resolution of one degree, and a temporal resolution of 10 min (Figure 3.2b). A preliminary treatment was performed to eliminate non-meteorological echoes through the radar polarimetric variables according to Crisologo et al. (2014), and the products used in the storm analysis were volumetric

reflectivity data. For processing the radar data, the wradlib library was used (HEISTERMANN; JACOBI; PFAFF, 2013).

To classify the synoptic and mesoscale systems, we used the analyses in the synoptic timetables and the 3-hour forecasts of the Global Forecast System (GFS) of the National Centers for Environmental Prediction (NCEP) with a grid spacing of 0.25° latitude and longitude (NCEP, 2015) and GOES16 satellite data (GOES-R CALIBRATION WORKING GROUP; GOES-R PROGRAM OFFICE, 2017).

3.3 Weather classification

Between 2017 and 2019, 413 natural disaster alerts were sent to the monitored municipalities in eastern Pernambuco state. Among these alerts, there were occurrences in 124 cases, when there was a confirmation of some flooding or landslide event. These 124 cases were grouped into 32 severe weather events, due to the ability of a single weather system to affect multiple counties. Of these 32 meteorological events, 8 were discarded for having an indirect relationship with rainfall. Thus, 24 episodes of severe rainfall were analyzed in detail in this study.

Rainfall stations record precipitation values at a constant 10-minute interval. From the time the alerts were sent, an objective analysis was performed using the Cressman method (CRESSMNAN, 1959) with the same resolution of the simulations to be performed (2.5 km) and considering a radius of influence of 15.0 km for each observation, and spatial maps of precipitation accumulations were built. In the regions where the highest rainfall accumulations coincided with the alerted municipalities, temporal sections of precipitation were constructed to identify the behavior of rainfall in each storm.

The radar products analyzed were CAPPI built with 1 km horizontal and 500 m vertical resolution and the PPI from the first elevation. Vertical CAPPI sections were also constructed at the positions and moments of highest precipitation. GOES 16 satellite data in channels 2 (visible 0.64μ), channels 8, 9, and 10 (water vapor 6.19μ, 6.95μ, and 7.34μ, respectively), and channels 13 and 16 (infrared 10.35μ and 13.3μ, respectively) were used to identify precipitation systems, often using a color enhancement to highlight the structures of interest. Still, to classify the systems, through the GFS model data, the meteorological variables of sea-level pressure, streamlines and wind magnitude at various

levels, geopotential height, and wind divergence were also analyzed and the perturbed field of these variables, which can be described by the following equation:

$$var' = var - \overline{var} \tag{3.1}$$

where *var* is any variable, $\overline{var}$ is the mean field and *var'* is the perturbed field.

3.4 Numerical Simulations

Table 3.1 presents the four severe rainfall events selected for sensitivity testing with the WRF model (version 4.2) according to the use of the microphysics, the planetary boundary layer, cumulus, and land surface parameterizations and for diagnostic analysis. Table 3.2 displays the set of tested schemes and their references. These schemes were chosen because the official model documentation states that they can be used in high resolution. For each event analyzed, 24 h of simulation was performed with initialization, if possible, at least 6 h before the onset of precipitation.

Table 3.1 – Characteristics of the severe rainfall events studied.

Date	Municipalities affected	Higher rainfall rates			Rain duration (hours)	Total accumulated (mm)
		mm/10min	mm/1h	mm/24h		
20170528	16	14.9	47.3	280.4	48	395.9
20170720	16	23.2	29.1	170.5	72	264.0
20180422	5	15.1	61.0	135.7	57	193.6
20190529	4	15.6	55.2	212.7	37	224.0

The black rectangle demarcates the region used in the numerical simulations in Figure 3.1a. The simulations were performed in two nested regions following a one-way nesting strategy, the parent domain, with a 5.0 km resolution and a 200 × 200 point grid, and the internal domain (used in this study), with 2.5 km resolution and a 201 × 201 point grid, both centered at 8.19203° S latitude and 35.46051° W longitude, with the model top at 50 hPa and 40 levels using the terrain-following vertical coordinate. For the initial and boundary conditions, the GFS analysis and forecasts every 3 h were used. The time step of the WRF model was set to 15 s, and the output frequency of the WRF model was 1 h.

All the possible combinations between the tested physical schemes would be on the order of thousands of simulations. To reduce the high computational cost of the simulations, we evaluated the physical schemes within their own physical type, choosing the most

skillful scheme among them and then analyzing the next set of physical options (DAI et al., 2021). After the simulations concerning the microphysics parameterization schemes, it is possible to verify the PBL schemes because there is no direct interaction with microphysics, followed by the cumulus parameterizations, which do not interact with the PBL, and finally land surface schemes (Figure 3.3) (STERGIOU; TAGARIS; SOTIROPOULOU, 2017). Each experiment set started with the RRTMG shortwave and longwave radiation schemes (invariant in all simulations), MYJ scheme for the planetary boundary layer, cumulus off, and RUC for surface and ranging of the microphysics schemes. After the best microphysics scheme was defined, all the planetary boundary layer parameterizations in Table 3.2 were tested, and after the best scheme was defined, the cumulus and surface parameterizations were checked in the same way.

Figure 3.3 – Interactions between the WRF parameterization schemes.

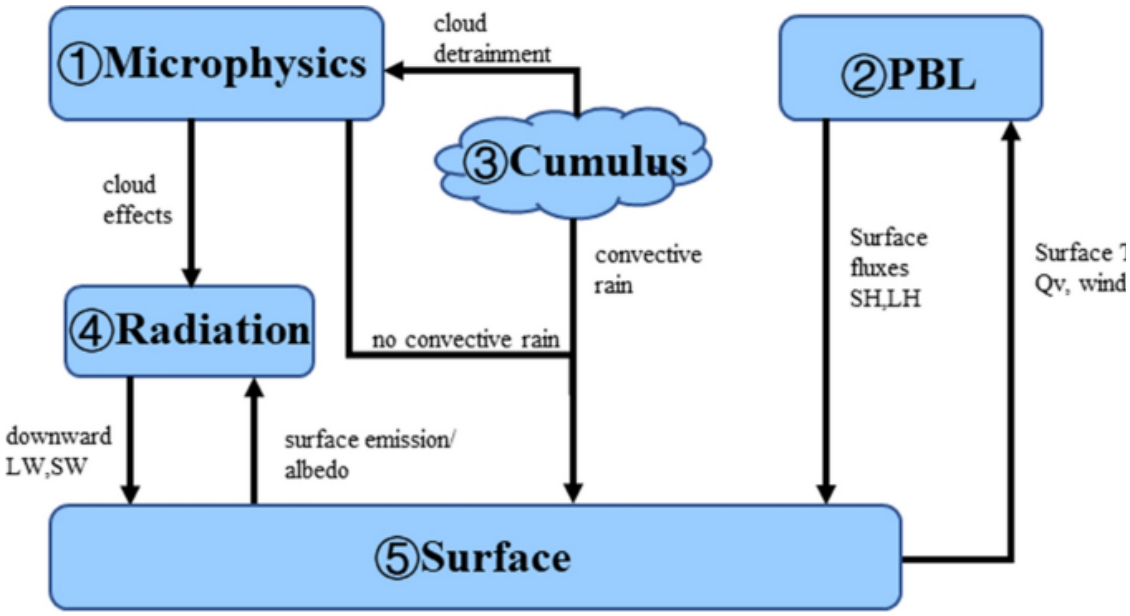

Source: Dai et al. (2021)

3.5 Forecast verification

Values of precipitation from the grid model and rain gauge point observations were compared using the point-to-grid approach. This comparison can lead to uncertainties in the verification results, but considering the high resolution of the model and the dense observation network, these uncertainties can be minimized (MERINO et al., 2022). To evaluate the model configurations, all the schemes in Table 2 were tested using standard

deviation (σ, Equation (3.2)), Pearson's correlation coefficient (R, Equation (3.3)), and root mean square error (RMS, Equations (3.4) and (3.5)) and summarized graphically through the Taylor diagram (TAYLOR, 2001), the relative error (RE, Equation (3.6)), and finally the bias (Equation (3.7)) to determine which scheme gave the best performance, comparing the precipitation generated by the model and the hourly accumulations data provided by rainfall stations. The equations of the statistical indexes used are described below:

$$\sigma_x^2 = \frac{1}{n}\sum_{i=1}^{n}(x_i - \bar{x})^2 \tag{3.2}$$

$$R_{f,o} = \frac{\frac{1}{n}\sum_{i=1}^{n}(f_i - \bar{f})(o_i - \bar{o})}{\sigma_f \sigma_o} \tag{3.3}$$

$$RMS = \frac{1}{n}\sum_{i=1}^{n}\left[(f_i - \bar{f}) - (o_i - \bar{o})\right]^2 \tag{3.4}$$

$$RMS^2 = \sigma_f^2 + \sigma_o^2 - 2\sigma_f \sigma_o R_{f,o} \tag{3.5}$$

$$RE = \frac{\left(\sum_{i=1}^{n}\bar{f_i} - \sum_{i=1}^{n}\bar{o_i}\right)}{\sum_{i=1}^{n}\bar{o_i}} * 100\% \tag{3.6}$$

$$Bias = \frac{1}{n}\sum_{i=1}^{n}(f_i - o_i) = \bar{f} - \bar{o} \tag{3.7}$$

In Equations (3.2)–(3.7), x indicates any variable, f is the forecast value, and o is the observed value. The cumulative hourly rainfall values observed at the rain gauge stations were compared with the cumulative hourly rainfall values predicted on an average across the nine grid points closest to the position of the rain gauge in focus. Equation (3.5) is used to calculate the RMS when the values σ_f, σ_o, and $R_{f,o}$ are used in the normalized Taylor diagram form (TAYLOR, 2001). When some configurations showed similar results, the next set of schemes to be checked were analyzed not only with the improved configuration considered but also with all the schemes considered good. Similarly, the Taylor diagram was used as a tiebreaker metric when the RE and the bias were close between two different configurations.

After testing the model's physical schemes, the HYSPLIT model (STEIN et al., 2015) was used to verify where the air parcels influencing the region were coming from. The

model calculation method is a hybrid between the Lagrangian approach, using a moving frame of reference for the advection and diffusion calculations as air parcels move from their initial location, and the Eulerian methodology, which uses a fixed three-dimensional grid as a frame of reference to compute air concentrations. The model can be run interactively through its platform called READY (ROLPH; STEIN; STUNDER, 2017), and the data used in its execution were the same as those used in this study (NCEP, 2015).

Table 3.2 – Physical schemes tested in the simulations.

Physics	Number Options[1]	Acronym	Scheme	Reference
Microphysics	28	TpsonAA	Thompson Aerosol-Aware	Thompson and Eidhammer (2014)
	2	PurdLin	Purdue Lin	Chen and Sun (2002)
	5	EtaFerr	Eta (Ferrier)	Rogers et al. (2001)
	8	Thompson	Thompson	Thompson et al. (2008)
	10	Morrison	Morrison 2-Mom	Morrison et al. (2009)
	18	NSSL+CCN	NSSL 2-Mom + CCN	Mansell et al. (2010)
	24	WSM7	WRF Single-Moment 7-class	Bae et al. (2019)
	26	WDM7	WRF Double-Moment 7-class	Bae et al. (2019)
	6	WSM6	WRF Single-Moment 6-class	Hong and Lim (2006)
	16	WDM6	WRF Double-Moment 6-class	Lim and Hong (2010)
	4	WSM5	WRF Single-Moment 5-class	Lim and Hong (2010)
Planetary boundary layer[2]	2 (2)	MYJ	Mellor-Yamada-Janjic scheme	Janjic (1994)
	6 (2)	MYNN3	Mellor-Yamada Nakanishi and Niino Level 3	Nakanishi and Niino (2009)
	7 (7)	ACM2	Asymmetric Convective Model	Pleim (2007)
	10 (10)	TEMF	Total Energy - Mass Flux	Angevine et al. (2010)
	11 (1)	ShinH	Shin-Hong scheme	Shin and Hong (2015)
	4 (4)	QNSE	Quasi-Normal Scale Elimination	Sukoriansky et al. (2005)
	1 (1)	YSU	Yonsei University Scheme	Hong et al. (2006)
	0 (5)	SMS3D	Subgrid Mixing Scheme	Zhang et al. (2018)
	5 (5)	MYNN2	Mellor-Yamada Nakanishi and Niino Level 2.5	Nakanishi and Niino (2009)
Cumulus	1	KainF	Kain-Fritsch	Kain (2004)
	3	GF	Grell-Freitas	Grell and Freitas (2013)
	5	G3	Grell-3	Grell and Dévényi (2002)
	6	Tiedtke	Tiedtke scheme	Zhang et al. (2011)
	10	KFCuP	Kain-Fritsch-Cumulus Potential	Berg et al. (2013)
	16	NewT	New Tiedtke Scheme	Zhang and Wang (2017)
Land Surface[3]	1	TDS	Thermal Diffusion Scheme	Dudhia (1996)
	2	Noah	Unified Noah LSM	Tewari et al. (2004)
	3	RUC	Rapid Update Cycle	Benjamin et al. (2004)
	4	NoahMP	Noah Multi-Physics	Niu et al. (2011)
	4 (1)	UCM	Urban Canopy Model	Chen et al. (2011)

[1] Option number in the model configuration. [2] Numbers of the surface layer schemes used with the PBL schemes.

3.6 Diagnostic analysis

To characterize the severe rainfall events, several dynamic and thermodynamic parameters were calculated in the regions where the maximum precipitation was verified and where there were municipalities with confirmed occurrences of natural disasters (areas denoted by the yellow box in Figure 3.4).

Figure 3.4 – Region of intersection between the heaviest precipitation and the alerted municipalities.

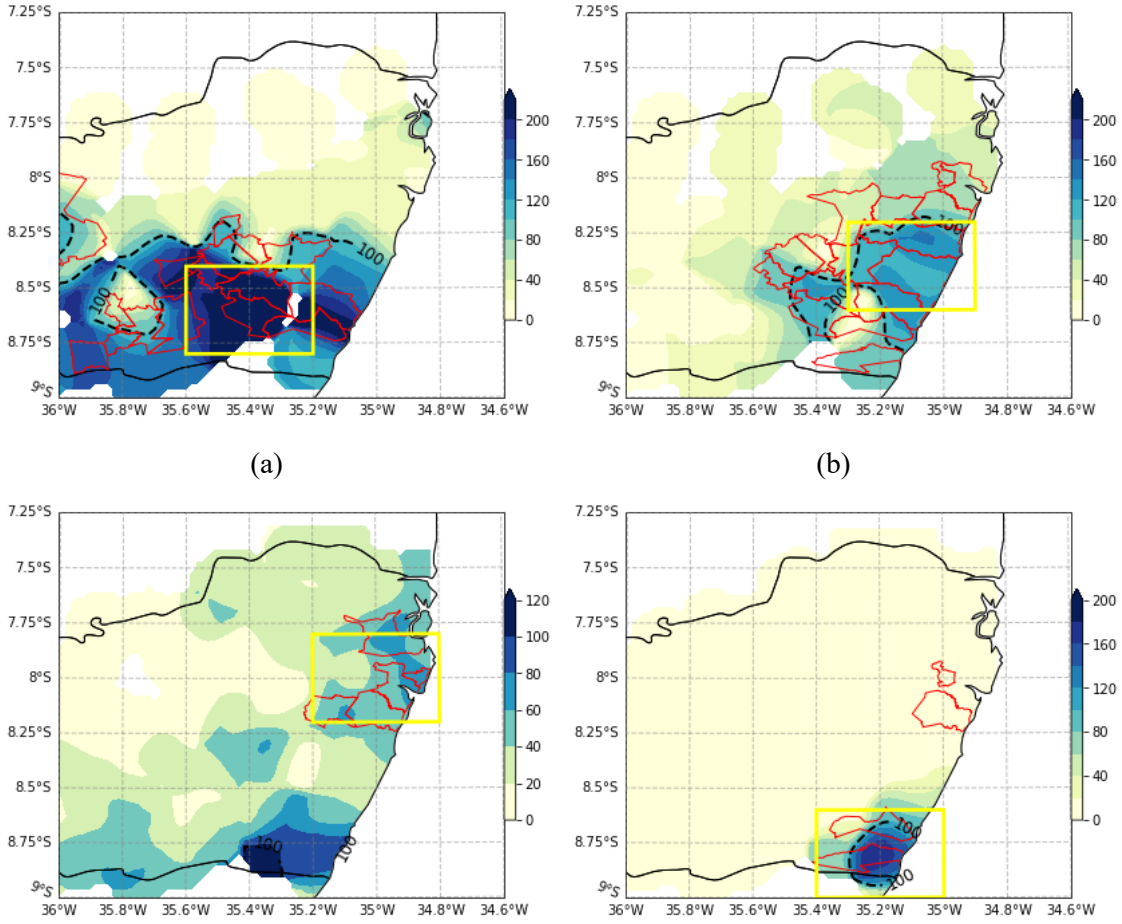

The blue shading (a–d) is the 24-h precipitation accumulation (mm/24 h) recorded by the rain gauges and interpolated using the Cressman technique with a 15 km radius. (a) Precipitation ranges from 20170527 12UTC to 20170528 12UTC, (b) from 20170720 00UTC to 20170721 00UTC, (c) from 20180422 00UTC to 20180423 00UTC, and (d) from 20190528 12UTC to 20190529 12UTC. The dotted line in black marks the 100 mm/24 h isohyet, the red areas are the municipalities affected by natural disasters, and the yellow boxes are the intersection regions between the heaviest rainfall and the municipalities affected by natural disasters and where the diagnostic analyses were performed.

To analyze atmospheric instability and initial convection resistance, the *CAPE* (Equation (3.8)) and *CINE* (Equation (3.9)) indicators were used, respectively. The low-level moisture supply was measured using moisture flux convergence (*MFC*, Equation (3.10)). The support at high and medium levels was verified using cyclonic vorticity advection (ADV_ζ, Equation (3.11)), disregarding the β term due to low latitudes.

The relationship between vertical wind shear and the severity condition of the studied events was also verified through vertical bulk shear in the deep layer (0–6 km, Equation (3.12)) and the middle layer (0–3 km, Equation (3.13)) and the evaluation of the change in wind direction with height.

$$CAPE = R_d \int_{p_f}^{p_n} (T_{vp} - T_{ve}) d \ln p \tag{3.8}$$

$$CINE = -R_d \int_{p_i}^{p_f} (T_{vp} - T_{ve}) d \ln p \tag{3.9}$$

$$MFC = -u\frac{\partial q}{\partial x} - v\frac{\partial q}{\partial y} - q\left(\frac{\partial u}{\partial x} + \frac{\partial v}{\partial y}\right) \tag{3.10}$$

$$ADV_\zeta = -\left(u\frac{\partial \zeta}{\partial x} + v\frac{\partial \zeta}{\partial y}\right) \tag{3.11}$$

$$SHEAR_{0-6km} = \sqrt{u_{500mb}^2 + v_{500mb}^2} - \sqrt{u_{10m}^2 + v_{10m}^2} \tag{3.12}$$

$$SHEAR_{0-3km} = \sqrt{u_{750mb}^2 + v_{750mb}^2} - \sqrt{u_{10m}^2 + v_{10m}^2} \tag{3.13}$$

where u and v are, respectively, the zonal and meridional wind components at the corresponding levels; R_d is the specific gas constant for dry air; T_{vp} is the virtual temperature of a rising air parcel through the humid adiabatic; T_{ve} is the virtual environment temperature; p_f, p_n, and p_i are, respectively, the isobaric levels of free convection, equilibrium, and lift condensation; q and ζ are the specific humidity and the relative vorticity, respectively; *CAPE*, *CINE*, u, and v are provided by the model; and q is calculated through the vapor pressure of the air and ζ through the wind components.

4 OBSERVATIONAL ANALYSIS

The analysis of the frequency of alerts sent to the eastern Pernambuco state can be seen in Figure 3. Alerts intensify between late February and early August and are almost non-existent between mid-August and December. There is also a slight preference for sending alerts during nighttime hours (Figure 4.1a). The vast majority of the events are concentrated in the coastal belt and the metropolitan region of Recife, especially the cities of Recife, Cabo de Santo Agostinho, and Olinda, with more than 30% of alerts sent (Figure 4.1b).

Figure 4.1 – Warnings sent to eastern Pernambuco.

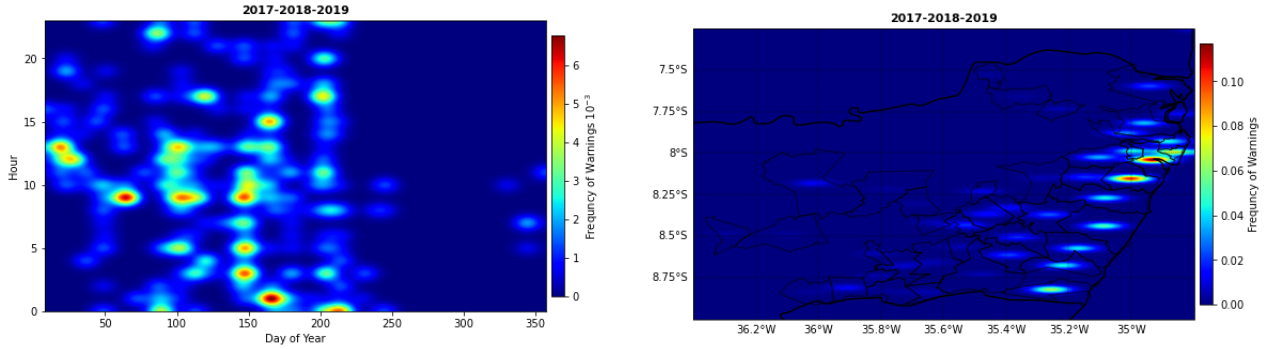

(a) (b)

Temporal (a) and spatial (b) distributions of the 413 alerts sent to eastern Pernambuco state between the years 2017 and 2019.

The higher occurrence of alerts being sent at this time of year is aligned with the rainy season in the region (OLIVEIRA; SANTOS E SILVA; LIMA, 2017) and the preference for the coastal belt may be associated with higher population density, a greater number of risk areas and susceptibility to natural disasters or so-called social factors (MATIAS RIBEIRO et al., 2021), in other words, both the occurrence of severe weather systems and the local characteristics of the cities that usually present areas with inadequate housing conditions and higher social vulnerability (POLAND NICOLODI; PETTERMANN, 2011). The higher number of alerts issued during nighttime hours may be related to the night maximum of rainfall activity due to convergence between the mean onshore flow and the offshore land breeze (KOUSKY, 1980) as these local systems can induce thunderstorm formation by increasing instability and moisture flux convergence due to their propagation (BHATE et al., 2016).

4.1 Synoptic and mesoscale analysis

Figure 4.2 shows the severe weather systems that hit the eastern PE state at the moments of the highest precipitation or early in their development. The events on days 20170303, 20170412, and 20170507 were characterized by a ridge on the surface, or even a closed high-pressure core (Figure 4.2b), deflecting the low-level flow into cyclonic curvature (Figure 4.2a-c) and favoring the convergence of the trade winds on the PE coast. In all three cases, there was a confluence zone of currents at high levels or a ridge favoring coupling between the low and high troposphere. Thus, these events were marked by local forcing at the surface and altitude.

In the 20170524 event, the high-pressure region at the surface was again present and at altitude an intense trough over the coast of PE with an area of strong horizontal wind shear (Figure 4.2d), which allowed this event to be classified as a coupling between local forcing at low and high levels. In the event of 20170527, a ridge extending between the states of AL and PE favored the emergence of a trough in the ocean parallel to the coast of these states (Figure 4.2e). In the case of 20170614, it was possible to observe a disturbing wave in the geopotential field at 700 hPa and the westerly cloudiness motion coinciding with the trough axis at this level (Figure 4.2f). This configuration allowed the event to be classified as an EWD.

On the event day 20170623, a ridge was observed between the states of AL and PE (Figure 4.2g) and the intensification of SASA strengthened the trade winds, which characterized this mechanism as the main factor of the observed discrete cloudiness. In 20170627, the ridge system on the continent and the trough in the ocean appeared to be displaced in the continent and it was possible to observe an intense high-level runoff in a circulation that preceded the formation of a UTCV (Figure 4.2h). This high-level flow was preponderant in favoring cloudiness on the coast of PE. In the case of 20170719, two cloud cores were observed, the first on the coast of the PE and the second in the ocean, favored by two cores of high pressure in the middle layer (Figure 4.2i).

The event of day 20170724 presented discrete cloudiness with the surface ridge extending between the states of AL and PE (Figure 4.2j). At the 650 hPa level, a ridge was also observed over the state of PE favoring cloud formation. In 20180118, aligned high and low-pressure cores were again observed over the state of PE with the storm formation on

the coast and east of the surface ridge (Figure 4.2k). In the 20180217 event, the ridge system on the continent and trough in the ocean was again present (Figure 4.2l), in addition to a closed high-level anticyclonic circulation over PE. This coupling once again favored the development of the storm.

In the 20180306 event, the high pressure at the surface was again observed with two cores and shifted further north concerning the previous cases (Figure 4.2m). Again, this high-pressure system deflected the low-level trade winds and favored mass convergence and storm formation to the east of its position. In the case of 20180405, the high surface pressure was present and the northern periphery of a UTCV influenced the coast of the PE (Figure 4.2n). In the 20180410 event, the ridge at the interior of the PE state was present, as well as the deflection pattern of the surface air currents and intense cloudiness detached from the ITCZ (Figure 4.2o).

In episode 20180412, there was a closed high-level anticyclonic circulation with its western periphery influencing the coast of the PE. The PE ridge was displaced further to the coast, which allowed the formation of a westward trough and the formation of intense inland cloudiness (Figure 4.2p). In the case of 20180421, the surface ridge in the PE interior can be observed with intense cloudiness from the west (Figure 4.2q) and at high levels an intense zonal runoff and is therefore classified as a case of cloudiness detached from the ITCZ. By 20190203, the surface high-pressuree system was moving eastward with intense cloudiness on the coast (Figure 4.2r). This cloudiness was coming from the ITCZ with an intense runoff at altitude, which favored the penetration of a cloud pulse and the formation of the storm.

In 20190205, there was the formation of a core of high pressure in the central portion of PE associated with intense cloudiness originating from the ocean from the ITCZ position (Figure 4.2s). In the 20190412 event there was intense cloudiness along the entire NEB east coast, the high-pressure core appeared displaced to the north and low-pressure cores were observed aligned to the ITCZ (Figure 4.2t). In the 20190527 events, it was possible to observe the high-pressure system on the surface extending between the states of AL and PE with slight cloudiness on the southern coast of PE (Figure 4.2u).

Figure 4.2 – Weather analysis for the 24 cases studied in detail.

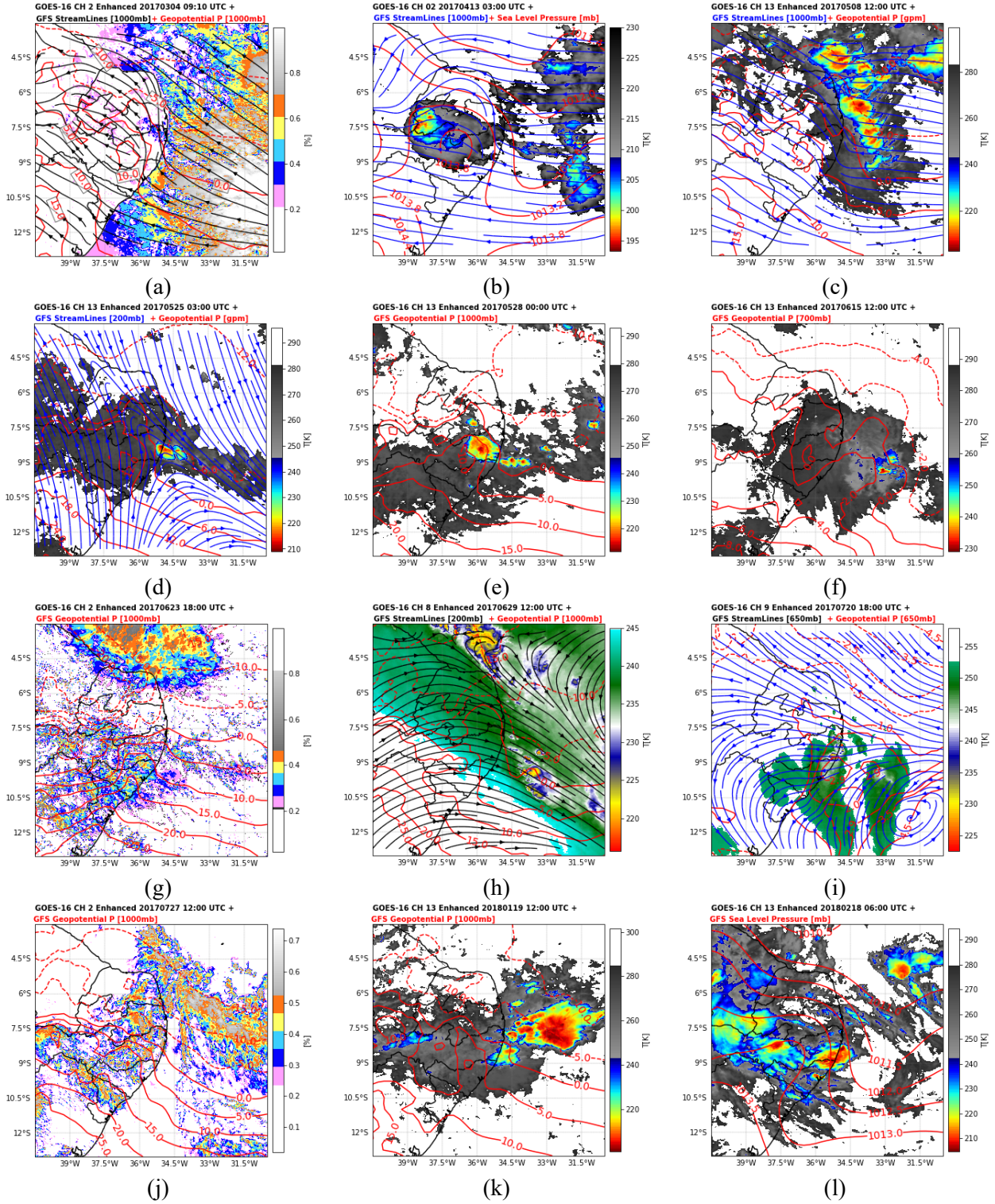

(continue)

Figure 4.2. Conclusion.

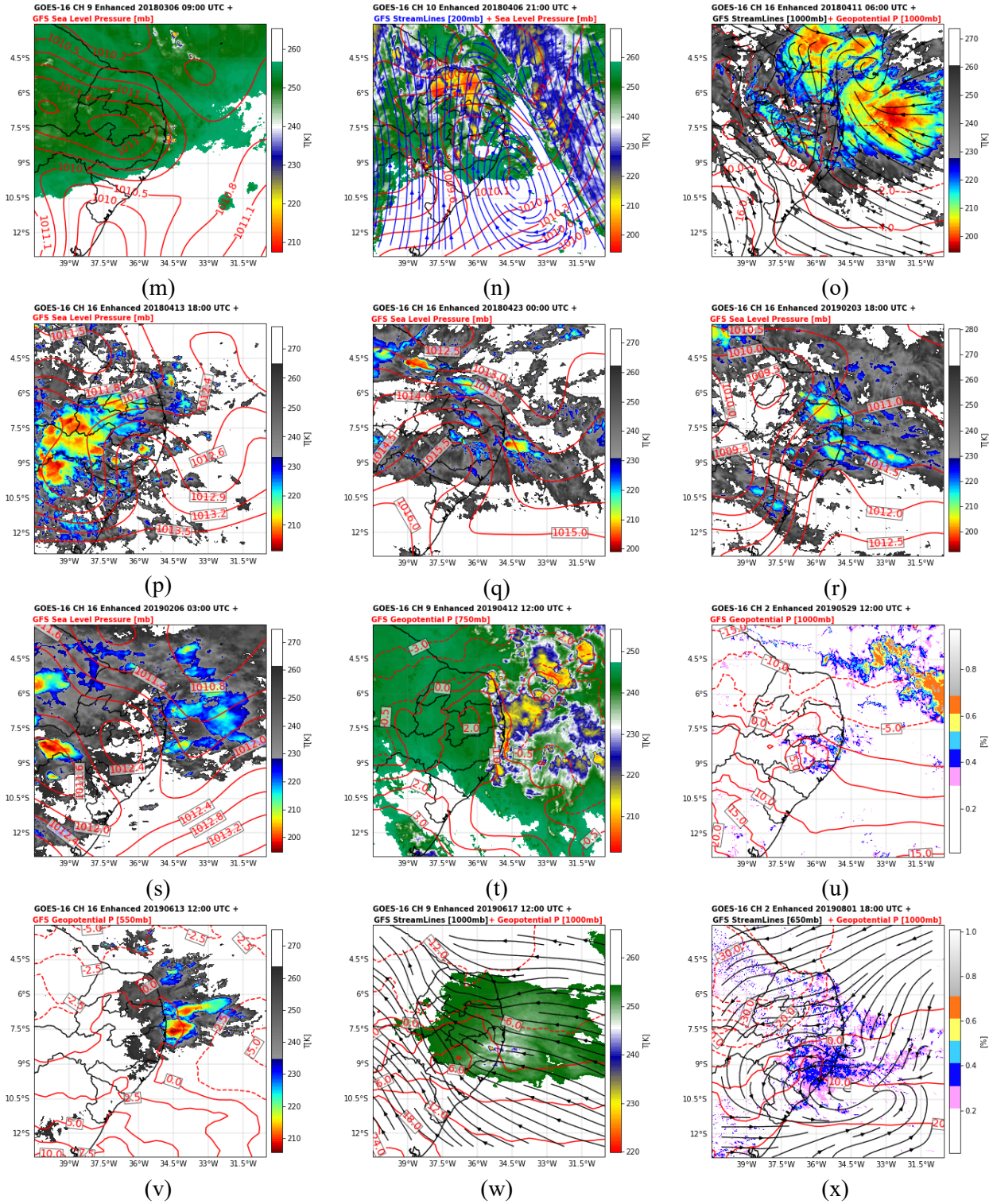

Cases (a) 20170303, (b) 20170412, (c) 20170507, (d) 20170524, (e) 20170527, (f) 20170614, (g) 20170623, (h) 20170627, (i) 20170719, (j) 20170724, (k) 20180118, (l) 20180217, (m) 20180306, (n) 20180405, (o) 20180410, (p) 20180412, (q) 20180421, (r) 20190203, (s) 20190205, (t) 20190412, (u) 20190527, (v) 20190612, (w) 20190614, and (x) 20190801.

On event day 20190612, a mid-layer ridge was observed extending across the states of AL, PE, and PB, with a storm acting on the coast to the east of this system (Figure 4.2v). In the case of 20190614, once again, the high-pressure system at the surface deflecting the runoff of the southeast trade winds was observed (Figure 4.4w). In case 20190801, a low-level ridge was observed between the states of AL and PE in addition to a medium-level cyclonic circulation-favoring cloud formation on the coast (Figure 4.4x).

The meteorological analysis identified two main sets of features associated with severe weather events. The first was composed of the synoptic systems acting in the region, and the second, which acts in the absence of some larger scale system, was composed of a mesoscale formation that can appear alone or associated with some other system.

The synoptic systems identified were ITCZ, EWD, UTCV and the high (HLF) and medium (MLF) layer flows that can also favor convergence at the surface and the development of severe thunderstorms according to wind shear (BROOKS; III; WILHELMSON, 1994). The second type of forcing identified was high pressure on the surface (HPS), sometimes with a closed isobar and sometimes in the form of a ridge and may be accompanied by other systems (HPS+), commonly positioned in the eastern portion between the states of AL and PE, but which was observed in all events and adjacent regions. The typical characteristics of the analyzed events gathered through meteorological, rainfall, and radar analysis can be seen in Appendix A, and the categorization of events by meteorological analysis in Figure 4.3.

ITCZ cloud pulses and mid-level runoff favoring convection at the surface were the highest frequency systems of the acting synoptic systems. This agrees with the results of Grodsky and Carton (2003), which show that the ITCZ can influence the east coast of the NEB. According to Kouadio et al. (2012), about 50% of severe rainfall episodes in the eastern NEB occur due to EWD acting in conjunction with trade winds leading to and strengthening the convective activity in the region. However, when we analyze the action of the southeast trade winds and the characteristics of EWD, only one episode could be classified as EWD, reducing the action of this synoptic system to less than 5% of cases responsible for large precipitation. A similar thought can be applied to UTCVs, where despite the central region of the PE being one of the main regions of action of this system

(SOUZA DOS REIS et al., 2021), in this study, only one case was identified (Figures 4.2n and 4.3).

Figure 4.3 – Categorization of the results for the meteorological analysis.

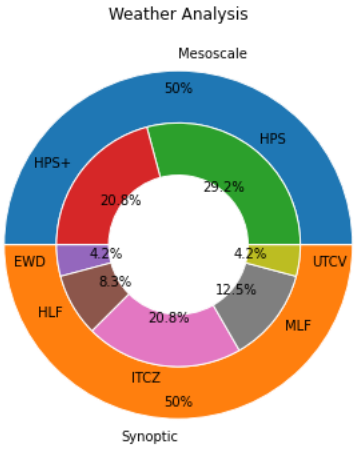

Events with synoptic features: ITCZ – intertropical convergence zone, EWD – easterly waves disturbance, UTCV – upper tropospheric cyclonic vortex, HLF – high layer flow, and MLF – medium layer flow. Events with mesoscale features: HPS – high pressure on the surface, and HPS+ – high pressure on the surface accompanied by other systems.

The mesoscale systems linked to severe rainfall were associated with high pressure at the surface that impeded the flow of the southeast trade winds, increasing the convergence of the moisture flux and favoring convection at low levels. In several cases, the trade winds colliding with this local high-pressure system were deflected into a cyclonic turn of the winds where the region of highest cloudiness was observed. This system was observed in all cases, however, when in the presence of a larger scale circulation, it overlapped with the local system. This mechanism, alone or accompanied by other factors, was observed in 50% of cases (Figure 4.3).

One hypothesis, that needs to be better explored, for the high surface pressure on the east coast of the NEB may be related to the phases of the Atlantic Multidecadal Oscillation (AMO) and its influence on the anomalous behavior of Atlantic Walker and Hadley cells (SHIMIZU; ANOCHI; KAYANO, 2022). These authors found that convection associated with the upward branch of a Walker cell over the Amazon contributed to the strengthening of the hydrological cycle in northern Brazil and intensified downward movements in the northeastern, the same with the Hadley cell that has an upward moving

core around 7°N and a strong downward branch with a core around 7°S. Reboita et al. (2016) identified that besides the Walker and Hadley cells, the Borborema plateau, a group of highlands between the states of AL, PE, PB, and RN with an average height of 200 m, but with peaks that can exceed 1000 m, also exerts an influence on the semi-aridity of the region, especially when the wind flow is coupled with the downward movements of the general circulation cells of the atmosphere. This air subsides over the area allowing the thermal equilibrium, heating the lower layers by adiabatic compression, and favoring the high pressure at the surface (CHARNEY, 1975).

4.2 Pluviometric analysis

Figure 4.4 shows the spatial distribution of rainfall in the 293 rain gauges studied, the positions of maximum rainfall and the municipalities with confirmation of natural disaster phenomena. It is possible to see that some episodes reach large extensions (Figure 4.4 – b, d, e, f, h, i, l, n, p, q, s, v, and w) while others occur on a smaller scale (Figure 4.4 – a, c, g, j, k, m, o, r, t, u, and x). Local-scale events can also exceed accumulations greater than 100mm as in cases 4.4u and 4.4r, as well as larger events may not reach that mark, as in case 4.4s.

Figure 4.4 – The spatial distribution of precipitation for all cases studied.

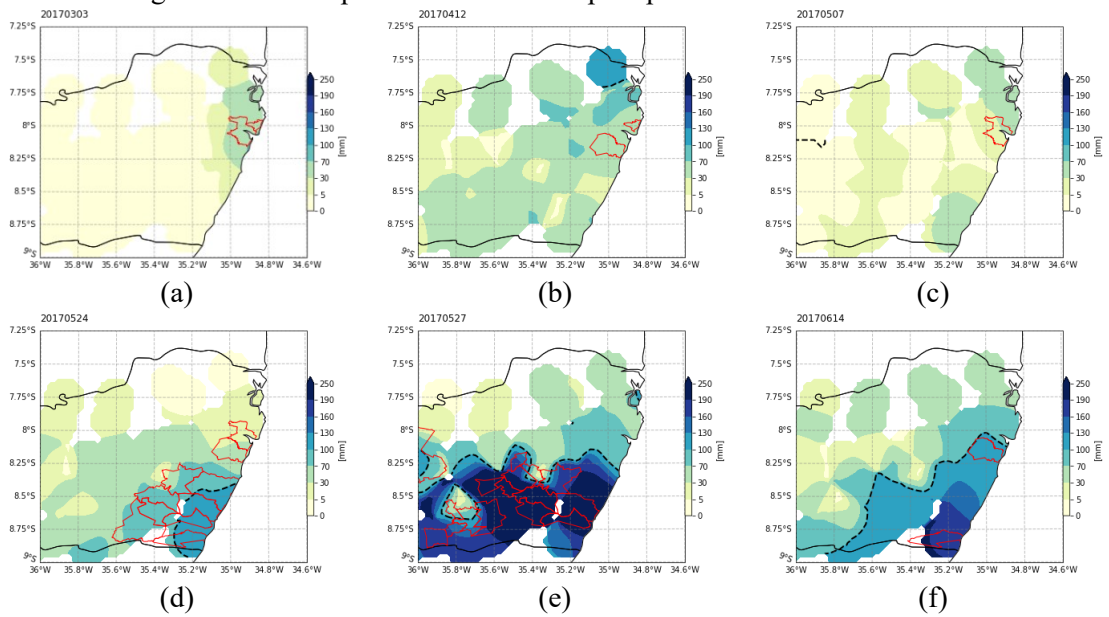

(a) (b) (c)

(d) (e) (f)

(continue)

Figure 4.4 – Continuation.

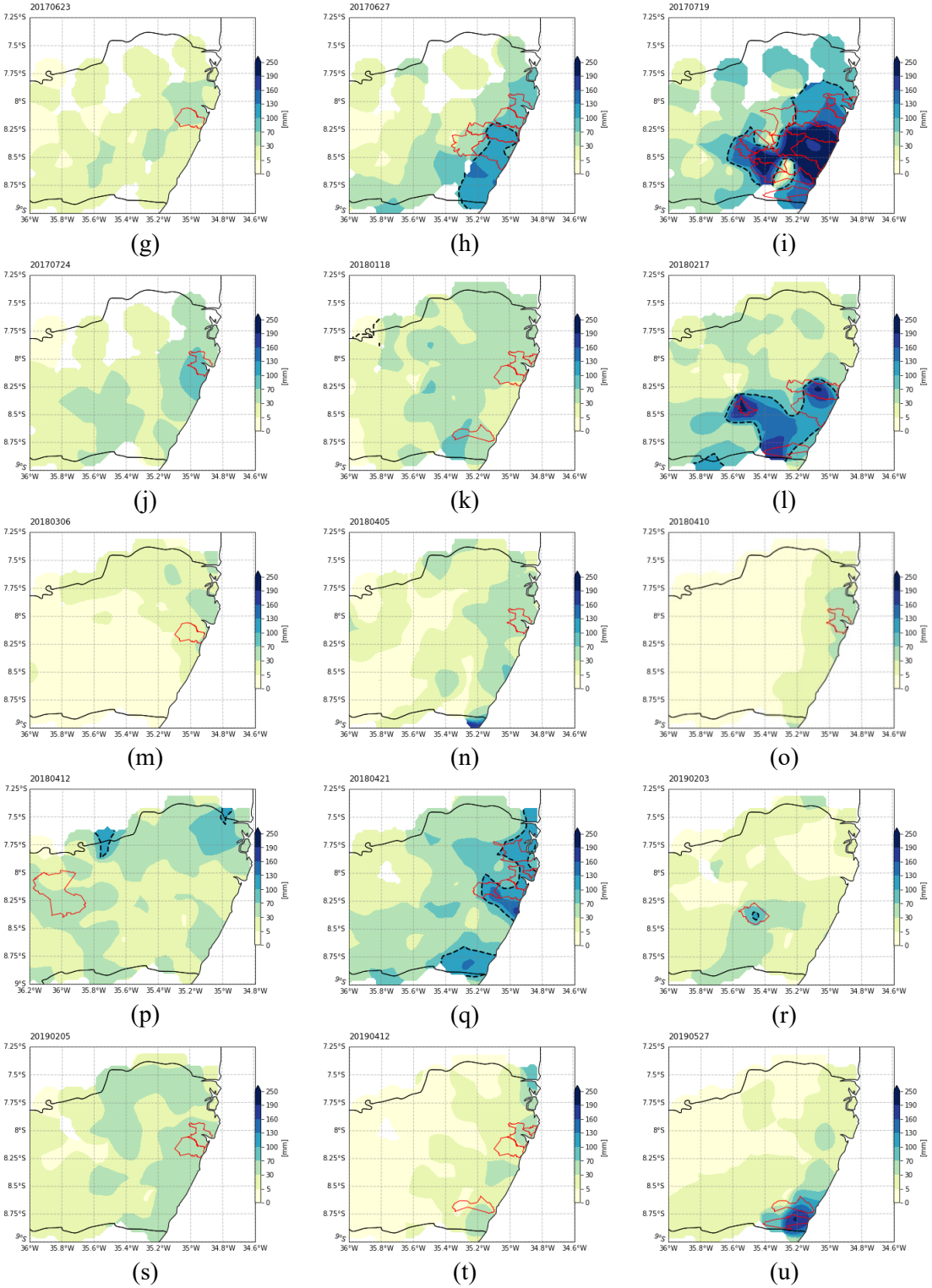

(continue)

Figure 4.4 – Conclusion.

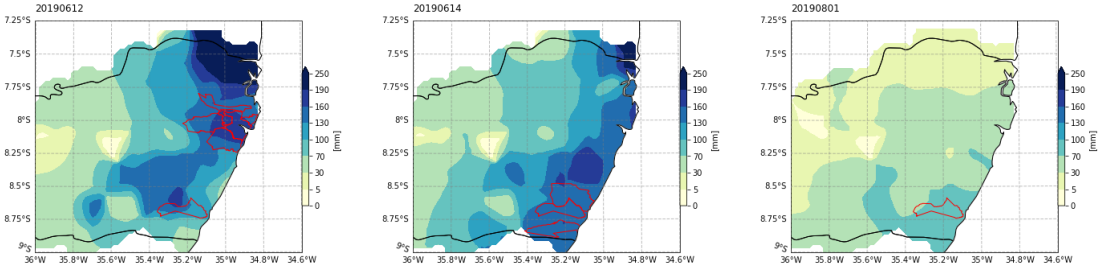

(v) (w) (x)

The total time of the accumulations can be seen in Appendix A and the corresponding time analysis in Figure 4.5. The red polygons are the municipalities affected by natural disasters. The black dotted line represents the 100-mm isohyet.

Figure 4.5 shows the temporal distribution of rainfall in a 0.4 x 0.4 degree latitude and longitude region over the intersection position between the highest accumulations and the alerted municipalities. Through the analysis of these temporal sections, it was possible to group the events into short and long duration, when they lasted less or more than 24 h, in low, high, and very high-intensity events, when rainfall records were below 10 mm/10min, when they were between 10 and 15 mm/10min, and when they were above 15 mm/10min, respectively. And whether the precipitation was continuous or spaced, when there was an interval with no rain longer than 1 h.

Figure 4.5 – The temporal distribution of rainfall for the 24 events studied at the intersection positions between the highest spatial accumulation and the alerted municipalities.

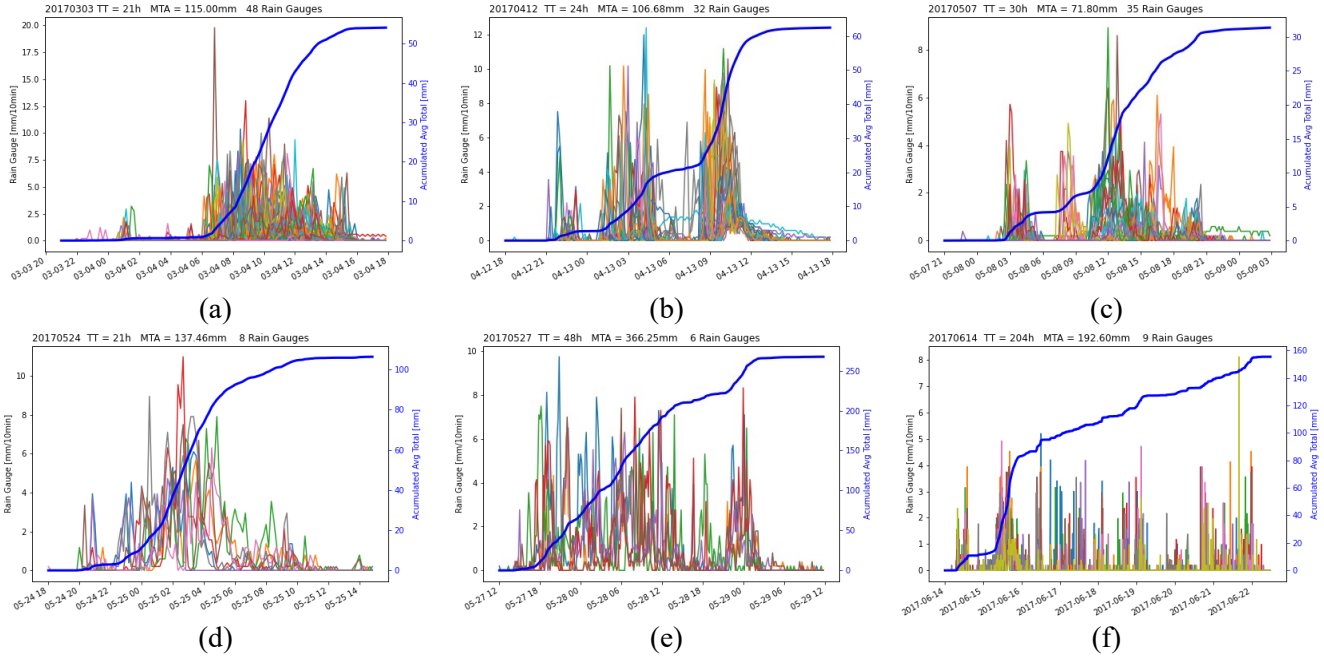

(a) (b) (c)

(d) (e) (f)

(continue)

Figure 4.5 – Continuation.

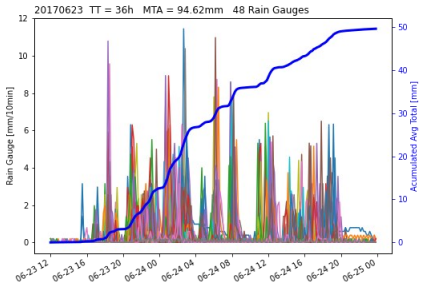

(g)

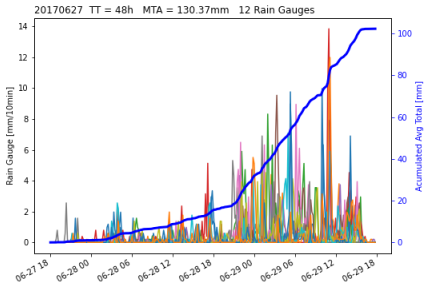

(h)

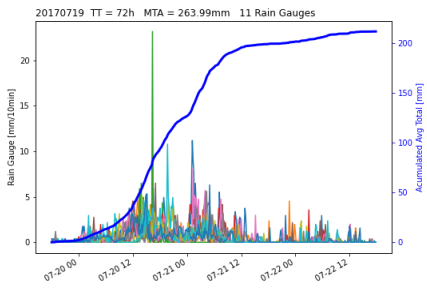

(i)

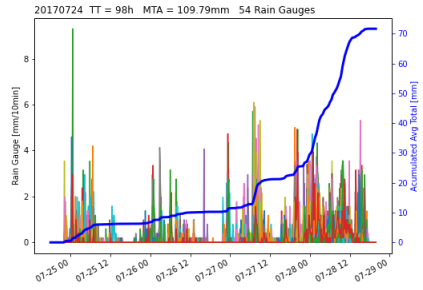

(j)

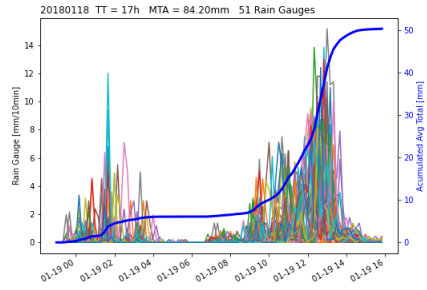

(k)

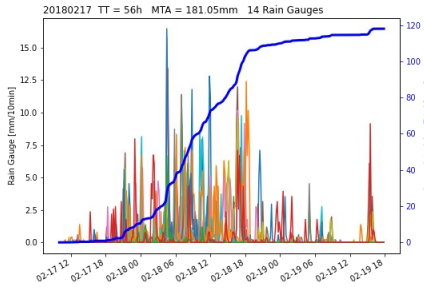

(l)

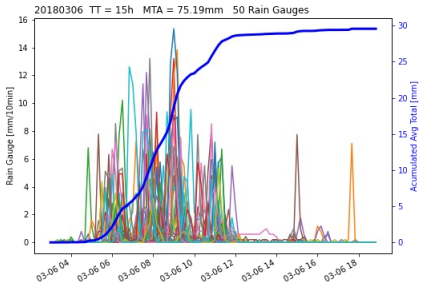

(m)

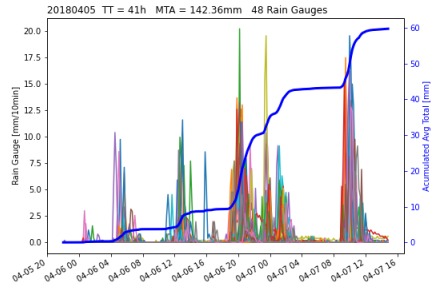

(n)

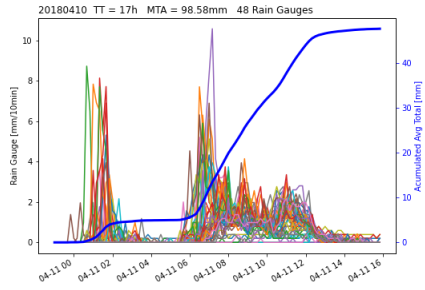

(o)

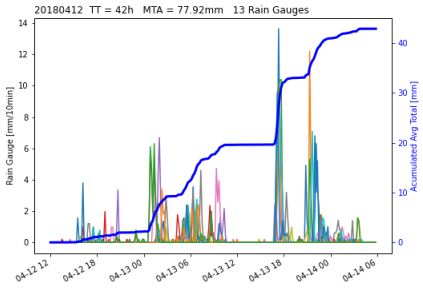

(p)

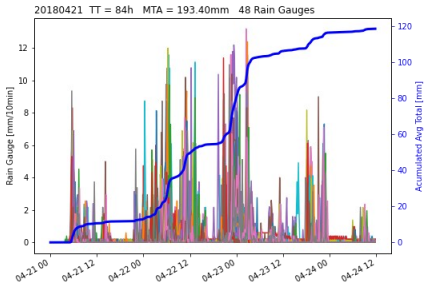

(q)

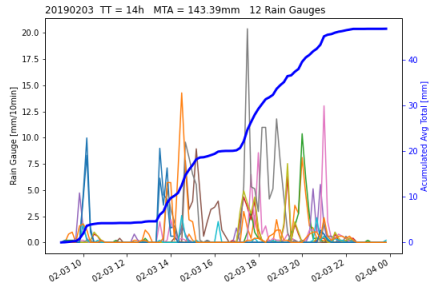

(r)

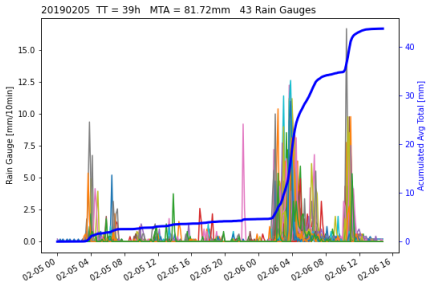

(s)

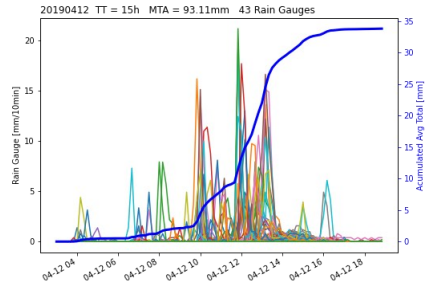

(t)

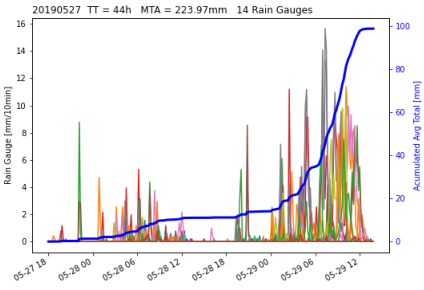

(u)

(continue)

Figure 4.5 – Conclusion.

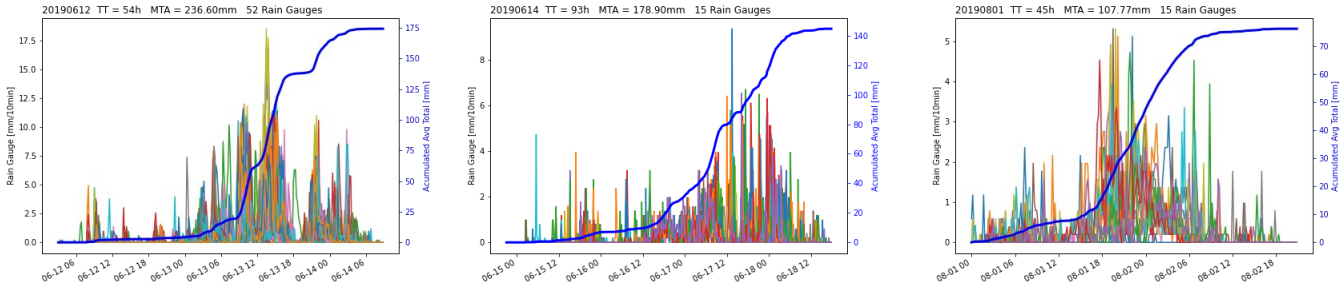

(v) (w) (x)

TT means the total time of rainfall duration and MTA is the maximum total accumulated in a rain gauge. Each rain gauge represents a different color (mm/10 min) and average accumulated precipitation for the period in blue.

Following this classification, it was observed that more than 60% cases were of long duration, about 42% of cases had very high precipitation rates, 33% had high rates and 25% low rates, and most of the rainfall (~60%) occurred at spaced or short intervals.

Figure 4.6 - Relationship between total accumulated rainfall and the duration of the event.

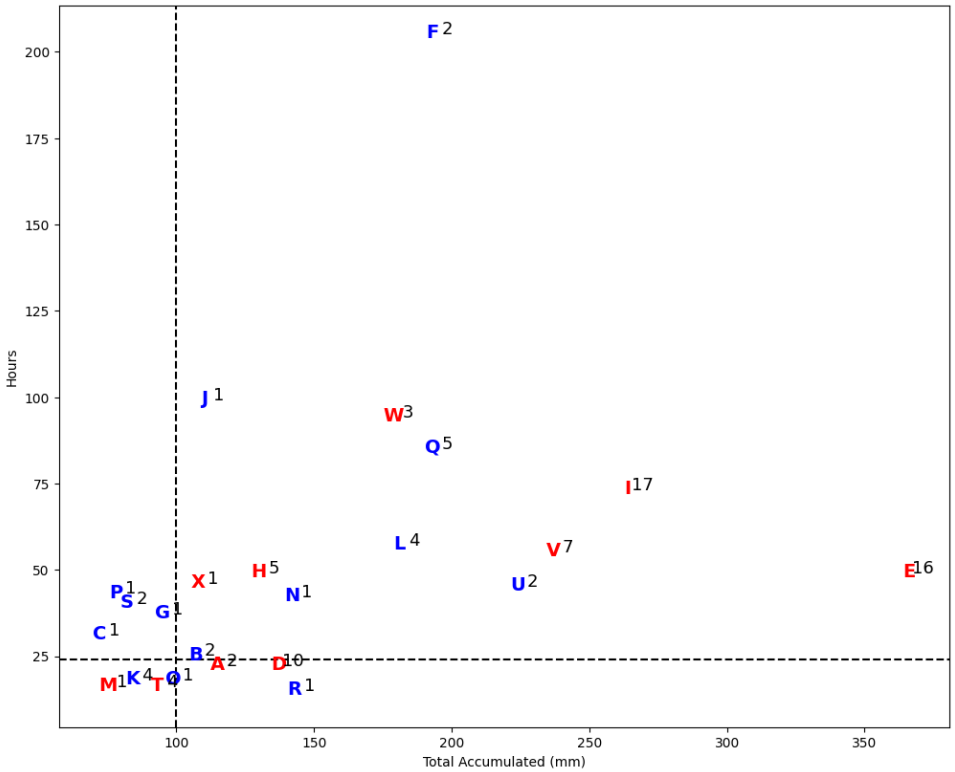

The letters refer to the events studied as identified in Figure 4.2. The colors indicate the type of event's precipitation with red events classified as continuous rain and blue as spaced-out rain. The numbers are the quantity of affected municipalities. The dotted lines mark the accumulation of 100 mm and the duration of 24 h.

The events that reached a large spatial coverage or the greatest number of municipalities presented continuous rainfall, with large accumulations and in a time interval generally less than 72 h (Figure 4.6). Event D, which showed constant rainfall with a duration of less than 24 h and a total accumulation around 140 mm, affected 10 municipalities and was therefore considered more severe than other events with higher accumulations. Event F, on the other hand, lasted about 200 h with spaced rainfall and total accumulations around 200 mm, but affected only two municipalities. In general, long duration events can have both high and low intensity, but occur mainly in a spaced manner. On the other hand, short-duration events are either continuous or spaced (Figure 4.6).

4.3 Radar analysis

Through the radar reflectivity (Figure 4.7), it was observed that most of the storms come from the eastern sector (southeast, east, and northeast), i.e., the ocean, and only two cases showed reflectivity cores moving from north. Vertical reflectivity sections were also constructed at the position and instants of the highest precipitation observed by the rain gauges (Figure 4.9). These vertical sections allowed us to identify that in 16 cases the maximum reflectivity cores were concentrated in a layer up to the height of 2000 m and in the remaining 8 cases the height of the highest reflectivity was between 3000 m and 5000 m. Additionally, in most events (21 cases), the radar reflectivity exceeded the height of 5000 m and in only 3 cases it was below that level (Figure 4.9).

It was also possible to group the cases according to the spatial distribution of reflectivity into isolated single-cell events (UNI – unicellular), events composed of small-sized multicell (MULT – multicellular), and events composed of large single-cell cells accompanied by other smaller nuclei (UNI+ – unicellular plus). This analysis showed that half of the cases are made up of several small-sized cells, while 37.5% of the cases are made up of large nuclei accompanied by smaller cells, and the minority are single convective cells.

Figure 4.7 – Radar reflectivity for all cases studied.

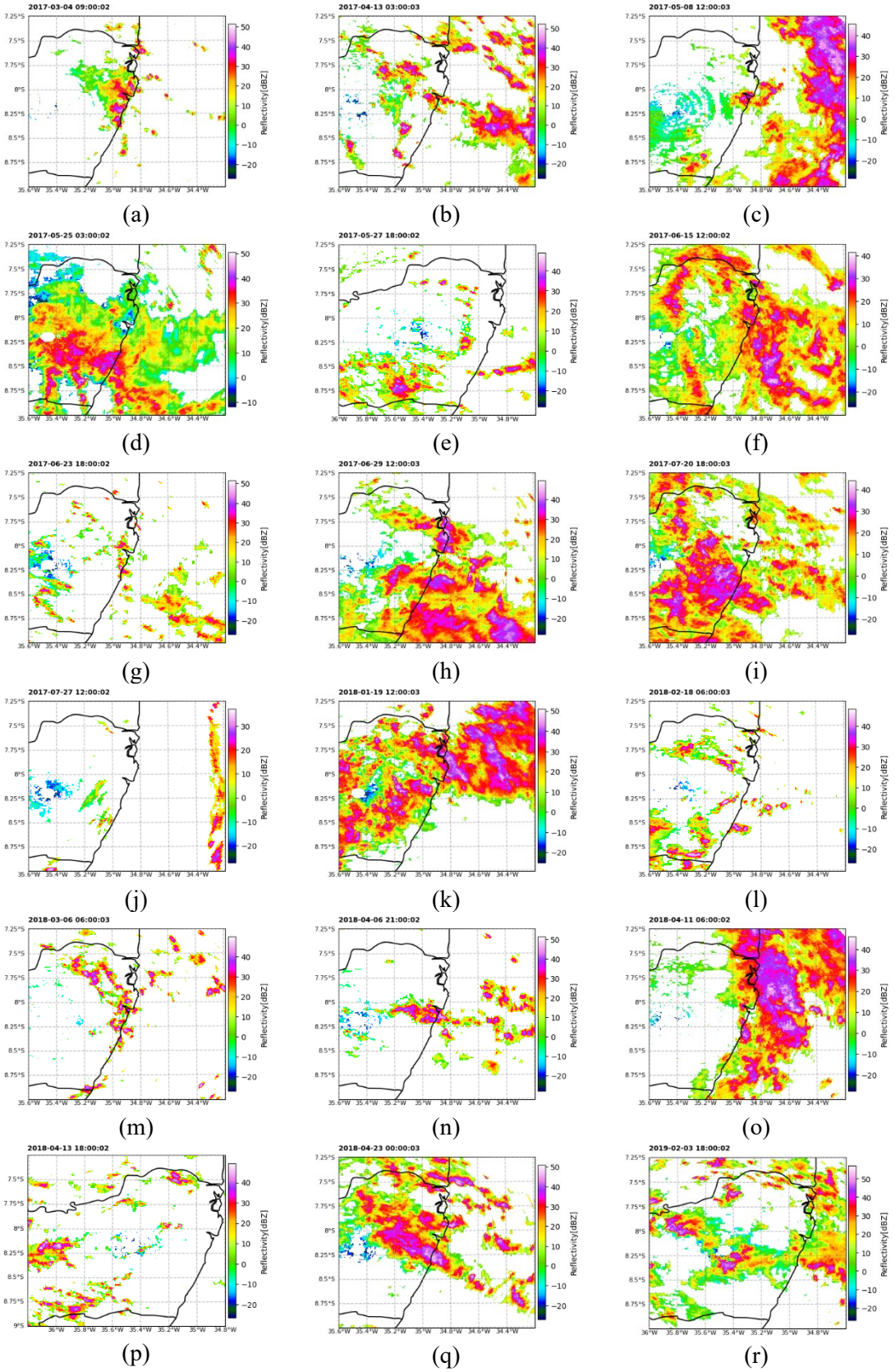

(continue)

Figure 4.7 – Conclusion.

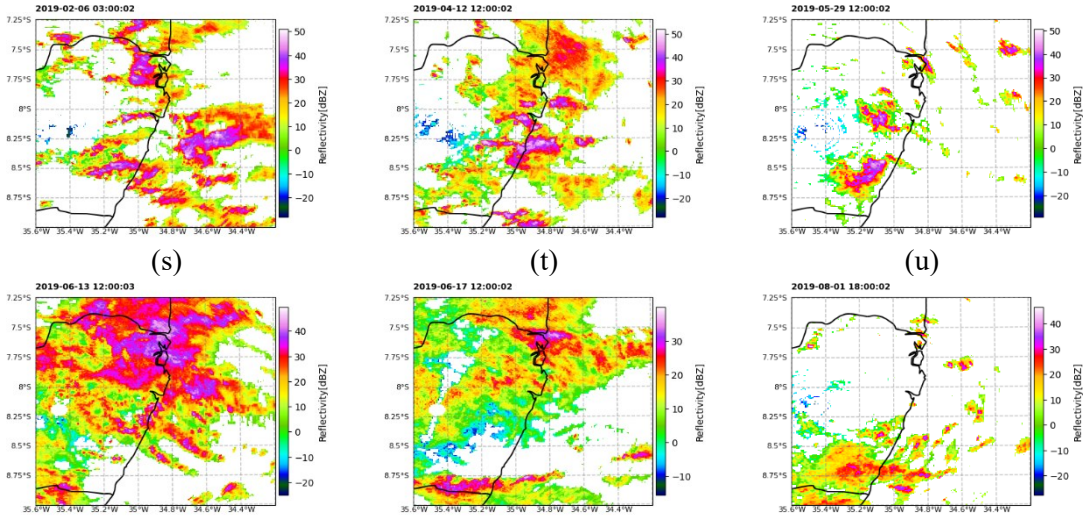

(s) (t) (u)

(v) (w) (x)

CAPPI at 2000 meters.

The analysis of the radar data allowed us to group the cases into events that presented several small reflectivity cores, storms with single cells and systems with one large cell accompanied by several smaller cells (KOLODZIEJ HOBSON et al., 2012) (Figure 4.8). The vast majority of storm cells move from the eastern sector and exhibit their maximum vertical reflectivity confined in the layer up to 2000 m (KUMAR; BHAT, 2016).

Figure 4.8 - Grouping of storms according to their morphology and preferred direction of movement (backward trajectories).

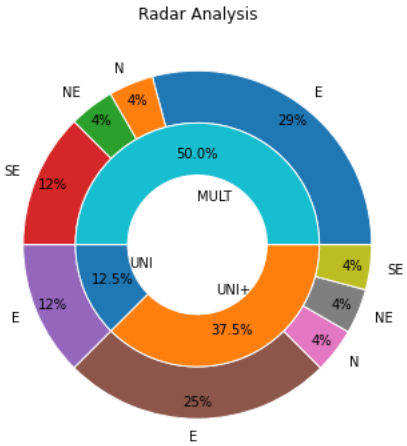

Spatial distribution of reflectivity: UNI – unicellular, MULT – multicellular, and UNI+ – unicellular plus. The preferred direction of movement: E – east, SE – southeast, N – north, and NE – northeast.

Figure 4.9 – Vertical radar reflectivity sections for each case analyzed.

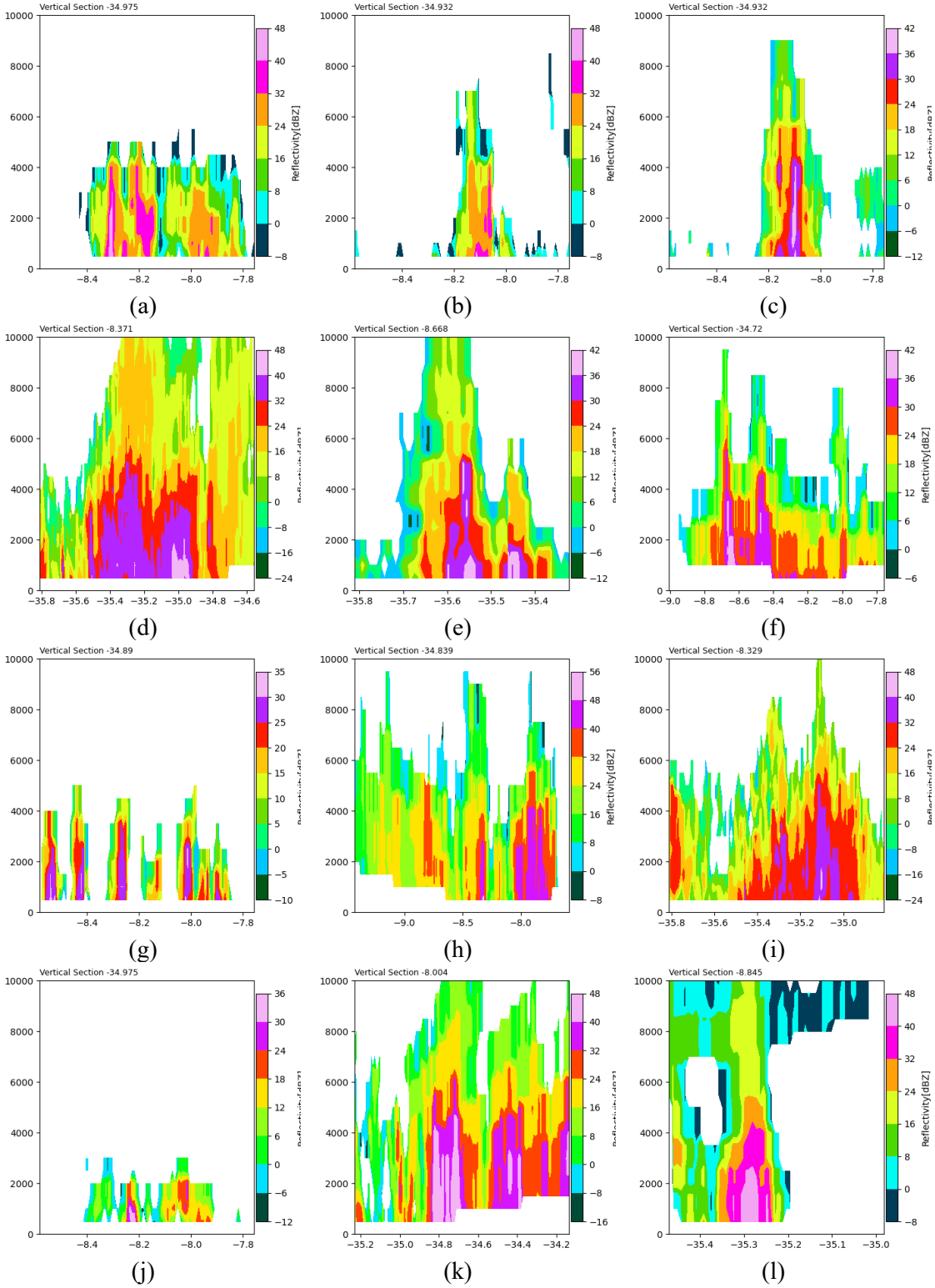

(continue)

Figure 4.9 – Conclusion.

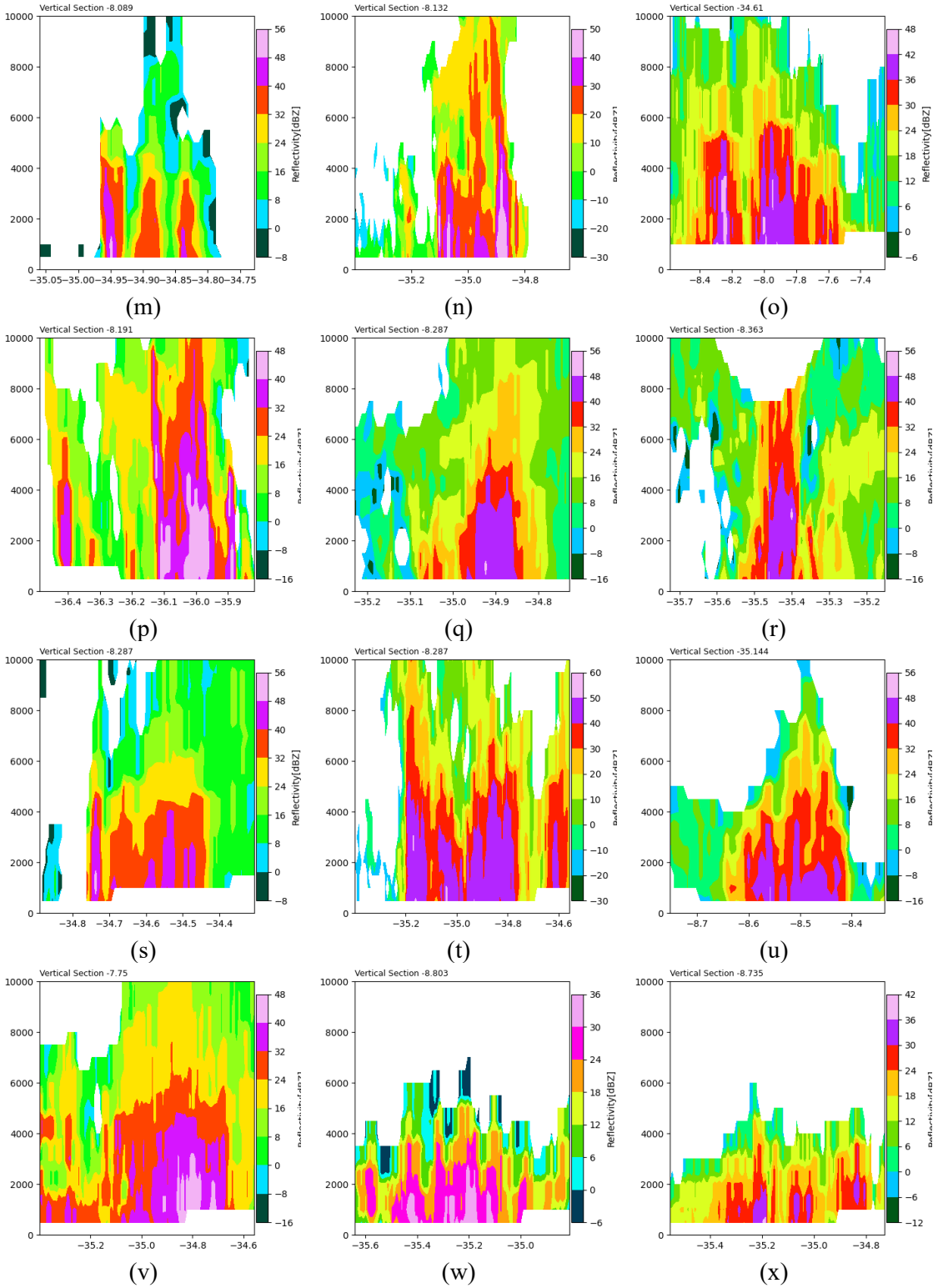

Vertical reflectivity sections over the storms at or near the instants of highest precipitation rates.

5 NUMERICAL ANALYSIS

5.1 Weather conditions of the selected events

The four episodes of severe rainfall chosen for the numerical simulations were classified as (1) 20170528, event (e) in the synoptic and mesoscale analysis, a mesoscale convective system (MCS) with a trough on the surface parallel to the coast (Figure 5.1a) with strong wind divergence at 800hPa and intense near-surface MFC (Figure 5.1b); (2) 20170720, event (i), an isolated system with less cloudiness than in the previous case, positioned to the east of a ridge and favored by a confluence of high-level winds (Figure 5.1c) with again a strong wind divergence at 750hPa and presence of a small MFC near the surface (Figure 5.1d); (3) 20180422, event (q), an intense outflow embedded in pulses of ITCZ cloudiness from the northern NEB coast (Figure 5.1e) with strong wind divergence at 750hPa (Figure 5.1f); (4) 20190529, event (u), an isolated storm formed due to the presence of a ridge on the east between the states of Alagoas and Pernambuco, forcing a cyclonic wind curvature near the surface (Figure 5.1g) and presence of strong wind divergence at 800hPa and weak MFC at the surface (Figure 5.1h).

Figure 5.1 – Synoptic and mesoscale analysis of simulated severe rainfall events.

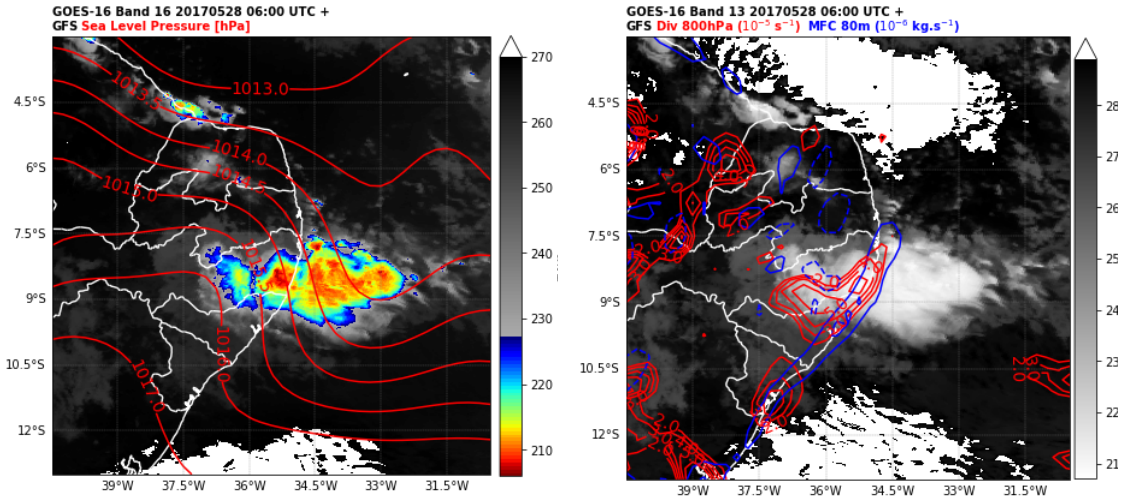

(a) (b)

(continue)

Figure 5.1 – Conclusion.

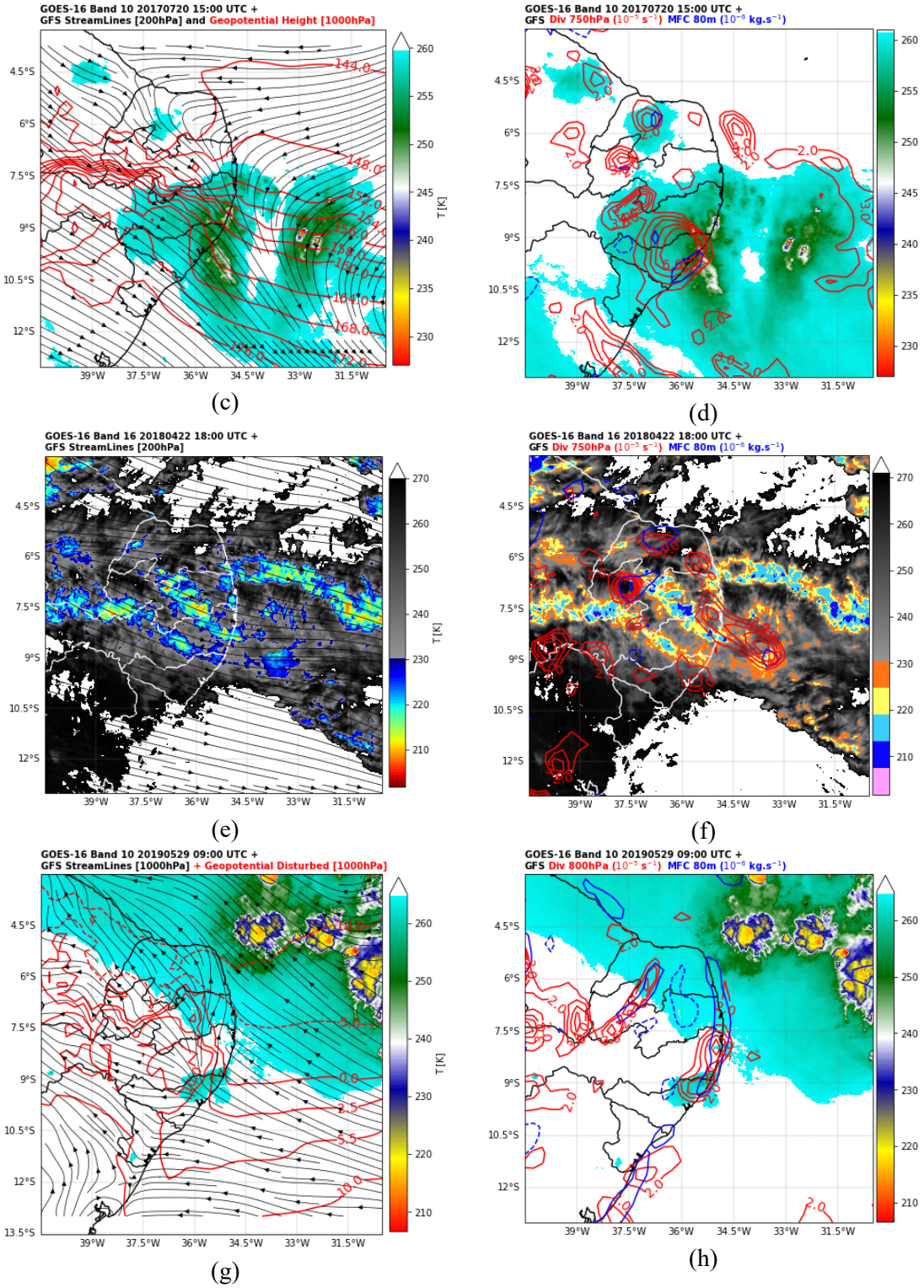

Synoptic and mesoscale analysis of simulated severe rainfall events: satellite images (a) and (b) on the enhanced infrared channel (13.3 μ and 10.35 μ), (c) and (d) on the enhanced water vapor channel (7.4 μ), (e) and (f) on the enhanced infrared channel (13.3 μ), (g) and (h) on the enhanced water vapor channel (7.4 μ). The meteorological fields are described in the figures.

Events 1 and 2 were associated with rainfall in large spatial extents, whereas events 3 and 4 were rainfall events concentrated in smaller regions. In all events, strong mass divergence was observed between the 850 hPa and 600 hPa levels, generally with a maximum at the 750 hPa level, on the order of 6.0 to 10.0 × $10^{-5}s^{-1}$. This strong divergence in the low- to mid-level layer was almost always accompanied by convergence in the lower layer, around 900 hPa, with the maximum core on the order of −7.5 to −15.0 × $10^{-5}s^{-1}$ (Figures not shown).

In event 1, starting on May 26 at 20UTC, the cloudiness began to intensify on the coast and subsequently expanded inland after being stationary in the coastal area all day on May 27. At high levels, there was diffluence of air currents and the proximity of the subtropical jet stream (FEDOROVA; LEVIT; CAMPOS, 2018). Near the surface, there was a trough parallel to the coast and an intense convergence of moisture flow from the ocean. This event showed local and synoptic scale characteristics and weak coupling between the high and low troposphere. The intense precipitation developed mainly locally, and the main elements for its maintenance were the trough at low levels near the coast and strong wind flow also in the low layer, as well as the strong MFC in the low layer and the strong wind divergence at the 800mb level (Figures 5.1a and 5.1b).

For event 2, the cloudiness was more discrete compared to the previous case. A ridge between the states of Alagoas and Pernambuco with an intense temperature gradient to the north was observed. Earlier that same day, there were upper tropospheric cyclonic vortices at altitude (DE MORAIS; GAN; YOSHIDA, 2021), with a core in the state of Maranhão and an eastern periphery influencing the coast of Pernambuco with a wind diffluence zone at upper levels. In the satellite images, it was possible to observe the westward advance of two cloud cores in the water vapor channel. However, no wave characteristics were observed at low or medium levels related to the position of these cores (GOMES et al., 2015). This event was characterized by the concentration of cloudiness to the east of the surface ridge, well-related to the position of maximum precipitation, a confluence zone of high-level winds with reduced intensity compared to the previous case, strong wind divergence at the 700hPa level, and MFC in the low layer with also reduced intensity compared to the previous case (Figures 5.1c and 5.1d).

For event 3, the outflow in the high levels was essentially westerly, with intense cloudiness, observed up to three days before the intense precipitation coming from the northwest. This cloudiness was associated with the presence of the ITCZ with entirely meridional outflow at high levels with strong wind divergence in 700hPa, weak MFC in the low levels, and presence of widespread cloudiness and precipitation (Figure 5.1e and 5.1f).

At the beginning of event 4, there was a closed anticyclonic circulation at high levels (Figure not shown). Even after the weakening of this circulation, an isolated storm formed to the east of a small surface ridge and intense flow perpendicular to the coast supporting a strong divergence in the 800hPa followed by a weak MFC in the low layer. The position of the surface moisture core, observed by the satellite image in the water vapor channel, the divergence above that core, and the ocean moisture supply coincided with the position of maximum precipitation (Figures 3.4d, 5.1g and 5.1h).

Synoptic and mesoscale analysis showed that events 1 (20170528), 2 (20170720), and 4 (20190529) were associated with high surface pressure, which contributed to the formation of thunderstorms to the east of its position, and with the intense trade winds that generally reach the coast perpendicularly and contribute to near-surface ocean moisture flux convergence. However, event 3 (20180422) was under the influence of ITCZ, which brought pulses of intense cloudiness from the north of the region. This analysis corroborates the results of Espinoza et al. (2021) for event 1, where the contribution of the ocean moisture flux to the heavy precipitation is indicated, and also the results of Gomes et al. (2015) for event 2, where it is stated that more than half of the tracked relative vorticity centers moving westward over the ocean are not classified as easterly wave disturbances. In all events, the presence of a strong wind divergence averaged over the layer between 800 hPa and 600 hPa with a strong low level convergence was observed and appeared to be fundamental to the occurrence of severe thunderstorms in this region.

5.2 Numerical simulations analysis

The 24-h simulation of event 1 was performed between 20170527 12UTC and 20170528 12UTC and totaled 69 runs. This event was the only one in which the best physical combinations reproduced a total average accumulation with an RE of around 50%. The

Thompson and TpsonAA MPHs were the best (Figures 5.2a, 5.3a, and 5.4a), with the Taylor diagram indicating Thompson first (Figure 5.4a). The two worst schemes were those with hail as the hydrometeor class (WSM7 and WDM7). The PBL TEMF scheme overestimated the rainfall by more than 200%, whereas the others underestimated it by around 80%. MYJ showed the best RE and the lowest bias (Figures 5.2b, 5.3b, and 5.4b). Turning on the cumulus parameterization, the KainF, G3, and KFCuP schemes were able to reproduce rainfall better, with KFCuP being the best (Figures 5.2c, 5.3c, and 5.4c). The RUC surface scheme showed the best RE and bias values (Figures 5.2d and 5.3d).

Figure 5.2 – Average hourly accumulated rainfall at the rain gauges and the rainfall generated by the model for the simulated event 1.

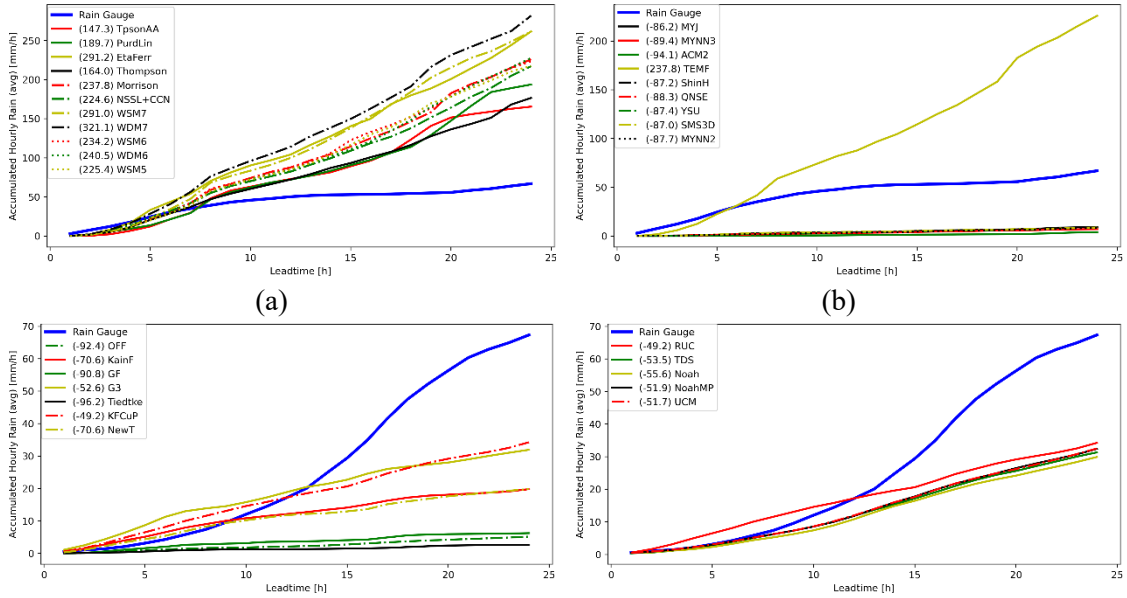

Relative errors: (a) microphysics settings, (b) the planetary boundary layer, (c) cumulus, and (d) surface parameterizations. Comparison of the average hourly accumulated rainfall at the rain gauges with the rainfall generated by the model according to the settings under analysis. Inside the legend are REs accumulated over 24 h for each configuration.

Figure 5.3 – Average hourly bias between the mean values calculated by the model and the mean values observed by rain gauges for event 1.

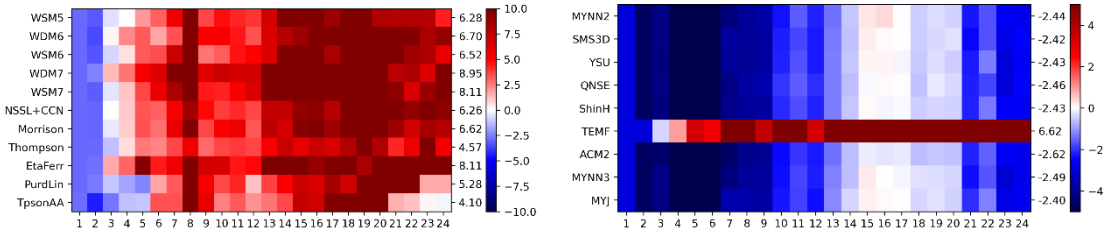

(continue)

Figure 5.3 - Conclusion

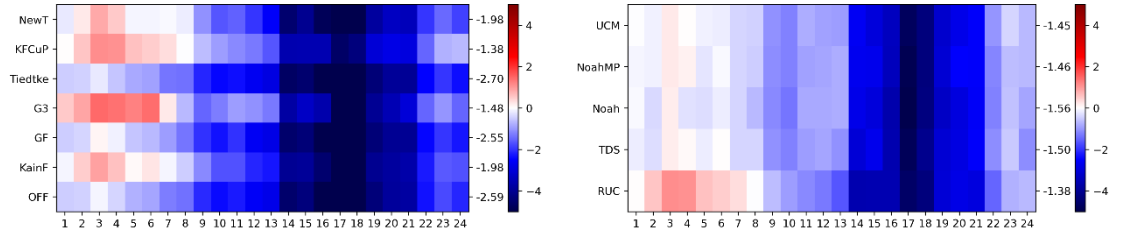

(c) (d)

(a) microphysics settings, (b) the planetary boundary layer, (c) cumulus, and (d) surface parameterizations. The colors show the average hourly bias and on the secondary axis the average period bias.

Figure 5.4 – Taylor diagram for event 1 settings.

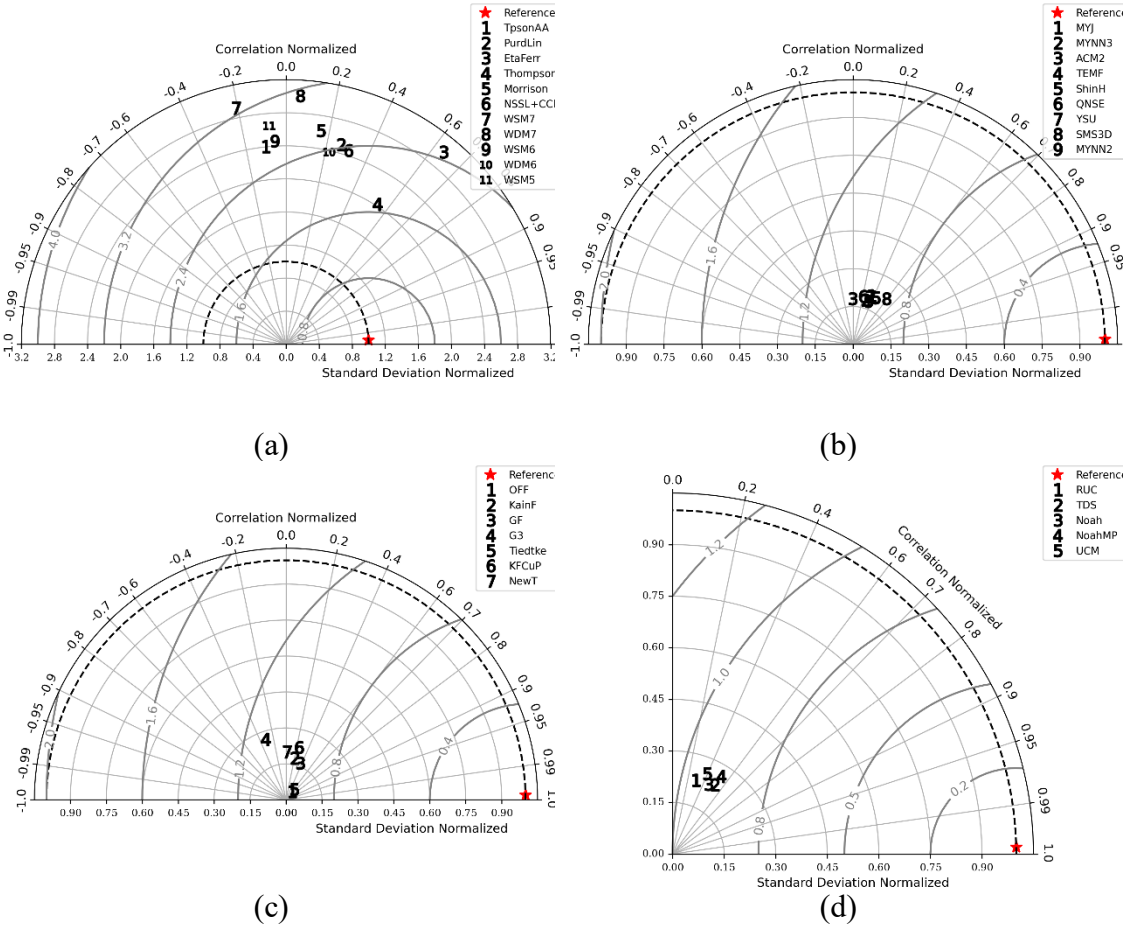

(a) (b)

(c) (d)

(a) microphysics settings, (b) the planetary boundary layer, (c) cumulus, and (d) surface parameterizations. The numbers correspond to the tested physical schemes.

The simulations for event 2 were performed between 20170720 00UTC and 20170721 00UTC and totaled 30 runs. The three best MPHs were NSSL + CCN, EtaFerr, and TpsonAA, whereas WDM7 and WDM6 produced almost no rainfall (Figures 5.5a, 5.6a, and 5.7a). For the PBL, again TEMF caused an overestimation and ACM2 was the best in terms of the RE and bias (Figures 5.5b, 5.6b, and 5.7b). Again, when the cumulus parameterization was turned on, the KainF, G3, and KFCuP schemes were able to better represent the rainfall (Figures 5.5c, 5.6c, and 5.7c). For the surface schemes, UCM showed better RE and bias values than RUC, but the RUC showed better values according to the Taylor diagram (Figures 5.5d, 5.6d, and 5.7d).

Figure 5.5 – Average hourly accumulated rainfall at the rain gauges and the rainfall generated by the model for the simulated event 2.

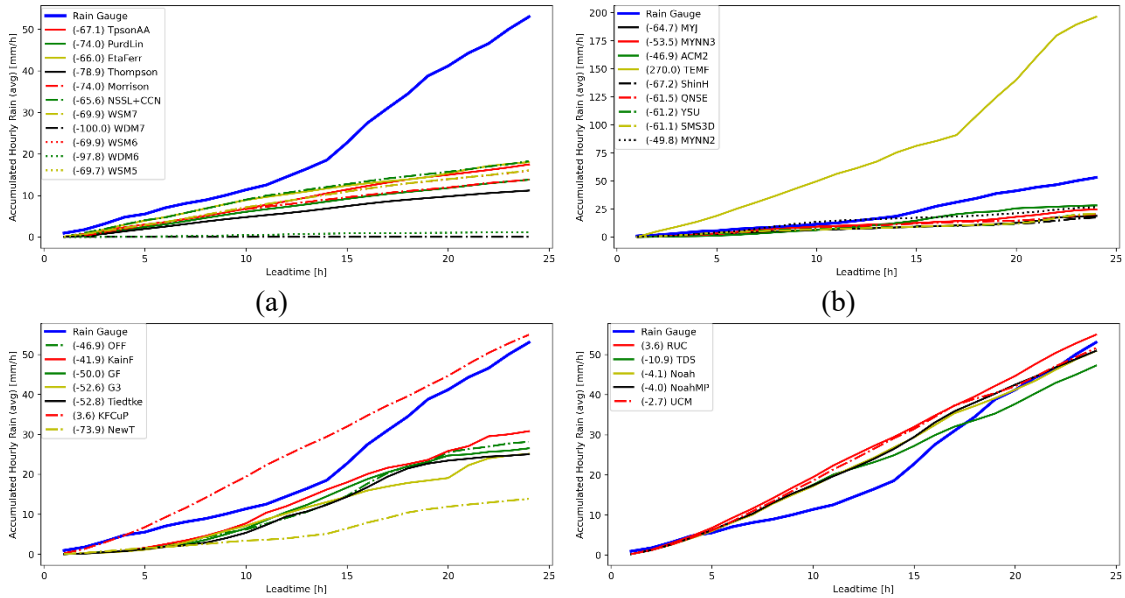

Relative errors: (a) microphysics settings, (b) the planetary boundary layer, (c) cumulus, and (d) surface parameterizations. Comparison the average hourly accumulated rainfall at the rain gauges with the rainfall generated by the model according to the settings under analysis. Inside the legend are REs accumulated over 24 h for each configuration.

Figure 5.6 – Average hourly bias between the mean values calculated by the model and the mean values observed by rain gauges for event 2.

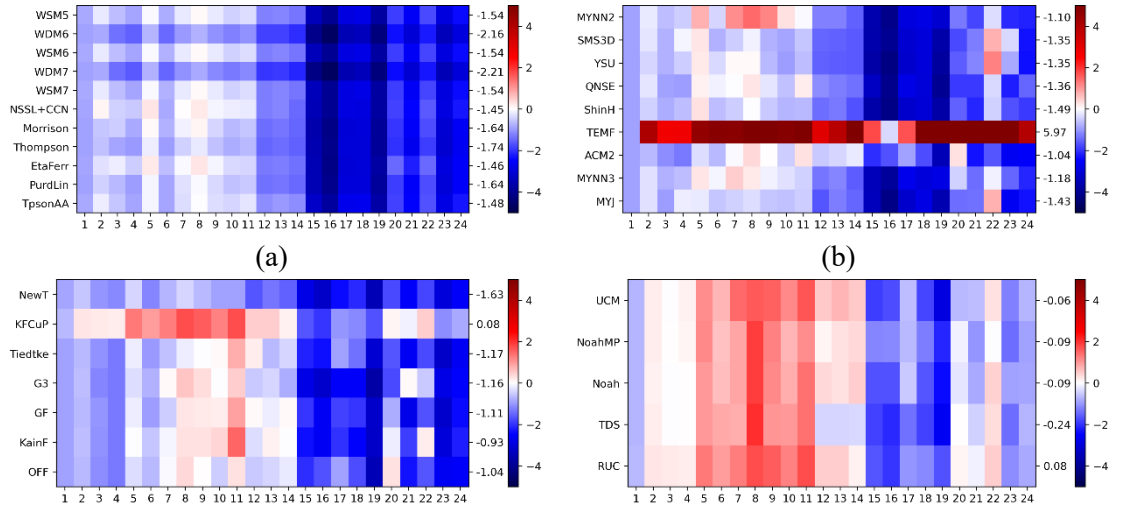

(a) (b)

(c) (d)

(a) microphysics settings, (b) the planetary boundary layer, (c) cumulus, and (d) surface parameterizations. The colors show the average hourly bias and on the secondary axis the average period bias.

Figure 5.7 – Taylor diagram for event 2 settings.

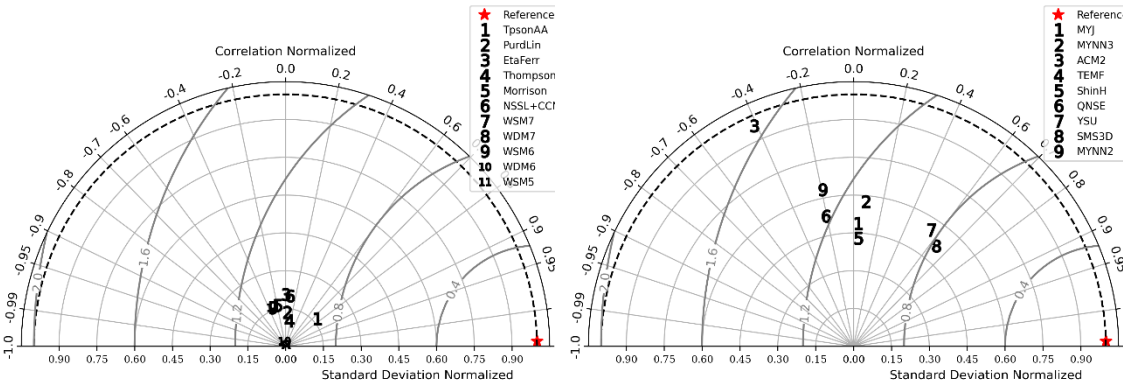

(a) (b)

(continue)

Figure 5.7 – Conclusion.

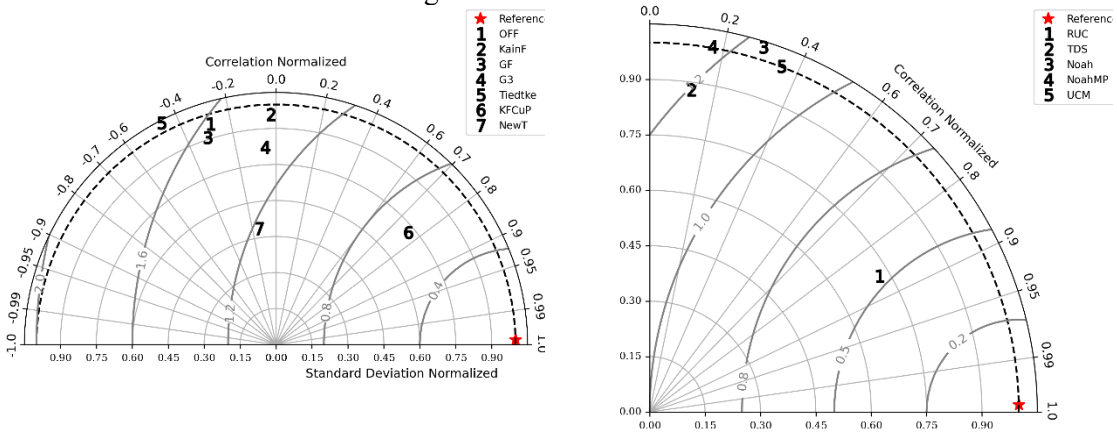

(c) (d)

(a) microphysics settings, (b) the planetary boundary layer, (c) cumulus, and (d) surface parameterizations. The numbers correspond to the tested physical schemes.

The simulations for event 3 were performed in the period from 20180422 00UTC to 20180423 00UTC and totaled 28 runs. The best MPHs were NSSL + CCN, WDM6, and TpsonAA; and the worst, again, were WSM7 and WDM7 (Figures 5.8a, 5.9a, and 5.10a). The PBL TEMF scheme continued to register overestimates, whereas ACM2 was better in all metrics (Figures 5.8b, 5.9b, and 5.10b). The KainF, G3, and KFCuP schemes again showed better capability in representing rainfall, with KFCuP improving the average total period accumulations by more than 50% (Figures 5.8c, 5.9c, and 5.10c). The surface physical schemes show little variation among them with the exception of RUC, which also stands out in all metrics (Figures 5.8d, 5.9d, and 5.10d).

Figure 5.8 – Average hourly accumulated rainfall at the rain gauges and the rainfall generated by the model for the simulated event 3.

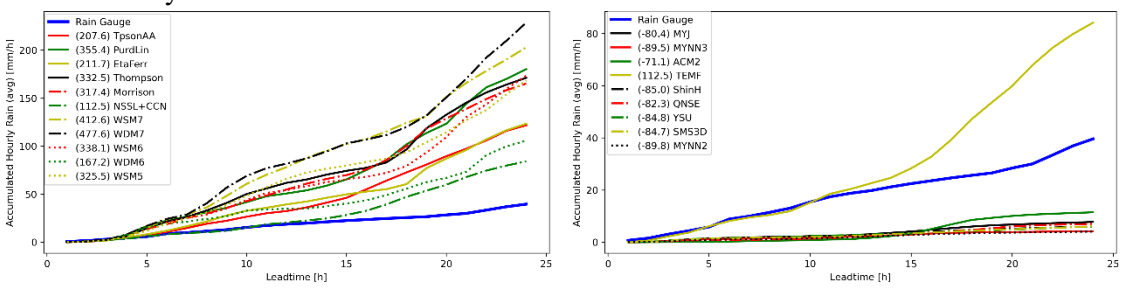

(a) (b)

(continue)

Figure 5.8 – Conclusion.

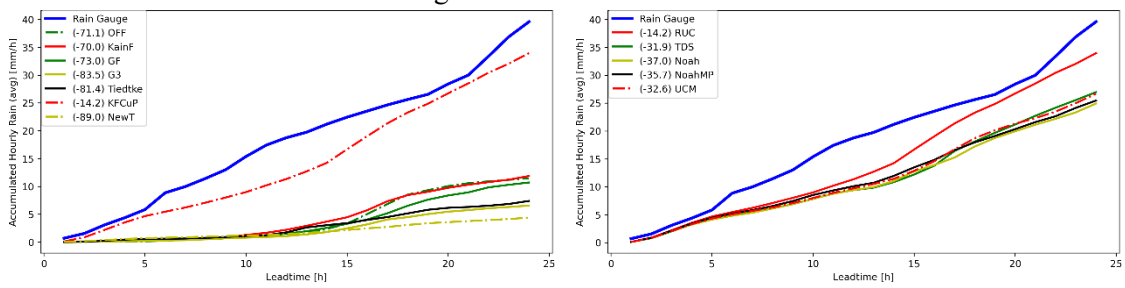

(c) (d)

Relative errors: (a) microphysics settings, (b) the planetary boundary layer, (c) cumulus, and (d) surface parameterizations. Comparison the average hourly accumulated rainfall at the rain gauges with the rainfall generated by the model according to the settings under analysis. Inside the legend are REs accumulated over 24 h for each configuration.

Figure 5.9 – Average hourly bias between the mean values calculated by the model and the mean values observed by rain gauges for event 3.

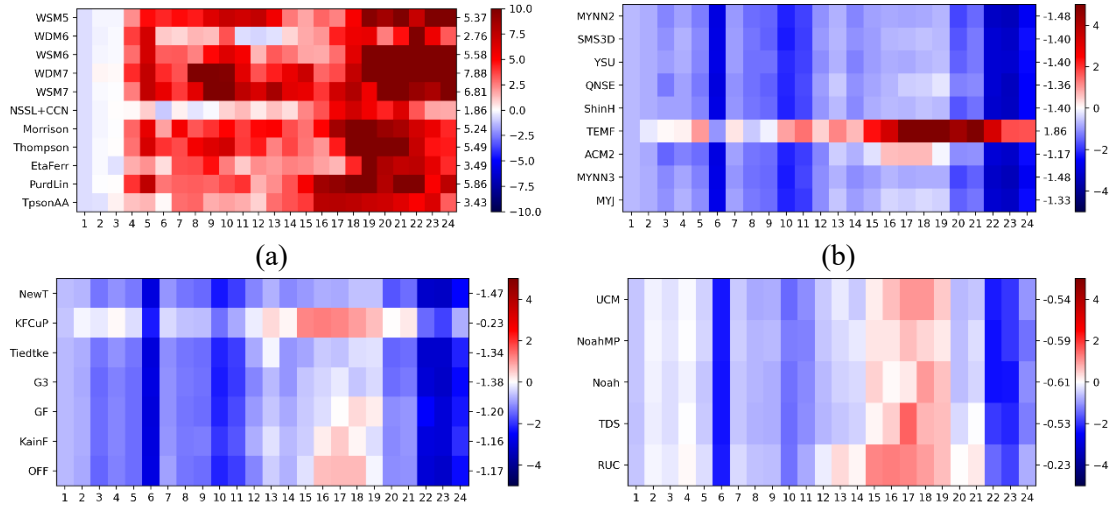

(a) (b)

(c) (d)

(a) microphysics settings, (b) the planetary boundary layer, (c) cumulus, and (d) surface parameterizations.The colors show the average hourly bias and on the secondary axis the average period bias.

Figure 5.10 – Taylor diagram for event 3 settings.

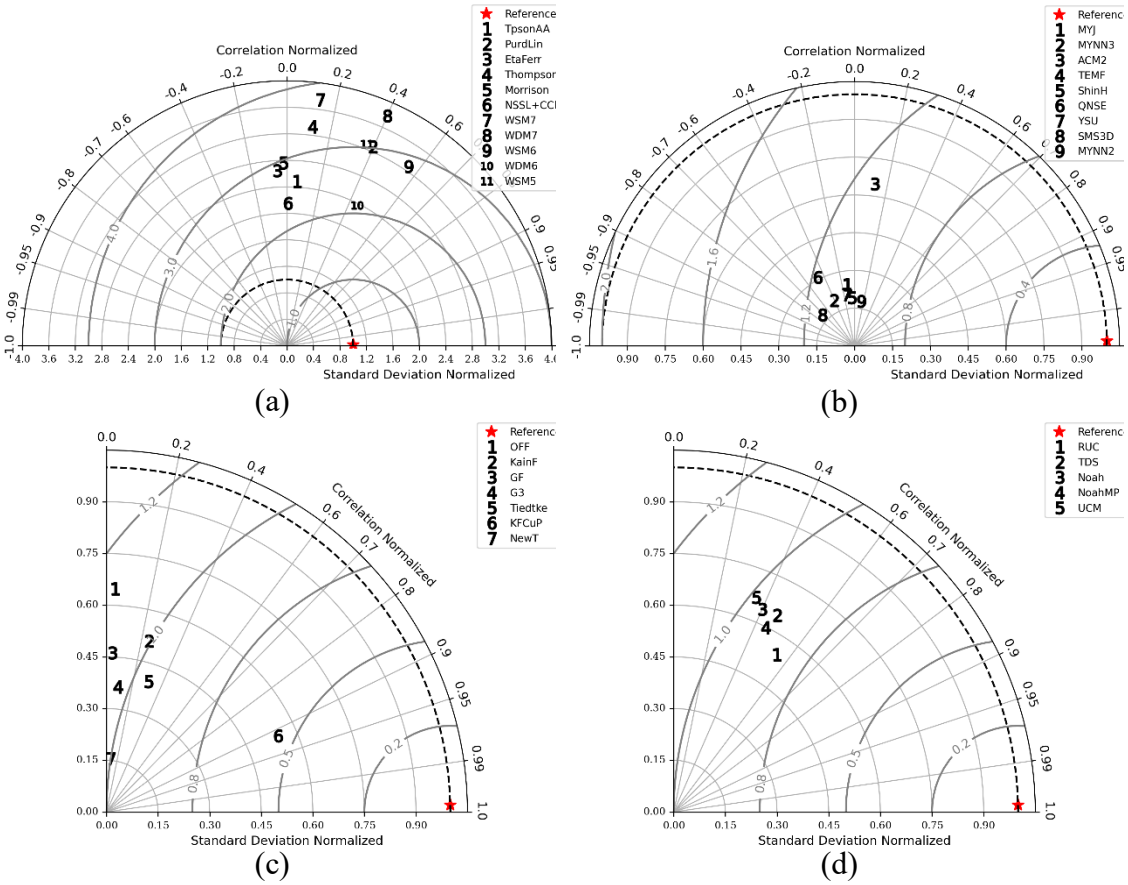

(a) microphysics settings, (b) the planetary boundary layer, (c) cumulus, and (d) surface parameterizations. The numbers correspond to the tested physical schemes.

The simulations for event 4 were performed between 20190528 12UTC and 20190529 12UTC and totaled 51 runs. For the microphysics parameterizations, the schemes that were best able to represent rainfall were TpsonAA, Thompson, and WSM5. Morrison's scheme overestimated the rainfall, and all others were barely able to generate rainfall (Figures 5.11a, 5.12a, and 5.13a). The TEMF boundary layer scheme also overestimated precipitation. The MYJ and YSU schemes showed close values, with YSU being considered slightly better (Figures 5.11b, 5.12b, and 5.13b). For this case, all the cumulus schemes, with the exception of Tiedtke, which failed to form rain, were able to better represent the precipitation (Figures 5.11c, 5.12c, and 5.13c). The G3 parameterization showed final average rainfall accumulations close to the values measured by the rain gauges. However, it exhibits a large bias at the beginning of the simulations, making its representation in the Taylor diagram inferior to KFCuP, which was therefore chosen as

the best. Again, the RUC surface scheme showed assertive displacement with respect to the others and was, therefore, chosen as the best (Figures 5.11d, 5.12d, and 5.13d).

Figure 5.11 – Average hourly accumulated rainfall at the rain gauges and the rainfall generated by the model for the simulated event 4.

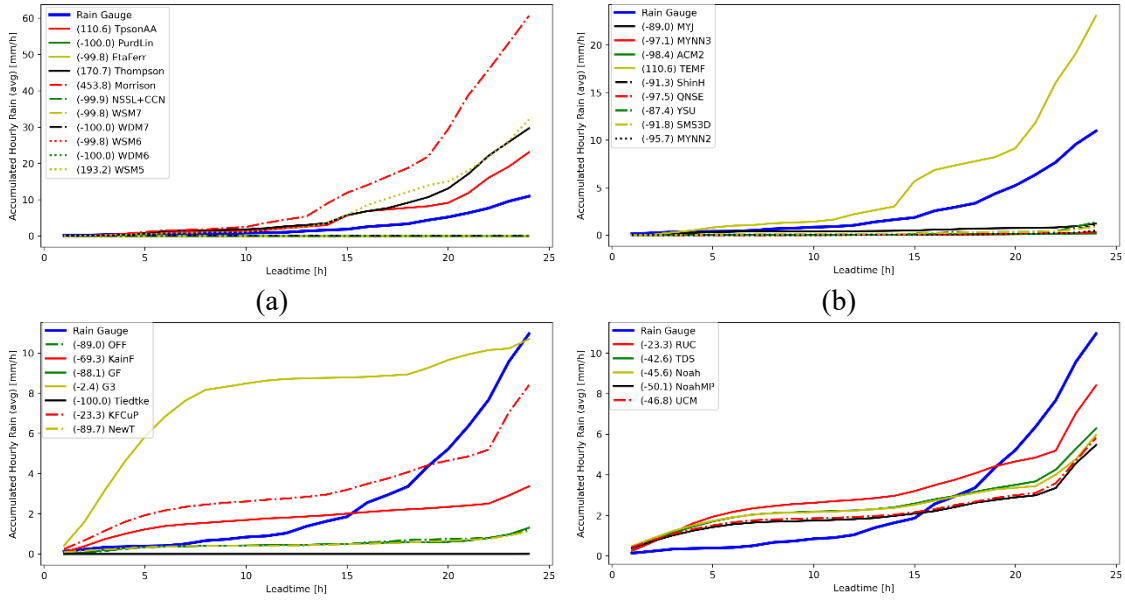

Relative errors: (a) microphysics settings, (b) the planetary boundary layer, (c) cumulus, and (d) surface parameterizations. Comparison the average hourly accumulated rainfall at the rain gauges with the rainfall generated by the model according to the settings under analysis. Inside the legend are REs accumulated over 24 h for each configuration.

Figure 5.12 – Average hourly bias between the mean values calculated by the model and the mean values observed by rain gauges for event 4.

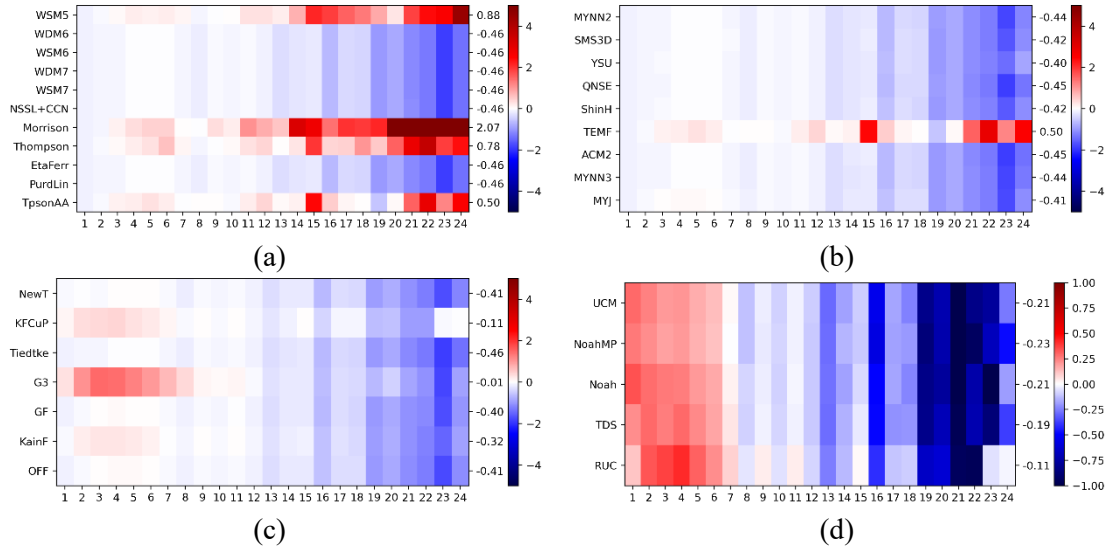

(a) microphysics settings, (b) the planetary boundary layer, (c) cumulus, and (d) surface parameterizations. The colors show the average hourly bias and on the secondary axis the average period bias.

Figure 5.13 – Taylor diagram for event 4 settings.

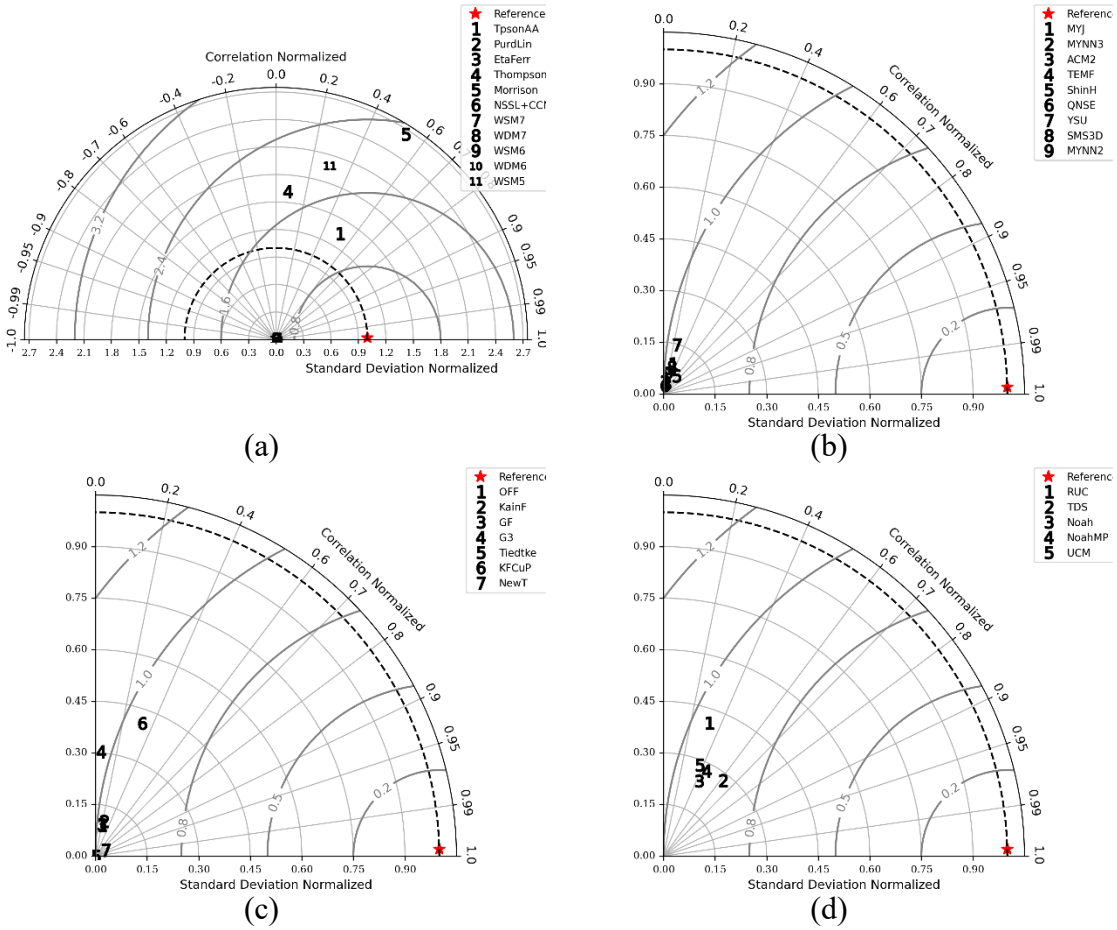

(a) microphysics settings, (b) the planetary boundary layer, (c) cumulus, and (d) surface parameterizations. The numbers correspond to the tested physical schemes.

Table 5.1 summarizes the best configurations and metrics obtained for each analyzed event and Table 5.2 shows the variation of RE among each set of physical schemes tested and the best RE achieved.

Table 5.1 – The best settings and their respective statistical metrics.

Event Date	MPH	PBL	CUM	SFC	*RE(%)*	*Bias*	*σ*		*R**	*RMS*	
							Data	*Model*		*value*	*norm*
20170528	Thompson	MYJ	KFCuP	RUC	*-49.2*	-1.38	5.455	1.230	0.221	5.699	0.975
20170720	NSSL+CCN	ACM2	KFCuP	RUC	*3.6*	0.08	3.386	2.445	0.860	3.842	0.528
20180422	NSSL+CCN	ACM2	KFCuP	RUC	*-14.2*	-0.23	3.695	2.015	0.546	3.936	0.838
20190529	TpsonAA	YSU	KFCuP	RUC	*-23.3*	-0.11	2.872	1.176	0.322	2.967	0.951

* Normalized values.

Table 5.2 – RE variation for each simulation set and per event (Δ%) and the best RE performed.

Schemes	Event 1		Event 2		Event 3		Event 4		AVG
	ΔRE	**Best**	**ΔRE**	**Best**	**ΔRE**	**Best**	**ΔRE**	**Best**	**ΔRE**
MPH	173.8	−147.3	−34.4	−65.6	365.1	112.5	553.8	−99.8	263.6
PBL [1]	7.9	−86.2	20.3	−46.9	18.7	−71.1	9.4	−89.0	13.9
PBL [2]	324.0	237.0	316.9	270.0	183.6	122.5	199.6	110.6	223.3
CUM [3]	−47.0	−49.2	−56.4	3.6	−67.2	−14.2	−97.6	−2.4	62.5
CUM [4]	−37.0	---	−50.5	---	−56.9	---	−86.6	---	−43.1
SFC	−6.4	−49.2	−8.2	−2.7	−22.8	−14.2	−26.8	−2.4	11.5

[1] PBL without TEMF. [2] PBL with TEMF. [3] Difference between the worst CUM and the best CUM. [4] Difference between the simulation without CUM and the best simulation with CUM.

For the microphysics schemes, for events 1, 2, and 3, TpsonAA and NSSL + CCN were always in the top three. The WDM7 scheme appeared among the three worst in all cases and failed to represent any rainfall in events 2 and 4. The WSM7 microphysics also appeared among the worst three in events 1, 3, and 4. These schemes add the hail hydrometeor to the microphysical and precipitation processes. According to Bae et al. (2019), these schemes tend to increase the accretion rate of ice particles due to the faster sedimentation of hail than graupel. In this way, the amount of hail is largely offset by a reduction in graupel, but it is the maximum at lower altitudes. Snow weakens the accretion of graupel at higher altitudes, which keeps it aloft, increasing its presence at medium levels. The reduction in the sum of graupel and hail in the melt layer leads to a decrease in the mixing ratio of the rain, which is compensated by falling hail. Therefore, this scheme tends to increase convective activity in regions of greater instability and decrease the intensity of precipitation in the stratiform region, thus configuring the role of hail in suppressing light precipitation and increasing heavy precipitation. This fact may have led to the poor performance of these schemes since this region is predominantly marked by shallow warm top storms (ARAÚJO PALHARINI; VILA, 2017).

TpsonAA microphysics incorporates the activation of aerosols as cloud condensation nuclei (CCN) and ice (IN) and, therefore, explicitly predicts the cloud water droplet number concentration, besides being designed for clouds where updrafts are present (THOMPSON; EIDHAMMER, 2014). NSSL + CCN microphysics predicts the mass

mixing ratio and the number of concentrations of all hydrometeor species, and the version used in this study also predicts the concentration of CCN (MANSELL; ZIEGLER; BRUNING, 2010; LI; ZHANG; XUE, 2017). It is remarkable that the best microphysics schemes verified in this study have explicit representations of aerosols and CCN. Atmospheric aerosol particles have a significant impact on the development of deep convective storms (SUN; ARIYA, 2006; HAZRA et al., 2017).

In a study on CCN concentration in northeastern Brazil, Almeida et al. (2014) stated that the concentration of coastal aerosols is almost double the concentrations of the inland aerosols and also influences the fraction of active particles, such as CCN, which has much higher concentrations when it originates over the sea. This fact also agrees with the region of highest precipitation in event 1 (inland Figure 3.4a), the only case where the best microphysics was neither TpsonAA nor NSSL + CCN and was generally not well represented. Oliveira et al. (2019) also analyzed aerosols in the NEB, identifying the predominant concentration of dust, marine aerosol, biomass burning, and particulate pollution, which can come from the ocean, the Amazon region, and even the coast of Africa. Figure 5.14 shows the trajectory where the air parcels came from for each simulated event and corroborates Oliveira's (2019) results. Overall, the lower and middle layer are majority influenced by southeast trade winds in the tropical South Atlantic Basin (UTIDA et al., 2019) but the high levels can be influenced by the outflow coming either from the central portion of the Atlantic (Figures 5.14a and d), the coast of Africa (Figure 5.14b), or the Amazon region (Figure 5.14c).

Figure 5.14 – Hysplit model backward trajectory direction.

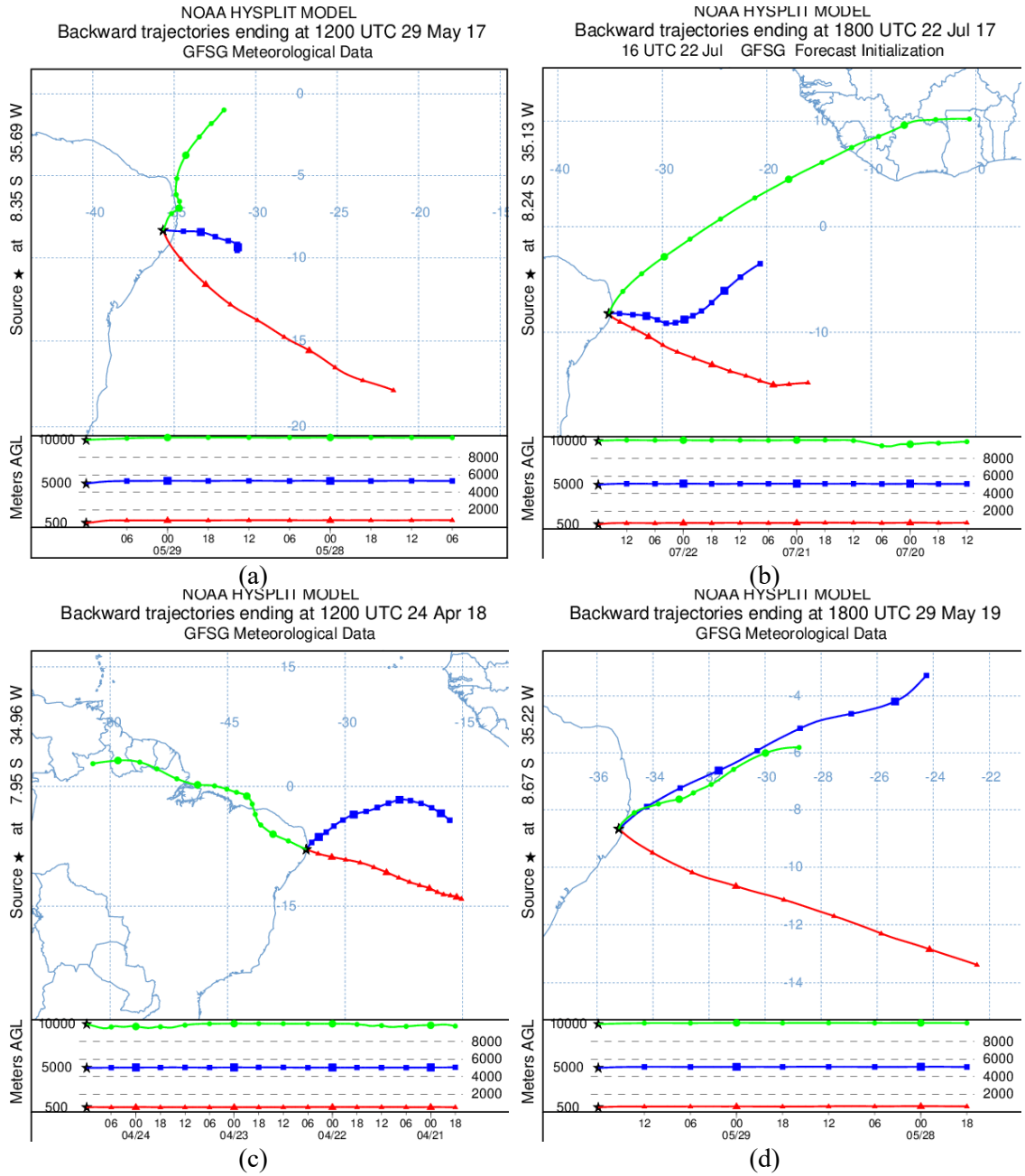

(a) event 1, (b) event 2, (c) event 3, and (d) event 4. Trajectories generated by the READY platform of the HYSPLIT model with GFS data. Available at https://www.ready.noaa.gov/HYSPLIT_traj.php.

For the planetary boundary layer schemes, MYJ was among the top three in three cases (being the best in event 1), ACM2 was the best in events 2 and 3, and TEMF was the worst in all other events. The parameters relevant for severe storm prediction controlled by PBL schemes act on buoyancy through modulations in potential temperature and

mixing ratio associated with stronger variability in the mixing layer depth (COHEN et al., 2015). A hypothesis for MYJ's better performance, a 1.5-order closure local scheme, in event 1, may be related to the production of a cooler and moister PBL (HU; NIELSEN-GAMMON; ZHANG, 2010) since the region analyzed for this case was the one positioned further inland and the simulations were between 12UTC on consecutive days, which completely covers the period of greatest radiative surface cooling. In the ACM2 scheme, a first-order closure hybrid scheme, non-local mixing, is represented by a matrix that defines the mass flows between any pair of model layers even if they are not adjacent (PLEIM, 2007). The YSU scheme, non-local first-order closure, considers the entrainment on top of the PBL explicitly (COHEN et al., 2015) and was considered the best scheme in work of Comin et al. (2021) for the same study region. Both schemes best represent shear and buoyancy in the study by Wang et al. (2016) and are generally characterized by a drying and warming daytime PBL (COHEN et al., 2015). These schemes helped in a better depiction of the rainfall in the events that occurred at the coastal zone interface (Figure 3.4b–d).

In the TEMF, a 1.5-order closure hybrid scheme, local mixing, is parameterized by a turbulent diffusivity, whereas the impact of non-local transport and mixing under convective conditions is parameterized using a mass flow method (ANGEVINE; JIANG; MAURITSEN, 2010). In all events, this scheme overestimated the rainfall (Figures 5.2b, 5.5b, 5.8b, and 5.11b). Some works have reported a larger vertical gradient of the water vapor mixing ratio and higher moisture content within the low cloud layer, which results in a pronounced moisture flux (ANGEVINE; JIANG; MAURITSEN, 2010; WANG; SHEN; HUANG, 2016), which can also be verified in this study in all events. Wang et al. (2016) further stated that no single scheme performs optimally in all aspects and that PBL schemes may depend on the atmospheric scenarios in which they are inserted. However, all these hypotheses can be more rigorously investigated by analyzing turbulent flows, diffusivity, and meteorological variables (such as potential temperature, wind, and water vapor mixing ratio) within the boundary layer, which is not within the scope of this work.

In all events, the rain representation was better with the cumulus parameterization activated. This study was within the so-called gray zone for cumulus clouds (cumulus schemes), and several recent studies have corroborated the activation of cumulus

parameterizations at resolutions between 2 to 3 km (KOTRONI; LAGOUVARDOS, 2004; MU et al., 2019; LIU; CHENG; HU, 2021). One of the main arguments for this activation is that these resolutions are still insufficient to represent the full spectrum of the convective scale (BRYAN; WYNGAARD; FRITSCH, 2003). The KFCuP, G3, and KainF convection schemes were better than the simulations with cumulus off in all events. The innovation between KFCuP and KainF is mainly the implementation of a new trigger function related to the temperature and moisture distribution in the convective boundary layer via a probability density function (BERG et al., 2013). To solve the problems of convective parameterizations, G3 uses ensemble and data assimilation techniques (GRELL; DÉVÉNYI, 2002). GF does a smoothing for the resolved cloud-scale transition, thus being a "scale-aware" scheme, in addition to interacting with aerosols through CCN autoconversion from cloud water to rain (GRELL; FREITAS, 2013).

In all cases studied, the land surface models showed the least variation between simulations of the same event (Table 5.2). The RUC scheme was among the top two in all cases, and TDS was among the top two in events 3 and 4. The TDS scheme has five soil layers, and the energy budget includes radiation, sensible, and latent heat flux, whereas in this study, RUC was used with nine soil layers, taking into account water phase changes, vegetation effects, prognostic variables, and a host of features that make it much more complex (BENJAMIN et al., 2004). The TDS scheme can be considered the simplest one currently available and performs better than the others (it was the second best in events 3 and 4). UCM was tested in all events, but a coherent analysis of the effects of this scheme should be restricted to, for example, the metropolitan region of Recife (within the yellow boxes in Figure 3.4c), where it is expected that this scheme can develop its characteristics and contribute to the results. Still, UCM was the second-best surface scheme with respect to the 24-h precipitation deviation in events 1 and 2. Table 5.2 shows the variation in the RE concerning the average total cumulative over 24 h for each simulation set tested and the observed improvement in this same index after the best physical scheme was chosen. Disregarding the PBL TEMF scheme, the largest variations are observed when using the microphysics and cumulus schemes. When TEMF is considered, the PBL variations are as large as the microphysics ones.

6 DIAGNOSTIC ANALYSIS

To describe the dynamic and thermodynamic factors that acted during the development of the storms, the atmospheric instability and the favorability of the middle and upper layers to the action of the systems were analyzed and the moisture supply in the low levels was verified with data from new simulations performed with the best configuration obtained from the previous analyses. These new simulations covered the total rainfall period for each event and started 6 hours before the onset of rainfall recorded at the rain gauges to cover the model spinup. For event 1 the simulations were from May 27, 2017, at 00 hours to May 29, at 12 hours totaling 60 hours of simulation, for event 2 the simulation was from July 19, 2017, at 06 hours to July 22, at 18 hours totaling 78 hours, for event 3 the simulation was from April 20, 2018, at 12 hours to April 24 at 12 hours totaling 96 hours, and for event 4 the simulation was from May 27, 2019, at 12 hours to May 29, at 6 hours totaling 54 hours of simulation. These analyses were performed for the regions within the yellow boxes (Figure 3.4) for each of the events studied.

For event 1, the analyses of the weather variables within the yellow box occurred in a region with a lower pluviometric density (Figure 6.1a). The model was able to represent an intense MFC just after the first 3 h of simulation. The MFC reached the 700 mb level, with near-surface values exceeding 30×10^{-3} g·kg^{-1}s^{-1} and was well-related to cyclonic vorticity advection in the low and middle layers (Figure 6.1b). The CAPE values at the beginning of the storm were intense, greater than 2500 J·kg^{-1}, and after the first 12 h began to decrease in a reverse motion to the shear in the middle layer, and the CINE values began to increase (Figure 6.1c). The low-level outflow was predominantly from the southeast with a reversal and weakening from the 700 hPa level (Figure 6.1d) a strong wind outflow at the 400 hPa level at the beginning of the event (Figure 6.1d and 6.1e) and wind divergence in the low layer during the whole period (Figure 6.1e).

Figure 6.1 – Analysis of the dynamic and thermodynamic variables inside the yellow box (Figure 3.4) for event 1.

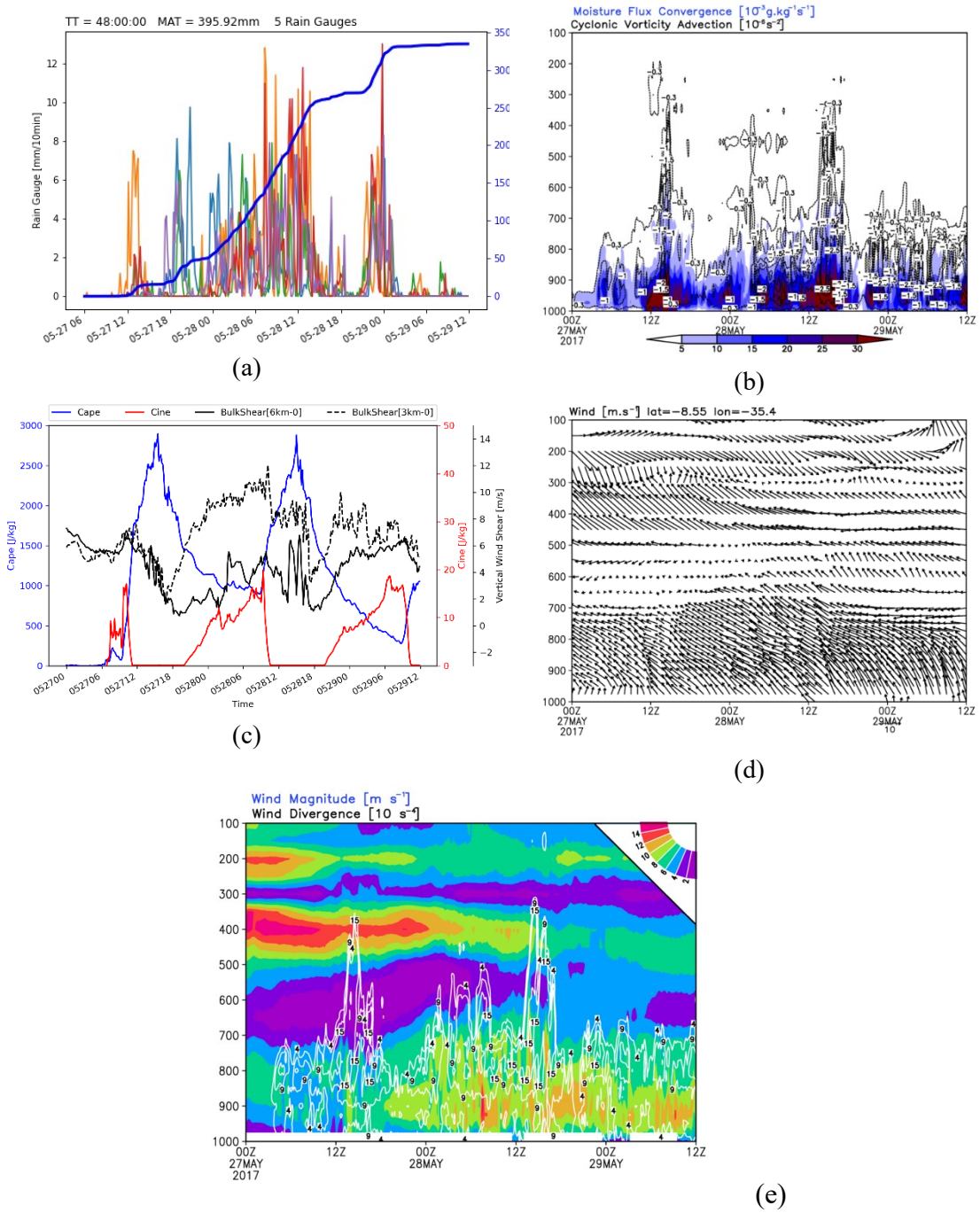

(a) each rain gauge represents a different color (mm/10 min) and average accumulated precipitation in blue at Total Time (TT) for event; MAT is for maximum accumulated total; (b) maximum MFC (10^{-3} g·kg^{-1}s^{-1}) and minimum ADV_{ζ} (10^{-6} s^{-2}); (c) maximum values of CAPE and CIN (J·kg^{-1}) and maximum values of bulk shear (m·s^{-1}) in their respective layers (outer axis); (d) vertical variation in the mean wind vector (m·s^{-1}); and (e) wind divergence (10^{-4} s^{-1}) and magnitude (m s^{-1}).

For event 2, precipitation showed an increase in intensity around at 12UTC (Figure 6.2a), which was directly related to the increase MFC (Figure 6.2b). Simultaneously, there was an abrupt drop in the values of CINE and the vertical wind shear in both the deep layer and the bottom layer, accompanied by the maximum peak of the CAPE (Figure 6.2c). At that same instant, between the 600 hPa and 500 hPa levels, the wind weakened and the shear of its direction was remarkable (Figure 6.2d) with the intensification of high-level outflow and favoring of the vertical extent of wind divergence (Figure 6.2e) always accompanied by intensification of wind convergence in the levels immediately below. In this event, a rain gauge at a certain moment registered a shower of rainfall exceeding 20 mm/10 min. The MFC reached the 700 hPa level and near-ground values on the order of 30×10^{-3} g·kg^{-1}s^{-1}, which was favored by advection of cyclonic vorticity, which weakened with height and was observed until the 300 hPa level aligned with the maximum MFC values. The CAPE peaked (~1500 J·kg^{-1}) just before the increase in precipitation intensity and CINE (~50 J·kg^{-1}) about 3 h before the CAPE. Wind shear was the highest in the lower layer (3 km) and showed values of 12 m·s^{-1}.

Figure 6.2 – Analysis of the dynamic and thermodynamic variables inside the yellow box for event 2.

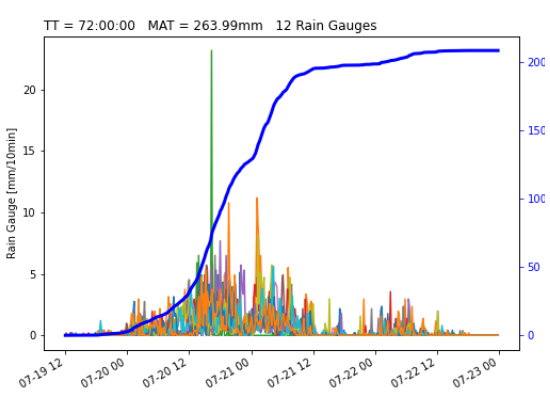

(a)

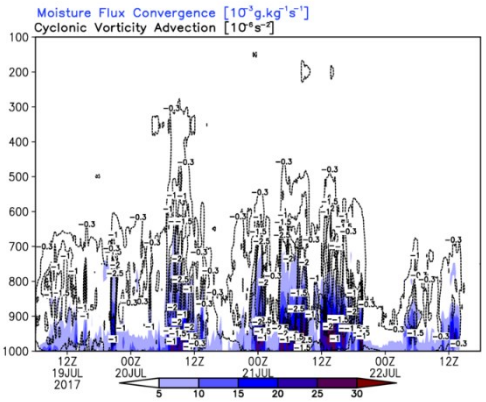

(b)

(continue)

Figure 6.2 – Conclusion.

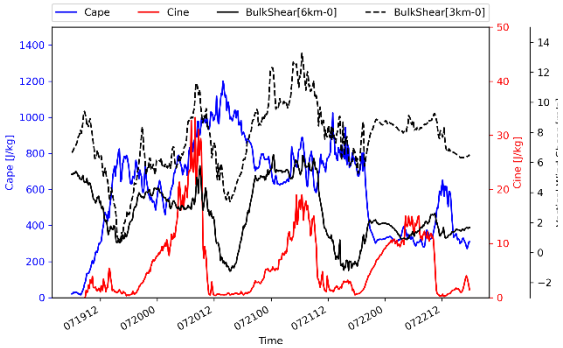

(c)

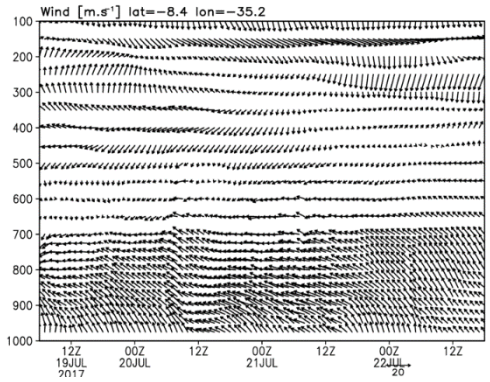

(d)

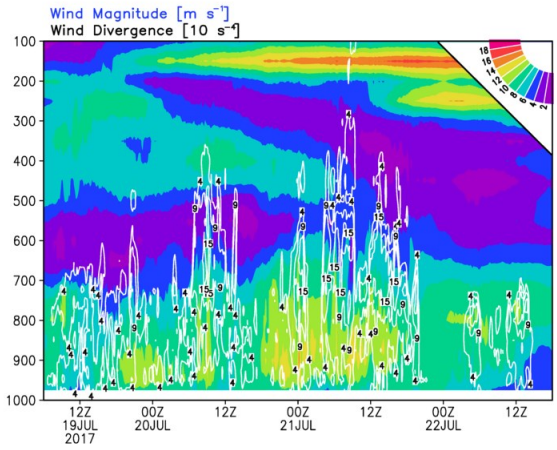

(e)

As in figure 6.1 but for event 2.

For event 3, the analyses within the yellow box covered the metropolitan region of the city of Recife which has the largest concentration of rain gauges (Figure 6.3a). It is possible to observe the good correspondence between MFC and the precipitation peaks (Figure 6.3a,b). A cyclonic vorticity advection core was verified at 15 UTC between the 700 hPa and 800 hPa levels and another one at high levels at the end of the simulation and coinciding with new rainfall occurrences (Figure 6.3b). The inhibition energy showed four maximum peak intensities, always following the wind shear variations in both layers and a variation almost always opposite to CAPE (Figure 6.3c). Again, the maximum CAPE values were near 2500 $J \cdot kg^{-1}$ and the maximum wind shear was around 10 $m \cdot s^{-1}$. The outflow in the low levels was predominantly from the southeast with weakening in the mid layer and reversal in the high levels (Figure 6.3d) and presence of intense outflow at high levels (Figure 6.3e).

Figure 6.3 – Analysis of the dynamic and thermodynamic variables inside the yellow box for event 3.

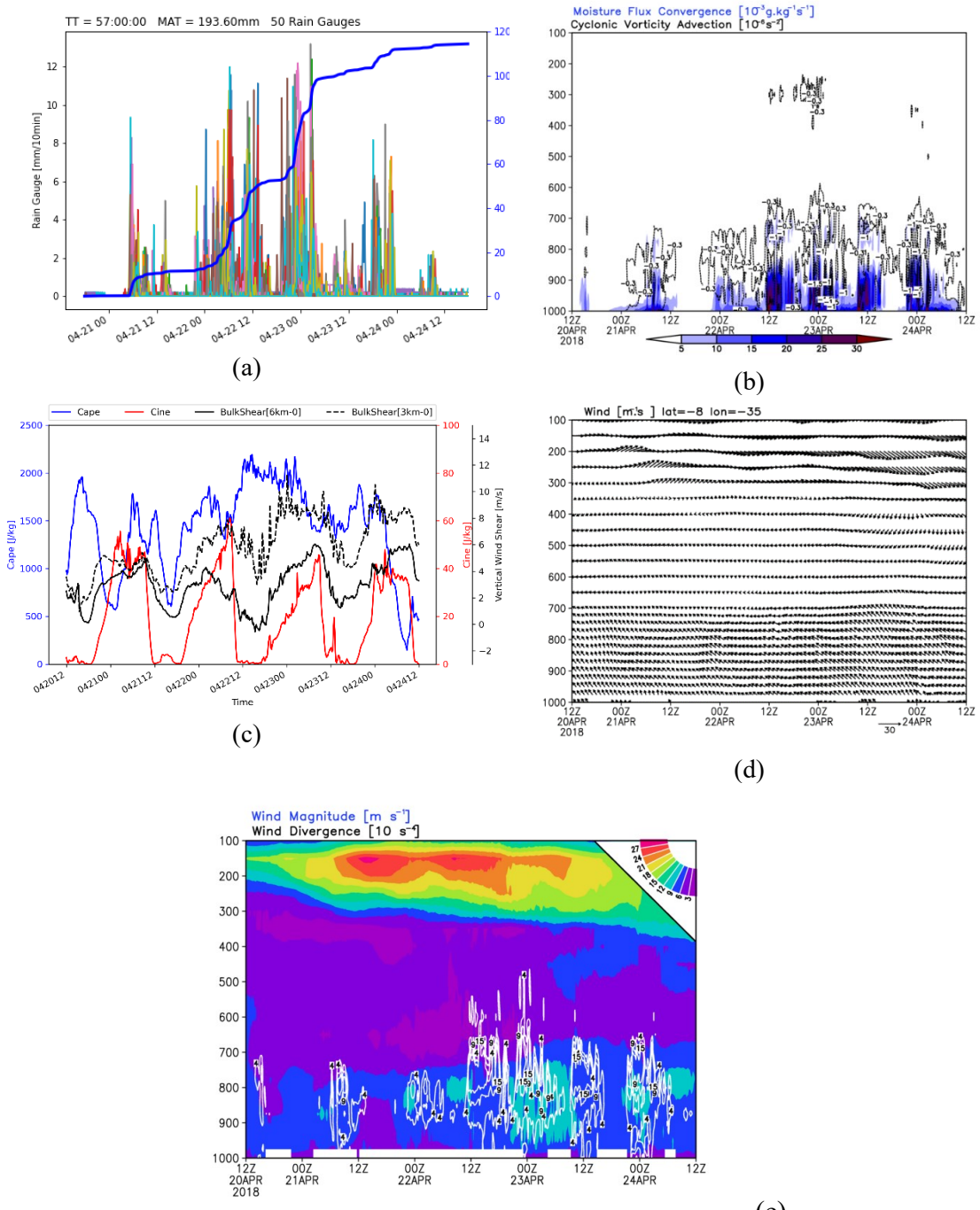

As in figure 6.1 but for event 3.

Precipitation in event 4, a less spatially comprehensive or locally characteristic event, showed the highest rain rates at the end of the observation period (Figure 6.4a). Despite the smaller spatial coverage, the intensity of the rainfall can be seen, with precipitation rates exceeding 15 mm/10 min. The MFC was confined to a lower layer than in the

previous cases, at around 800 hPa, and the moisture supply was available at least 6 h before the onset of precipitation. No support from the medium and upper levels was observed for this event (Figure 6.4b). This was the only case where the shear in the deep layer was predominantly higher than the shear in the middle layer (Figure 6.4c). Unlike the other cases, the higher precipitation rates were associated with keeping the CAPE and shear values with slight variation. (Figure 6.4c). The CAPE and shear values were also lower than in the previous cases (approximately 2000 $J \cdot kg^{-1}$ and 8 $m \cdot s^{-1}$, respectively). This was the only case where the outflow in the middle layer did not weaken and the wind at low levels was predominantly from the east (Figure 6.4d) with two overlapping maximum wind speed nuclei (Figure 6.4e) and coinciding with the instant of intense MFC at low levels.

Figure 6.4 – Analysis of the dynamic and thermodynamic variables inside the yellow box for event 4.

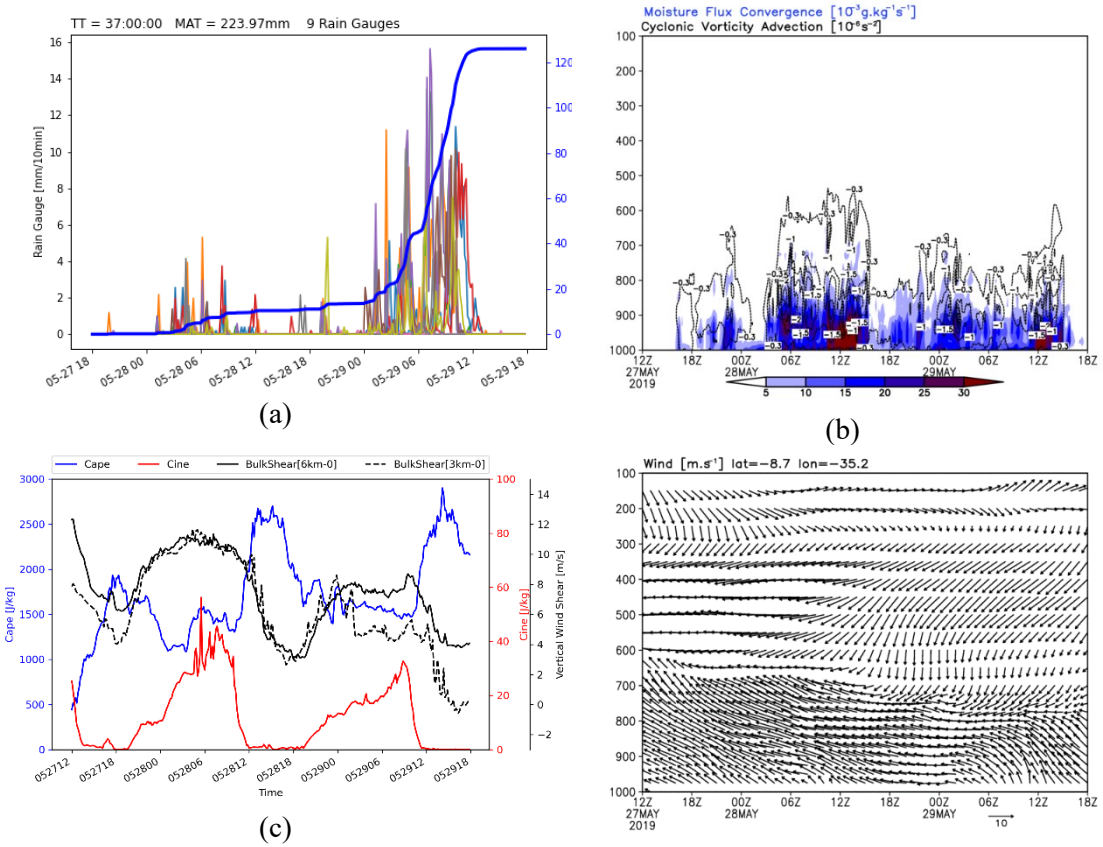

(a) (b) (c) (d)

(continue)

Figure 6.4 – Conclusion.

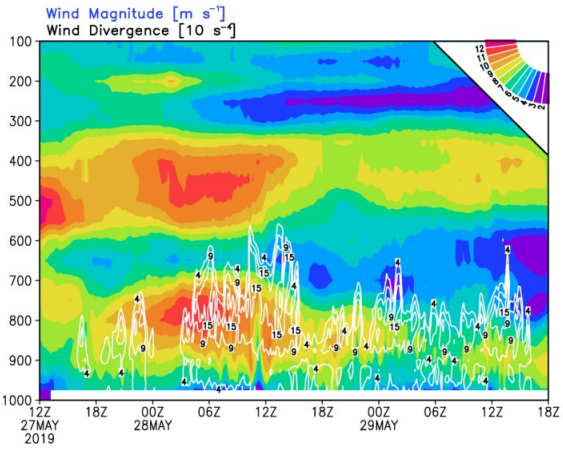

As in figure 6.1 but for event 4.

In all simulated cases, the prevailing wind at the surface and in the low layer was from the southeast and/or the east, in agreement with the influence of the trade winds in the region. In all simulated cases, the moisture flux convergence in the low layer reached the 800 hPa level. In general, MFC was well-related to precipitation, with maximum values observed before and during maximum precipitation, reaching values higher than 30×10^{-3} $g \cdot kg^{-1}s^{-1}$ in all cases, values comparable to the occurrence of the most robust updrafts measured in nature (BANACOS; SCHULTZ, 2005). The cyclonic vorticity advection at medium and high levels supported the convergence at low levels in events 1, 2, and 3. Only in event 4, considered an isolated storm case, the support of the high and middle layers was not observed. The lowest maximum CAPE value was observed in event 2 (around 1400 $J \cdot kg^{-1}$) and the highest in events 1 and 3 (about 2500 $J \cdot kg^{-1}$). The maximum values of the CINE were between 30 and 60 $J \cdot kg^{-1}$ in events 2 through 4. In event 1, it presented the lowest values, increasing throughout the simulation. As expected, the values of the CAPE and CINE show antagonistic movements, with a sharp drop in the values of CINE from the maintenance of the CAPE and/or after reaching certain values (between 1200 and 1500 $J \cdot kg^{-1}$).

The vertical wind shear in the deep layer was higher than the shear in the middle layer only in event 4. In the other events, the shear in the middle layer was higher, with maximum values between 10 and 12 $m \cdot s^{-1}$. An inverse relationship was also observed between the wind shear in both layers and the CAPE values, that is, after wind shear

intensifies, the CAPE values tend to decrease. However, the higher precipitation rates were associated with increased wind shear, most noticeable in the deep layer for event 4 and the middle layer for the other events. Vertical wind shear tends to promote thunderstorm organisation, although excessive wind shear can be detrimental to convective initiation by increasing entrainment of environmental air into the storm. In general, the wind shear starts at values around 6 $m \cdot s^{-1}$, presents a drop after the first precipitations, and gradually increases reaching maximum values around 10 $m \cdot s^{-1}$, contributing to maintaining the storm's lifetime.

7 CONCLUSIONS

The present work analyzed 124 incident records of natural disaster alerts for the eastern part of the state of Pernambuco/Brazil, which were grouped into 24 severe weather events, and performed numerical simulation with the WRF model for 4 of these cases. The first practical results of this work can be seen in Appendixes B and C. As expected, a positive relationship was observed between the occurrence of the events and the rainy season in the region and a preference for the occurrence of alerts during nighttime hours. The spatial arrangement of the municipalities warned is concentrated on the coastal strip, which may be associated with the greater rainfall regime and with the greater susceptibility to the occurrence of natural disasters due to the characteristics of social development in this region.

Half of the severe rainfall events were associated with synoptic scale systems and the other half with a smaller scale surface high pressure responsible for blocking the advance of the southeast trade winds and favoring convergence at the surface. Among the synoptic systems, the ITCZ showed more significant action, while the high pressure at the surface, which can be closed or in the form of a ridge, can act alone or be associated with some other mechanism in general at medium and high levels.

The precipitation cells in 50% of cases were composed of multiple small-sized cells entering the continent mainly from the east and southeast. The highest reflectivity observed in a storm core was 60dBZ and almost 90% of cases showed a vertical extent greater than 5000 m.

The rainfall was also classified as short and long duration, with the longest lasting event being over 200 hours and the shortest lasting event being only 14 hours. The rain gauge that registered the highest accumulation was 366 mm in rainfall that lasted 48 hours without interruption but with weak intensity. The heaviest rainfall rate accumulated more than 140 mm in just 14 h. The most common events are long duration and capable of large rainfall totals.

Four severe rainfall events that triggered natural disasters were chosen for detailed analysis with the WRF model. The event of 20170528 was associated with an MCS, the cases of 20170720 and 20190529 were associated with isolated storms, and the event of 20180422 with runoff coming from the ITCZ. All cases showed substantial wind

divergence averaged between the 800 and 600 hPa levels and the presence of moisture flux convergence from the ocean. In all the cases analyzed, high pressure was observed on the surface over the continent, sometimes with closed isobars and sometimes in the form of a ridge, which in half of the cases directly contributed to the intensification of convergence near the coast to the east of its position, and the favoring to storm formation.

For the analysis of the physical configurations of the model, the microphysics schemes with aerosol and/or CCN treatment stood out. The microphysics incorporating hail as a hydrometeor category performed the furthest from the observations. The TEMF boundary layer scheme offered parameters for an overestimation of rainfall in all cases. None of the characteristics that allow categorizing the planetary boundary layer schemes, such as order of closure or local or non-local scheme, stood out widely, but the parameterizations that showed the best results were ACM2, MYJ, and YSU.

The numerical simulations were performed at 2.5km horizontal resolution, and almost all simulations with the cumulus parameterization tuned were closer to the observed precipitation. The KFCuP scheme was better in all simulations and was responsible for more than a 50% improvement in the representation of rainfall in events 2 and 3. The surface schemes showed the slightest variation from each other, with the RUC scheme also being the best in all simulations. It has been shown that air parcels from different locations, not only from the adjacent ocean, charged with the thermodynamical properties of their regions of origin, such as the Amazon region and the west coast of Africa, can act on the east coast of the NEB.

The analyses of the dynamic and thermodynamic variables in the intersection regions between the heaviest precipitation and the warned municipalities show an intense moisture convergence flow in the low layer that easily reaches the 700 hPa level and that presented values that exceeded 3.0×10^{-2} g·kg^{-1}s^{-1}. The maximum CINE values were around 30 J·kg^{-1} in the first and second cases and 50 J·kg^{-1} in the third and fourth cases indicating the absence of a more robust lifting mechanism where diurnal heating or local topographic features would be sufficient for triggering convection. However, the lifting mechanisms indispensable for the development of storms has not been completely identified.

The CAPE values almost reached 3000 $J \cdot kg^{-1}$, and an antagonistic relationship was observed with wind shear variations, especially in the middle layer, which showed the highest values. The highest shear values did not reach 15 $m \cdot s^{-1}$, and the variations throughout the storms were, on average, between 6 $m \cdot s^{-1}$ and 8 $m \cdot s^{-1}$. Also of note is the presence of the substantial wind divergence between the low and mid-layer well related to the storm formation position.

Regarding the specific objectives that guided this work:

1) It has been demonstrated that mainly Intertropical Convergence Zone, high and medium level outflow, local high pressure at the surface, and secondary participation of Upper Tropospheric Cyclonic Vortices and Easterly Wave Disturbances play a role in the region;

2) An important contribution of the microphysics schemes that take aerosols and CCN into account was found. The convective scheme KFCuP was much better than the others and RUC for the surface. The ACM2, MYJ, and YSU schemes stood out for planetary boundary layer;

3) For the meteorological variables, it was observed an important role of mid to low level wind divergence with strong convergence in the levels immediately below, intense CAPE values, and strong moisture flux convergence, besides wind shear values in the average below 10 $m \cdot s^{-1}$.

7.1 Suggestions for further work

This work was inserted in the context of extreme weather and climate events and sought to contribute to the identification of synoptic and mesoscale systems through satellite, model, radar, and rainfall data, and to propose a better configuration for numerical simulations as well as to identify and describe the main ingredients responsible for severe rainfall events. As a suggestion for future work, we suggest expanding this analysis to the other priority regions for natural disasters in Brazil, for example, the metropolitan regions of São Paulo, Rio de Janeiro, Manaus, and Salvador, and the mountainous regions of the states Rio de Janeiro, Santa Catarina, and Espírito Santo, all of which are known to be sensitive to severe rainfall events.

A vital aspect identified in this study was the ability to contribute to the formation of severe thunderstorms of the high-pressure surface system when positioned near the coast of the states of Alagoas and Pernambuco. This system and all its effects need to be better studied. Also, for the eastern coastal region of the NEB, the influence of sea surface temperature on the increase or suppression of moisture fluxes from the ocean has not been considered in this study. Studies that consider this effect on local storm formation need to be considered. One suggestion to better understand the lifting mechanisms, especially of entirely mesoscale storms, is to increase the region of the simulations in the ocean direction because one of the observed features not explored in this study was the presence of several wind convergence and water vapor mixing ratio cores coming from outside the grid.

REFERENCES

AHRENS, C. D.; HENSON, R. **Meteorology today an introduction to weather, climate, and the environment**. 12.ed. Boston: Cengage, 2019. 678 p. ISBN(13: 978-1-337-61666-9).

AHRENS, C. D.; SAMSON, P. J. Weather forecasting. In: LEARNING, C. (Ed.). **Extreme weather and climate**. Belmont: Brooks/Cole, 2011. p. 398–427.

ALEKSANDROVA, M.; BALASKO, S.; KALTENBORN, M.; MALERBA, D.; MUCKE, P.; NEUSCHÄFER, O.; RADTKE, K.; PRÜTZ, R.; STRUPAT, C.; WELLER, D.; WIEBE, N. **WorldRiskReport 2021: focus: social protection**. Berlin: Bündnis Entwicklung Hilft, 2021. 74 p. ISBN(978-3-946785-12-5).

ALMEIDA, G. P.; BORRMANN, S.; LEAL JUNIOR, J. B. V. Cloud condensation nuclei (Ccn) concentration in the brazilian northeast semi-arid region: the influence of local circulation. **Meteorology and Atmospheric Physics**, v. 125, n. 3–4, p. 159–176, 2014.

ALVALÁ, R. C. S.; ASSIS DIAS, M. C. DE; SAITO, S. M.; STENNER, C.; FRANCO, C.; AMADEU, P.; RIBEIRO, J.; SOUZA DE MORAES SANTANA, R. A.; NOBRE, C. A. Mapping characteristics of at-risk population to disasters in the context of Brazilian early warning system. **International Journal of Disaster Risk Reduction**, v. 41, n. September, p. 101326, 1 dez. 2019.

ALVARES, C. A.; STAPE, J. L.; SENTELHAS, P. C.; DE MORAES GONÇALVES, J. L.; SPAROVEK, G. Köppen's climate classification map for Brazil. **Meteorologische Zeitschrift**, v. 22, n. 6, p. 711–728, 1 dez. 2013.

ANGEVINE, W. M.; JIANG, H.; MAURITSEN, T. Performance of an Eddy diffusivity–mass flux scheme for shallow cumulus boundary layers. **Monthly Weather Review**, v. 138, n. 7, p. 2895–2912, 2010.

ARAKAWA, A. The cumulus parameterization problem: past, present, and future. **Journal of Climate**, v. 17, n. 13, p. 2493–2525, 2004.

ARAKAWA, A.; SCHUBERT, W. H. Interaction of a cumulus cloud ensemble with the large-scale environment, part I. **Journal of the Atmospheric Sciences**, p. 674–701, 1974.

ARAÚJO PALHARINI, R. S.; VILA, D. A. Climatological behavior of precipitating clouds in the northeast region of Brazil. **Advances in Meteorology**, v. 2017, 2017.

ASSIS DIAS, M. C.; SAITO, S. M.; ALVALÁ, R. C. S.; SELUCHI, M. E.; BERNARDES, T.; CAMARINHA, P. I. M.; STENNER, C.; NOBRE, C. A. Vulnerability index related to populations at-risk for landslides in the Brazilian Early Warning System (BEWS). **International Journal of Disaster Risk Reduction**, v. 49, e 101742, 2020.

ASSIS DIAS, M. C.; SAITO, S. M.; ALVALÁ, R. C. S.; STENNER, C.; PINHO, G.; NOBRE, C. A.; FONSECA, M. R. S.; SANTOS, C.; AMADEU, P.; SILVA, D.; LIMA, C. O.; RIBEIRO, J.; NASCIMENTO, F.; CORRÊA, C. O. Estimation of exposed population to landslides and floods risk areas in Brazil, on an intra-urban scale. **International Journal of Disaster Risk Reduction**, v. 31, p. 449–459, 2018.

AVELAR, A. S.; NETTO, A. L. C.; LACERDA, W. A.; BECKER, L. B.; MENDONÇA, M. B. Mechanisms of the recent catastrophic landslides in the mountainous range of Rio de Janeiro, Brazil. **Landslide Science and Practice: Global Environmental Change**, v. 4, p. 265–270, 2013.

ÁVILA, A.; JUSTINO, F.; WILSON, A.; BROMWICH, D.; AMORIM, M. Recent precipitation trends, flash floods and landslides in southern Brazil. **Environmental Research Letters**, v. 11, n. 11, 2016.

BAE, S. Y.; HONG, S. Y.; TAO, W. K. Development of a single-moment cloud microphysics scheme with prognostic hail for the Weather Research and Forecasting (WRF) Model. **Asia-Pacific Journal of Atmospheric Sciences**, v. 55, n. 2, p. 233–245, 2019.

BALDWIN, M. E.; KAIN, J. S.; KAY, M. P. Properties of the convection scheme in NCEP's Eta Model that affect forecast sounding interpretation. **Weather and Forecasting**, v. 17, n. 5, p. 1063–1079, 2002.

BALDWIN, M. E.; KAIN, J. S.; LAKSHMIVARAHAN, S. Development of an automated classification procedure for rainfall systems. **Monthly Weather Review**, v. 133, n. 4, p. 844–862, 2005.

BANACOS, P. C.; SCHULTZ, D. M. The use of moisture flux convergence in forecasting convective initiation: historical and operational perspectives. **Weather and Forecasting**, v. 20, n. 3, p. 351–366, 2005.

BENJAMIN, S. G.; GRELL, G. A.; BROWN, J. M.; SMIRNOVA, T. G.; BLECK, R. Mesoscale weather prediction with the RUC hybrid isentropic–terrain-following coordinate model. **Monthly Weather Review**, v. 132, n. 2, p. 473–494, 2004.

BERG, L. K.; GUSTAFSON, W. I.; KASSIANOV, E. I.; DENG, L. Evaluation of a modified scheme for shallow convection: implementation of CuP and case studies. **Monthly Weather Review**, v. 141, n. 1, p. 134–147, 2013.

BETTS, A. K.; MILLER, M. J. A new convective adjustment scheme. Part II: single column tests using GATE wave, BOMEX, ATEX and arctic air-mass data sets. **Quarterly Journal of the Royal Meteorological Society**, v. 112, n. 473, p. 693–709, 1986.

BHATE, J.; KESARKAR, A. P.; KARIPOT, A.; BALA SUBRAHAMANYAM, D.; RAJASEKHAR, M.; SATHIYAMOORTHY, V.; KISHTAWAL, C. M. A sea breeze induced thunderstorm over an inland station over Indian South Peninsula: a case study. **Journal of Atmospheric and Solar-Terrestrial Physics**, v. 148, p. 96–111, 2016.

BROOKS, H. E.; III, C. A. D.; WILHELMSON, R. B. The role of midtropospheric winds in the evolution and maintenance of low-level mesocyclones. **Monthly Weather Review**, v. 122, n. 1, p. 126–136, 1994.

BRYAN, G. H.; WYNGAARD, J. C.; FRITSCH, J. M. Resolution requirements for the simulation of deep moist convection. **Monthly Weather Review**, v. 131, n. 10, p. 2394–2416, 2003.

CAVALCANTI, I. F. A; KOUSKY, V. E. Climatology of South American cold fronts. In: INTERNATIONAL CONFERENCE ON SOUTHERN HEMISPHERE METEOROLOGY AND OCEANOGRAPHY, 7., 2003. **Proceedings…** 2003. p. 4–5.

CENTRO NACIONAL DE GERENCIAMENTO DE RISCOS E DESASTRES (CENAD). **Anuário brasileiro de desastres naturais 2011**. Brasília. 2012. Available from: <http://www.integracao.gov.br/c/document_library/get_file?uuid=e3cab906-c3fb-49fa-945d-649626acf790&groupId=185960>.

CENTRO NACIONAL DE MONITORAMENTO E ALERTAS DE DESASTRES NATURAIS (CEMADEN). **Anuário da sala de situação do Cemaden 2017**. São José dos Campos. 2019. Available from: <http://www2.cemaden.gov.br/wp-content/uploads/2020/06/Anuario_Sala_Situação_2017.pdf>.

CENTRO UNIVERSITÁRIO DE ESTUDOS; E PESQUISAS SOBRE DESASTRES (CEPED). **Atlas brasileiro de desastres naturais 1991 a 2010: volume Brasil.** 2. ed. Florianópolis: Universidade Federal de Santa Catarina; Centro Universitário de Estudos e Pesquisas sobre Desastres, 2012. 126 p. ISBN(9788564695085).

CHARNEY, J. G. Dynamics of deserts and drought in the Sahel. **Quarterly Journal of the Royal Meteorological Society**, v. 101, n. 428, p. 193–202, 1975.

CHEN, F.; KUSAKA, H.; BORNSTEIN, R.; CHING, J.; GRIMMOND, C. S. B.; GROSSMAN-CLARKE, S.; LORIDAN, T.; MANNING, K. W.; MARTILLI, A.; MIAO, S.; SAILOR, D.; SALAMANCA, F. P.; TAHA, H.; TEWARI, M.; WANG, X.; WYSZOGRODZKI, A. A.; ZHANG, C. The integrated WRF/urban modelling system: development, evaluation, and applications to urban environmental problems. **International Journal of Climatology**, v. 31, n. 2, p. 273–288, 2011.

CHEN, F.; MITCHELL, K.; SCHAAKE, J.; XUE, Y.; PAN, H. L.; KOREN, V.; DUAN, Q. Y.; EK, M.; BETTS, A. Modeling of land surface evaporation by four schemes and comparison with FIFE observations. **Journal of Geophysical Research Atmospheres**, v. 101, n. D3, p. 7251–7268, 1996.

CHEN, S. H.; SUN, W. Y. A One-dimensional time dependent cloud model. **Journal of the Meteorological Society of Japan. Ser. II**, v. 80, n. 1, p. 99–118, 2002.

CHOI, I. J.; JIN, E. K.; HAN, J. Y.; KIM, S. Y.; KWON, Y. Sensitivity of diurnal variation in simulated precipitation during East Asian summer monsoon to cumulus parameterization schemes. **Journal of Geophysical Research**, v. 120, n. 23, p. 11,971-11,987, 2015.

COHEN, A. E.; CAVALLO, S. M.; CONIGLIO, M. C.; BROOKS, H. E. A review of planetary boundary layer parameterization schemes and their sensitivity in simulating southeastern U.S. cold season severe weather environments. **Weather and Forecasting**, v. 30, n. 3, p. 591–612, 1 jun. 2015.

CONFEDERAÇÃO NACIONAL DE MUNICÍPIOS (CNM). **Danos e prejuízos causados por desastres no Brasil entre 2013 a 2022**. Brasília. 2022. Available from: <https://www.cnm.org.br/biblioteca/download/15317>.

CORREIA FILHO, W. L. F.; DE OLIVEIRA-JÚNIOR, J. F.; DE BARROS SANTIAGO, D.; DE BODAS TERASSI, P. M.; TEODORO, P. E.; DE GOIS, G.; BLANCO, C. J. C.; DE ALMEIDA SOUZA, P. H.; DA SILVA COSTA, M.; GOMES, H. B.; DOS SANTOS, P. J. Rainfall variability in the Brazilian northeast biomes and their interactions with meteorological systems and ENSO via CHELSA product. **Big Earth Data**, v. 3, n. 4, p. 315–337, 2019.

CRESSMNAN, G. P. An operational objective analysis system. **Monthly Weather Review**, v. 87, n. 10, p. 367–374, 1959.

CRISOLOGO, I.; VULPIANI, G.; ABON, C. C.; DAVID, C. P. C.; BRONSTERT, A.; HEISTERMANN, M. Polarimetric rainfall retrieval from a C-band weather radar in a tropical environment (The Philippines). **Journal of Atmospheric Science**, v. 50, n. S, p. 1976–7633, 2014.

DAI, D.; CHEN, L.; MA, Z.; XU, Z. Evaluation of the WRF physics ensemble using a multivariable integrated evaluation approach over the Haihe river basin in northern China. **Climate Dynamics**, v. 57, n. 1–2, p. 557–575, 2021.

DE MORAIS, M. D. C.; GAN, M. A.; YOSHIDA, M. C. Features of the upper tropospheric cyclonic vortices of Northeast Brazil in life cycle stages. **International Journal of Climatology**, v. 41, n. S1, p. E39–E58, 2021.

DE OLIVEIRA, A. M.; SOUZA, C. T.; DE OLIVEIRA, N. P. M.; MELO, A. K. S.; LOPES, F. J. S.; LANDULFO, E.; ELBERN, H.; HOELZEMANN, J. J. Analysis of atmospheric aerosol optical properties in the northeast brazilian atmosphere with remote sensing data from MODIS and CALIOP/CALIPSO satellites, AERONET photometers and a ground-based Lidar. **Atmosphere**, v. 10, n. 10, p. 594, 2019.

DE SOUZA, D. C.; OYAMA, M. D. Breeze potential along the Brazilian northern and northeastern coast. **Journal of Aerospace Technology and Management**, v. 9, n. 3, p. 368–378, 2017.

DEBORTOLI, N. S.; CAMARINHA, P. I. M.; MARENGO, J. A.; RODRIGUES, R. R. An index of Brazil's vulnerability to expected increases in natural flash flooding and landslide disasters in the context of climate change. **Natural Hazards**, v. 86, n. 2, p. 557–582, 2017.

DOSWELL, C. A. I. The distinction between large-scale and mesoscale contribution to severe convection: a case study example. **Weather and Forecasting**, v. 7, p. 3–16,

1987.

DOSWELL, C. A. I.; BROOKS, H. E.; MADDOX, R. A. Flash flood forecasting : an ingredients-based methodology. **Weather and Forecasting**, v. 11, p. 560–581, 1996.

DUDA, J. D.; GALLUS, W. A. Spring and Summer midwestern severe weather reports in supercells compared to other morphologies. **Weather and Forecasting**, v. 25, n. 1, p. 190–206, 2010.

DUDHIA, J. A multi-layer soil temperature model for MM5. In: PSU/NCAR MESOSCALE MODEL USERS' WORKSHOP, 6., 1996. **Proceedings...** 1996.

DUNN, G. E. Cyclogenesis in the tropical Atlantic. **Bulletin of the American Meteorological Society**, v. 21, n. 6, p. 215–229, 1940.

EMANUEL, K. A.; RAYMOND, D. J. **The representation of cumulus convection in numerical models**. Boston: American Meteorological Society, 1993. v. 46, 246 p. ISBN(978-1-935704-13-3).

ESPINOZA, N. S.; DOS SANTOS, C. A. C.; SILVA, M. T.; GOMES, H. B.; FERREIRA, R. R.; DA SILVA, M. L.; SANTOS E SILVA, C. M.; DE OLIVEIRA, C. P.; MEDEIROS, J.; GIOVANNETTONE, J.; AMARO, V. E.; SANTOS, C. A. G.; MISHRA, M. Landslides triggered by the may 2017 extreme rainfall event in the east coast northeast of Brazil. **Atmosphere**, v. 12, n. 10, 2021.

FABRY, F. **Radar meteorology: principles and practice**. Cambridge: Cambridge University Press, 2015. 272 p. ISBN(978-1-107-07046-2).

FALASCA, S.; GANDOLFI, I.; ARGENTINI, S.; BARNABA, F.; CASASANTA, G.; DI LIBERTO, L.; PETENKO, I.; CURCI, G. Sensitivity of near-surface meteorology to PBL schemes in WRF simulations in a port-industrial area with complex terrain. **Atmospheric Research**, v. 264, 2021.

FEDOROVA, N.; LEVIT, V.; CAMPOS, A. M. V. Brazilian northeast jet stream: association with synoptic-scale systems. **Meteorological Applications**, v. 25, n. 2, p. 261–268, 2018.

FERREIRA, R. N.; SCHUBERT, W. H. Barotropic aspects of ITCZ breakdown. **Journal of the Atmospheric Sciences**, v. 54, n. 2, p. 261–285, 1997.

FIELD, C. B.; BARROS, V.; STOCKER, T. F.; DAHE, Q. (EDS.). **Managing the risks of extreme events and disasters to advance climate change adaptation: special report of the Intergovernmental Panel on Climate Change**. Cambridge: Cambridge University Press, 2012. ISBN(9781107025066).

FLETCHER, C. A. J. **Computational Galerkin methods**. New York: Springer, 1984. 310 p. ISBN(978-3-642-85949-6).

FLETCHER, R. D. The general circulation of the tropical and equatorial atmosphere. **Journal of Meteorology**, v. 2, n. 3, p. 167–174, 1945.

GAO, Y.; LEUNG, L. R.; ZHAO, C.; HAGOS, S. Sensitivity of U.S. summer precipitation to model resolution and convective parameterizations across gray zone resolutions. **Journal of Geophysical Research: Atmospheres**, v. 122, n. 5, p. 2714–2733, 2017.

GETTELMAN, A.; ROOD, R. B. **Demystifying climate models: a users guide to Earth system models**. Heidelberg: Springer, 2016. 282 p. ISBN(978-3-662-48959-8).

GOES-R CALIBRATION WORKING GROUP; GOES-R PROGRAM OFFICE. **NOAA GOES-R series Advanced Baseline Imager (ABI) level 1b radiances**. NOAA National Centers for Environmental Information, 2017. Available from: <https://data.nodc.noaa.gov/cgi-bin/iso?id=gov.noaa.ncdc:C01501>.

GOMES, H. B.; AMBRIZZI, T.; HERDIES, D. L.; HODGES, K.; PONTES DA SILVA, B. F.; LUÍS HERDIES, D.; HODGES, K.; PONTES DA SILVA, B. F. Easterly wave disturbances over Northeast Brazil: an observational analysis. **Advances in Meteorology**, v. 2015, 2015.

GOMES, H. B.; AMBRIZZI, T.; PONTES DA SILVA, B. F.; HODGES, K.; SILVA DIAS, P. L.; HERDIES, D. L.; SILVA, M. C. L.; GOMES, H. B. Climatology of easterly wave disturbances over the tropical South Atlantic. **Climate Dynamics**, v. 53, n. 3–4, p. 1393–1411, 2019.

GRELL, G. A.; DÉVÉNYI, D. A generalized approach to parameterizing convection combining ensemble and data assimilation techniques. **Geophysical Research Letters**, v. 29, n. 14, p. 38–1, 2002.

GRELL, G. A.; FREITAS, S. R. A scale and aerosol aware convective parameterization for weather and air quality modeling. **Atmospheric Chemistry and Physics**, v. 13, p. 23845–23893, 2013.

GRODSKY, S. A.; CARTON, J. A. The intertropical convergence zone in the South Atlantic and the equatorial cold tongue. **Journal of Climate**, v. 16, n. 4, p. 723–733, 2003.

HASTENRATH, S. **Climate dynamics of the tropics updated edition from climate and circulation of the tropics**. [S.l.]: Srpinger, 1991. 57 p. ISBN(978-94-011-3156-8).

HAZRA, A.; CHAUDHARI, H. S.; RANALKAR, M.; CHEN, J. P. Role of interactions between cloud microphysics, dynamics and aerosol in the heavy rainfall event of June 2013 over Uttarakhand, India. **Quarterly Journal of the Royal Meteorological Society**, v. 143, n. 703, p. 986–998, 2017.

HE, J. J.; YU, Y.; YU, L. J.; LIU, N.; ZHAO, S. P. Impacts of uncertainty in land surface information on simulated surface temperature and precipitation over China. **International Journal of Climatology**, v. 37, p. 829–847, 2017.

HEISTERMANN, M.; JACOBI, S.; PFAFF, T. Technical note: an open source library for processing weather radar data (wradlib). **Hydrology and Earth Systems Science,** v. 17, n. 2, p. 863–871, 2013.

HIDALGO NUNES, L. An overview of recent natural disasters in South America. **Text Bulletin des Séances Académie Royale des Scineces d'Outre-Mer**, v. 57, n. 2011, p. 409–425, 2011.

HOLTON, J. R.; HAKIM, G. J. **An introduction to dynamic meteorology**. 5.ed. Oxford: Elsevier, 2013. 551 p.

HONG, S.-Y. Y.; NOH, Y.; DUDHIA, J. A new vertical diffusion package with an explicit treatment of entrainment processes. **Monthly Weather Review**, v. 134, n. 9, p. 2318–2341, 2006.

HONG, S. Y.; LIM, J.-O. J. The WRF Single-Moment 6-Class microphysics scheme (WSM6). **Asia-Pacific Journal of Atmospheric Sciences**, v. 42, n. 2, p. 129–151, 2006.

HORITA, F. E. A.; DE ALBUQUERQUE, J. P.; MARCHEZINI, V. Understanding the decision-making process in disaster risk monitoring and early-warning: a case study within a control room in Brazil. **International Journal of Disaster Risk Reduction**, v. 28, p. 22–31, 2018.

HOUNSOU-GBO, G. A.; SERVAIN, J.; ARAUJO, M.; CANIAUX, G.; BOURLÈS, B.; FONTENELE, D.; MARTINS, E. S. P. R. SST indexes in the tropical South Atlantic for forecasting rainy seasons in Northeast Brazil. **Atmosphere**, v. 10, n. 6, 2019.

HU, X. M.; NIELSEN-GAMMON, J. W.; ZHANG, F. Evaluation of three planetary boundary layer schemes in the WRF model. **Journal of Applied Meteorology and Climatology**, v. 49, n. 9, p. 1831–1844, 2010.

INSTITUTO BRASILEIRO DE GEOGRAFIA E ESTATÍSTICA (IBGE). **População em áreas de risco no Brasil**. Rio de Janeiro, 2018. Available from: <https://biblioteca.ibge.gov.br/visualizacao/livros/liv101589.pdf>.

INSTITUTO BRASILEIRO DE GEOGRAFIA E ESTATÍSTICA (IBGE). **Monitoramento da cobertura e uso da terra do brasil: 2016-2018**. Rio de Janeiro, 2020. Available from: <https://biblioteca.ibge.gov.br/visualizacao/livros/liv101703.pdf>.

JANJIĆ, Z. I. The step-mountain Eta coordinate model: further developments of the convection, viscous sublayer, and turbulence closure schemes. **Monthly Weather Review**, v. 122, n. 5, p. 927–945, 1994.

JEWORREK, J.; WEST, G.; STULL, R. Evaluation of cumulus and microphysics parameterizations in WRF across the convective gray zone. **Weather and Forecasting**, v. 34, n. 4, p. 1097–1115, 2019.

JEWORREK, J.; WEST, G.; STULL, R. WRF precipitation performance and predictability for systematically varied parameterizations over complex terrain. **Weather and Forecasting**, v. 36, n. 3, p. 893–913, 2021.

JIA, W.; ZHANG, X. The role of the planetary boundary layer parameterization schemes on the meteorological and aerosol pollution simulations: a review. **Atmospheric Research**, v. 239, 2020.

JIN, J.; MILLER, N. L.; SCHLEGEL, N. Sensitivity study of four land surface schemes in the WRF model. **Advances in Meteorology**, v. 2010, 2010.

JIRAK, I. L.; COTTON, W. R.; MCANELLY, R. L. Satellite and radar survey of mesoscale convective system development. **Monthly Weather Review**, v. 131, n. 10, p. 2428–2449, 2003.

JORGENSEN, A. P.; WECKWERTH, T. M. Forcing and organization of convective systems. In: WAKIMOTO, R. M.; SRIVASTAVA, R. (Ed.). **Radar and atmospheric science: a collection of essays in honor of David Atlas**. Massachusetts: American Meteorological Society, 2003. p. 75–104.

KAIN, J. S. The Kain–Fritsch convective parameterization: an update. **Journal of Applied Meteorology and Climatology**, v. 43, n. 1, p. 170–181, 2004.

KAIN, J. S.; FRITSCH, J. M. A One-dimensional entraining/detraining plume model and its application in convective parameterization. **Journal of the Atmospheric Sciences**, v. 47, n. 23, p. 2784–2802, 1990.

KAIN, J. S.; FRITSCH, J. M. **Meteorology and atmospheric physics the role of the convective "trigger function" in numerical forecasts of mesoscale convective systems**. [S.l.]: Meteorological Atmospheric Physics, 1992.

KAYANO, M. T. T.; ANDREOLI, R. V. V. O clima da região Nordeste do Brasil. In: CAVALCANTI, I.F.A.; FERREIRA, N. J.; SILVA, M. G. A. J.; DIAS, M. A. F. S. (Ed.). **Tempo e clima no Brasil**. São Paulo: Oficina de textos, 2009. p. 213–233.

KESSLER, E. On the distribution and continuity of water substance in atmospheric circulations. **Meteorological Monographs**, v. 10, n. 32, p. 96, 1969.

KOLODZIEJ HOBSON, A. G.; LAKSHMANAN, V.; SMITH, T. M.; RICHMAN, M. An automated technique to categorize storm type from radar and near-storm environment data. **Atmospheric Research**, v. 111, p. 104–113, 2012.

KOTRONI, V.; LAGOUVARDOS, K. Evaluation of MM5 high-resolution real-time forecasts over the urban area of Athens, Greece. **Journal of Applied Meteorology and Climatology**, v. 43, n. 11, p. 1666–1678, 2004.

KOUADIO, Y. K.; SERVAIN, J.; MACHADO, L. A. T.; LENTINI, C. A. D. Heavy rainfall episodes in the eastern northeast Brazil linked to large-scale ocean-atmosphere conditions in the tropical atlantic. **Advances in Meteorology**, v. 2012, p. 16, 2012.

KOUSKY, V. E. Frontal Influences on Northeast Brazil. **Monthly Weather Review**, v. 107, p. 1140–1153, 1979.

KOUSKY, V. E. Diurnal rainfall variation in northeast Brazil. **Monthly Weather**

Review, v. 108, n. 4, p. 488–498, 1980.

KOUSKY, V. E.; GAN, M. A. Upper tropospheric cyclonic vortices in the tropical South Atlantic. **Tellus**, v. 33, n. 6, p. 538–551, 1981.

KUMAR, S.; BHAT, G. S. Vertical profiles of radar reflectivity factor in intense convective clouds in the tropics. **Journal of Applied Meteorology and Climatology**, v. 55, n. 5, p. 1277–1286, 2016.

KUO, H. L. Further studies of the parameterization of the influence of cumulus convection on large-scale flow. **Journal of the Atmospheric Sciences**, v. 31, n. 5, p. 1232–1240, 1974.

KWON, Y. C.; HONG, S. Y. A Mass-flux cumulus parameterization scheme across gray-zone resolutions. **Monthly Weather Review**, v. 145, n. 2, p. 583–598, 2017.

LI, S.; GAO, Y.; LYU, S.; LIU, Y.; PAN, Y. Response of surface air temperature to the change of leaf area index in the source region of the Yellow River by the WRF model. **Theoretical and Applied Climatology**, v. 138, p. 1755–1765, 2019.

LI, S.; MENG, Z.; WU, N. A preliminary study on the organizational modes of mesoscale convective systems associated with warm-sector heavy rainfall in south China. **Journal of Geophysical Research: Atmospheres**, v. 126, n. 16, 2021.

LI, X.; ZHANG, Q.; XUE, H. The role of initial cloud condensation nuclei concentration in hail using the WRF NSSL 2-moment microphysics scheme. **Advances in Atmospheric Sciences 2017 34:9**, v. 34, n. 9, p. 1106–1120, 2017.

LIBBRECHT, K. G. Crystal growth in the presence of surface melting and impurities: an explanation of snow crystal growth morphologies. 2008. Available from: https://www.its.caltech.edu/~atomic/publist/mobility.pdf.

LIM, K. S. S.; HONG, S. Y. Development of an effective double-moment cloud microphysics scheme with prognostic Cloud Condensation Nuclei (CCN) for weather and climate models. **Monthly Weather Review**, v. 138, n. 5, p. 1587–1612, 2010.

LIU, Y.; CHENG, A.; HU, H. Precipitation simulation from the cumulus convection parameterization schemes based on the WRF model in the Weihe River Basin, China. **Journal of Physics: Conference Series**, v. 2006, n. 1, e012004, 2021.

LÓPEZ-BRAVO, C.; CAETANO, E.; MAGAÑA, V. Forecasting summertime surface temperature and precipitation in the Mexico city metropolitan area: sensitivity of the wrf model to land cover changes. **Frontiers in Earth Science**, v. 6, p. 1–14, 2018.

LOVELAND, T. R.; REED, B. C.; BROWN, J. F.; OHLEN, D. O.; ZHU, Z.; YANG, L.; MERCHANT, J. W. Development of a global land cover characteristics database and IGBP DISCover from 1 km AVHRR data. **International Journal of Remote Sensing**, v. 21, n. 7, p. 1303–1330, 2000.

LU, J.; FENG, T.; LI, J.; CAI, Z.; XU, X.; LI, L.; LI, J. Impact of assimilating

Himawari-8-derived layered precipitable water with varying cumulus and microphysics parameterization schemes on the simulation of Typhoon Hato. **Journal of Geophysical Research: Atmospheres**, v. 124, n. 6, p. 3050–3071, 2019.

LUIZA, A.; NETTO, C.; SATO, A. M.; SOUZA, A.; VIANNA, L. G. G.; ARAÚJO, I. S.; DAVID, L. C.; LIMA, P. H.; SILVA, A. P. A.; SILVA, R. P. Landslide science and practice. **Landslide Science and Practice**, 2013.

MAHBUB ALAM, M. Impact of cloud microphysics and cumulus parameterization on simulation of heavy rainfall event during 7-9 October 2007 over Bangladesh. **Journal of Earth System Science**, v. 123, n. 2, p. 259–279, 2014.

MANSELL, E. R.; ZIEGLER, C. L.; BRUNING, E. C. Simulated electrification of a small thunderstorm with two-moment bulk microphysics. **Journal of the Atmospheric Sciences**, v. 67, n. 1, p. 171–194, 2010.

MARCHEZINI, V.; HORITA, F. E. A.; MATSUO, P. M.; TRAJBER, R.; TREJO-RANGEL, M. A.; OLIVATO, D. A review of studies on participatory early warning systems (P-EWS): pathways to support citizen science initiatives. **Frontiers in Earth Science**, v. 6, p. 184, 2018.

MARENGO, J. A.; CAMARINHA, P. I.; ALVES, L. M.; DINIZ, F.; BETTS, R. A. Extreme rainfall and hydro-geo-meteorological disaster risk in 1.5, 2.0, and 4.0°C global warming scenarios: an analysis for Brazil. **Frontiers in Climate**, v. 3, 2021.

MARENGO, J. A.; ESPINOZA, J. C. Extreme seasonal droughts and floods in Amazonia: causes, trends and impacts. **International Journal of Climatology**, v. 36, n. 3, p. 1033–1050, 2016.

MARENGO, J. A.; TOMASELLA, J.; SOARES, W. R.; ALVES, L. M.; NOBRE, C. A. Extreme climatic events in the Amazon basin. **Theoretical and Applied Climatology**, v. 107, n. 1–2, p. 73–85, 2012.

MARKOWSKI, P.; RICHARDSON, Y. **Mesoscale meteorology in midlatitudes**. Chichester: [s.n.], .2010. 407 p. ISBN(9780470742136).

MARWITZ, J. D. The structure and motion of severe hailstorms. Part I: supercell storms. **Journal of Applied Meteorology and Climatology**, v. 11, p. 166–179, 1972a.

MARWITZ, J. D. The structure and motion of severe hailstorms. Part II: multi-cell storms. **Journal of Applied Meteorology and Climatology**, v. 11, p. 180–188, 1972b.

MARWITZ, J. D. The structure and motion of severe hailstorms. Part III: severely sheared storms. **Journal of Applied Meteorology and Climatology**, v. 11, p. 189–201, 1972c.

MATIAS RIBEIRO, M. S.; DE MELO BARBOSA ANDRADE, L.; CONSTANTINO SPYRIDES, M. H.; LIMA, K. C.; EVANGELISTA DA SILVA, P.; BATISTA, D. T.; RODRIGUES DE LARA, I. A.; RIBEIRO, M. S. M.; ANDRADE, L. D. M. B.; SPYRIDES, M. H. C.; LIMA, K. C.; DA SILVA, P. E.; BATISTA, D. T.; DE LARA, I.

A. R. Environmental disasters in northeast Brazil: hydrometeorological, social, and sanitary factors. **Weather, Climate, and Society**, v. 13, n. 3, p. 541–554, 2021.

MELO, A. B. C.; CAVALCANTI, I. F. A. A.; SOUZA, P. P. Zona de Convergência Intertropical do Atlântico. In: CAVALCANTI, I. F. A.; FERREIRA, N. J.; SILVA, M. G. A.; DIAS, M. A. F. S. (Ed.). **Tempo e clima no Brasil**. São Paulo: Oficina de textos, 2009. p. 25–41.

MERINO, A.; GARCÍA-ORTEGA, E.; NAVARRO, A.; SÁNCHEZ, J. L.; TAPIADOR, F. J. WRF hourly evaluation for extreme precipitation events. **Atmospheric Research**, v. 274, e106215, 2022.

METODIEV, D.; ANDRADE, M. R. M.; MENDES, R. M.; MORAES, M. A. E.; KONIG, T.; BORTOLOZO, C. A.; BERNARDES, T.; LUIZ, R. A. F.; COELHO, J. O. M. Correlation between rainfall and mass movements in north coast region of Sao Paulo State, Brazil for 2014-2018. **International Journal of Geosciences**, v. 9, n. 12, p. 669–679, 2018.

MEYERS, M. P.; WALKO, R. L.; HARRINGTON, J. Y.; COTTON, W. R. New RAMS cloud microphysics parameterization. Part II: the two-moment scheme. **Atmospheric Research**, v. 45, n. 1, p. 3–39, 1997.

MOLION, L. C. B.; BERNARDO, S. DE O. Uma revisão da dinâmica das chuvas no Nordeste Brasileiro. **Revista Brasileira de Meteorologia**, v. 17, n. 1, p. 1–10, 2002.

MORRISON, H.; MILBRANDT, J. A. Parameterization of cloud microphysics based on the prediction of bulk ice particle properties. Part I: scheme description and idealized tests. **Journal of the Atmospheric Sciences**, v. 72, n. 1, p. 287–311, 2015.

MORRISON, H.; THOMPSON, G.; TATARSKII, V. Impact of cloud microphysics on the development of trailing stratiform precipitation in a simulated squall line: comparison of one- and two-moment schemes. **Monthly Weather Review**, v. 137, n. 3, p. 991–1007, 2009.

MOURA, A. D.; SHUKLA, J. On the dynamics of droughts in northeast Brazil: observations, theory and numerical experiments with a general circulation model. **Journal of the Atmospheric Sciences**, v. 38, p. 2653–2675, 1981.

MU, Z.; ZHOU, Y.; PENG, L.; HE, Y. Numerical rainfall simulation of different WRF parameterization schemes with different spatiotemporal rainfall evenness levels in the Ili region. **Water**, v. 11, n. 12, 2019.

NAKANISHI, M.; NIINO, H. Development of an improved turbulence closure model for the atmospheric boundary layer. **Journal of the Meteorological Society of Japan Serie II**, v. 87, n. 5, p. 895–912, 2009.

NATIONAL CENTERS FOR ENVIRONMENTAL PREDICTION (NCEP). **NCEP GFS 0.25 degree global forecast grids historical archive**. Boulder, CO. 2015. Available from: <https://doi.org/10.5065/D65D8PWK>.

NELCI COMIN, A.; JUSTINO, F.; PEZZI, L.; DIEGO DE SOUSA GURJÃO, C.; SHUMACHER, V.; FERNÁNDEZ, A.; ADRIANO SUTIL, U. Extreme rainfall event in the Northeast coast of Brazil: a numerical sensitivity study. **Meteorology and Atmospheric Physics**, v. 133, p. 141–162, 2021.

NIU, G. Y.; YANG, Z. L.; MITCHELL, K. E.; CHEN, F.; EK, M. B.; BARLAGE, M.; KUMAR, A.; MANNING, K.; NIYOGI, D.; ROSERO, E.; TEWARI, M.; XIA, Y. The community Noah land surface model with multiparameterization options (Noah-MP): 1. model description and evaluation with local-scale measurements. **Journal of Geophysical Research: Atmospheres**, v. 116, n. D12, p. 12109, 2011.

OLIVEIRA, P. T.; SANTOS E SILVA, C. M.; LIMA, K. C. Climatology and trend analysis of extreme precipitation in subregions of Northeast Brazil. **Theoretical and Applied Climatology**, v. 130, n. 1–2, p. 77–90, 2017.

ON, N.; KIM, H. M.; KIM, S. Effects of resolution, cumulus parameterization scheme, and probability forecasting on precipitation forecasts in a high-resolution limited-area ensemble prediction system. **Asia-Pacific Journal of Atmospheric Sciences**, v. 54, p. 623–637, 2018.

PARKER, M. D.; JOHNSON, R. H. Organizational modes of midlatitude mesoscale convective systems. **Monthly Weather Review**, v. 128, n. 10, p. 3413–3436, 2000.

PLEIM, J. E. A combined local and nonlocal closure model for the atmospheric boundary layer. Part I: model description and testing. **Journal of Applied Meteorology and Climatology**, v. 46, n. 9, p. 1383–1395, 2007.

POLAND NICOLODI, J. L.; PETTERMANN, R. M. Vulnerability of the Brazilian coastal zone in its environmental, social, and technological aspects. **Journal of Coastal Research SI**, v. 64, p. 1372–1379, 2011.

POLETTI, M. L.; PARODI, A.; TURATO, B. Severe hydrometeorological events in Liguria region: calibration and validation of a meteorological indices-based forecasting operational tool. **Meteorological Applications**, v. 24, n. 4, p. 560–570, 2017.

RAO, V. B.; DE LIMA, M. C.; FRANCHITO, S. H. Seasonal and interannual variations of rainfall over eastern northeast Brazil. **Journal of Climate**, v. 6, n. 9, p. 1754–1763, 1993.

RAO, V. B.; MARQUES, V. S. Water vapor characteristics over northeast Brazil during two contrasting years. **Journal of Climate and Applied Meteorology**, v. 23, p. 440–444, 1984.

REBOITA, M. S.; AMBRIZZI, T.; SILVA, B. A.; PINHEIRO, R. F.; DA ROCHA, R. P. The south atlantic subtropical anticyclone: present and future climate. **Frontiers in Earth Science**, v. 7, p. 1–15, 2019.

REBOITA, M. S.; RODRIGUES, M.; PEREIRA, R. A.; FREITAS, C.; MARTINS, D.; MILLER, G. Causas da semi-aridez do sertão nordestino. **Revista Brasileira de Climatologia**, v. 19, n. 12, p. 254–277, 2016.

RITCHIE, H.; ROSER, M. Natural disasters. **Our World in Data**, 2014.

ROGERS, E.; BLACK, T.; FERRIER, B.; LIN, Y.; PARRISH, D.; DIMEGO, G. Changes to the NCEP meso Eta analysis and forecast system: increase in resolution, new cloud microphysics, modified precipitation assimilation, modified 3DVAR analysis. **NWS Technical Procedures Bulletin**, v. 488, p. 1–15, 2001.

ROLPH, G.; STEIN, A.; STUNDER, B. Real-time Environmental Applications and Display sYstem: READY. **Environmental Modelling & Software**, v. 95, p. 210–228, 2017.

SHERBURN, K. D.; PARKER, M. D. Climatology and ingredients of significant severe convection in high-shear, low-CAPE environments. **Weather and Forecasting**, v. 29, n. 4, p. 854–877, 2014.

SHIMIZU, M. H.; ANOCHI, J. A.; KAYANO, · M T. Precipitation patterns over northern Brazil basins: climatology, trends, and associated mechanisms. **Theoretical and Applied Climatology**, v. 1, p. 3, 2022.

SHIN, H. H.; HONG, S. Y. Representation of the subgrid-scale turbulent transport in convective boundary layers at gray-zone resolutions. **Monthly Weather Review**, v. 143, n. 1, p. 250–271, 2015.

SILVA DIAS, P. L. DA. **Smaller scale convergence patterns in the NEB** [personal communication]. Message received by Saulo Barros Costa on November 11, 2022.

SKAMAROCK, W. C.; KLEMP, J. B.; DUDHIA, J.; GILL, D. O.; LIU, Z.; BERNER, J.; WANG, W.; POWERS, J. G.; DUDA, M. G.; BARKER, D. M.; HUANG, X.-Y. **A description of the advanced research WRF model version 4**. Boulder: National Center for Atmospheric Research, 2019. Available from: <https://www2.mmm.ucar.edu/wrf/users/docs/technote/v4_technote.pdf>.

SMITHSON, P. A. IPCC, 2001: climate change 2001: the scientific basis. **International Journal of Climatology**, v. 22, n. 9, e1144, 2002.

SOUZA DOS REIS, J.; WEBER, ·; GONÇALVES, A.; MENDES, D. Climatology of the dynamic and thermodynamic features of upper tropospheric cyclonic vortices in Northeast Brazil. **Climate Dynamics**, v. 57, p. 3413–3431, 2021.

STEIN, A. F.; DRAXLER, R. R.; ROLPH, G. D.; STUNDER, B. J. B.; COHEN, M. D.; NGAN, F. NOAA's HYSPLIT Atmospheric transport and dispersion modeling system. **Bulletin of the American Meteorological Society**, v. 96, n. 12, p. 2059–2077, 2015.

STENSRUD, D. J. **Parametrization schemes: keys to understanding numerical weather prediction models**. Cambridge: Cambridge University Press, 2007. 480 p. ISBN(978-0-521-86540-1).

STERGIOU, I.; TAGARIS, E.; SOTIROPOULOU, R.-E. P. Sensitivity asessment of WRF parameterizations over Europe. **Proceedings 2017,** v. 1, n. 5, p. 119, 2017.

STULL, R. B. **An introduction to boundary layer meteorology**. Berlin: Springer, 1988. 670 p. ISBN(978-90-277-2768-8).

STULL, R. B. Static stability: an update. **Bulletin - American Meteorological Society**, v. 72, n. 10, p. 1521–1529, 1991.

SUKORIANSKY, S.; GALPERIN, B.; PEROV, V. Application of a new spectral theory of stably stratified turbulence to the atmospheric boundary layer over sea ice. **Boundary-Layer Meteorology**, v. 117, n. 2, p. 231–257, 2005.

SUN, J.; ARIYA, P. A. Atmospheric organic and bio-aerosols as cloud condensation nuclei (CCN): A review. **Atmospheric Environment**, v. 40, n. 5, p. 795–820, 2006.

TAPIADOR, F. J.; TAO, W. K.; SHI, J. J.; ANGELIS, C. F.; MARTINEZ, M. A.; MARCOS, C.; RODRIGUEZ, A.; HOU, A. A comparison of perturbed initial conditions and multiphysics ensembles in a severe weather episode in Spain. **Journal of Applied Meteorology and Climatology**, v. 51, n. 3, p. 489–504, 2012.

TASZAREK, M.; ALLEN, J. T.; BROOKS, H. E.; PILGUJ, N.; CZERNECKI, B. Environments in a Warming Climate. **Bulletin of the American Meteorological Society**, v. 102, n. 2, p. 296–322, 2021.

TAYLOR, K. E. Summarizing multiple aspects of model performance in a single diagram. **Journal of Geophysical Research**, v. 106, n. D7, 2001.

TEWARI, M.; CHEN, F.; WANG, W.; DUDHIA, J.; LEMONE, M. A.; MITCHELL, K.; EK, M.; GAYNO, G.; WEGIEL, J.; CUENCA, R. H. Implementation and verification of the unified NOAH land surface model in the WRF model. In: CONFERENCE ON WEATHER ANALYSIS AND FORECASTING, 20; CONFERENCE ON NUMERICAL WEATHER PREDICTION, 16., 2004. **Proceedings...** Bulletin of the American Meteorological Society, 2004.

THOMPSON, G.; EIDHAMMER, T. A study of aerosol impacts on clouds and precipitation development in a large winter cyclone. **Journal of the Atmospheric Sciences**, v. 71, n. 10, p. 3636–3658, 2014.

THOMPSON, G.; FIELD, P. R.; RASMUSSEN, R. M.; HALL, W. D. Explicit forecasts of winter precipitation using an improved bulk microphysics scheme. Part II: implementation of a new snow parameterization. **Monthly Weather Review**, v. 136, n. 12, p. 5095–5115, 2008.

TORO, J.; MATERA, M.; MOURA, F. S.; PEDROSO, F. F. (Ed.). **Coping with losses : options for disaster risk financing in Brazil**. Washington: The World Bank, 2014. 86 p.

TORRES, R. R.; FERREIRA, N. J. Case studies of easterly wave disturbances over Northeast Brazil using the Eta Model. **Weather and Forecasting**, v. 26, n. 2, p. 225–235, 2011.

UNITED NATIONS OFFICE FOR DISASTER RISK REDUCTION (UNDRR).

Disaster risk reduction in the United Nations: roles, mandates and results of key UN entities. Geneva. 2013. Available from: <http://www.unisdr.org/files/32918_drrintheun2013.pdf>.

UTIDA, G.; CRUZ, F. W.; ETOURNEAU, J.; BOULOUBASSI, I.; SCHEFUSS, E.; VUILLE, M.; NOVELLO, V. F.; PRADO, L. F.; SIFEDDINE, A.; KLEIN, V.; ZULAR, A.; VIANA, J. C. C.; TURCQ, B. Tropical South Atlantic influence on northeastern Brazil precipitation and ITCZ displacement during the past 2300 years. **Nature Scientific Reports**, v. 9, n. 1698, p. 8, 2019.

UVO, C. B.; REPELLI, C. A.; ZEBIAK, S. E.; KUSHNIR, Y. The relationships between tropical Pacific and Atlantic SST and northeast Brazil monthly precipitation. **Journal of Climate**, v. 11, n. 4, p. 551–562, 1998.

WAGNER, A.; HEINZELLER, D.; WAGNER, S.; RUMMLER, T.; KUNSTMANN, H. Explicit convection and scale-aware cumulus parameterizations: high-resolution simulations over areas of different topography in Germany. **Monthly Weather Review**, v. 146, n. 6, p. 1925–1944, 2018.

WALISER, D. E.; GAUTIER, C. A Satellite-derived Climatology of the ITCZ. **Journal of Climate**, v. 6, p. 2162–2174, 1993.

WANG, W.; SHEN, X.; HUANG, W. A comparison of boundary-layer characteristics simulated using different parametrization schemes. **Boundary-Layer Meteorology**, v. 161, n. 2, p. 375–403, 2016.

WESTERMAYER, A. T.; GROENEMEIJER, P.; PISTOTNIK, G.; SAUSEN, R.; FAUST, E. Identification of favorable environments for thunderstorms in reanalysis data. **Meteorologische Zeitschrift**, v. 26, n. 1, p. 59–70, 2017.

WONG, M.; ROMINE, G.; SNYDER, C. Model improvement via systematic investigation of physics tendencies. **Monthly Weather Review**, v. 148, n. 2, p. 671–688, 2020.

WORLD METEOROLOGICAL ORGANIZATION (WMO). **Guidelines for implementation of Common Alerting Protocol (CAP): enabled emergency alerting**. Geneva. 2013. Available from: <https://library.wmo.int/doc_num.php?explnum_id=3431>.

ZHANG, C.; WANG, Y. Projected future changes of tropical cyclone activity over the western north and south Pacific in a 20-km-Mesh regional climate model. **Journal of Climate**, v. 30, n. 15, p. 5923–5941, 2017.

ZHANG, C.; WANG, Y.; HAMILTON, K. Improved representation of boundary layer clouds over the southeast Pacific in ARW-WRF using a modified tiedtke cumulus parameterization scheme. **Monthly Weather Review**, v. 139, n. 11, p. 3489–3513, 2011.

ZHANG, X.; BAO, J. W.; CHEN, B.; GRELL, E. D. A three-dimensional scale-adaptive turbulent kinetic energy scheme in the WRF-ARW model. **Monthly Weather**

Review, v. 146, n. 7, p. 2023–2045, 2018.

ZHOU, L.; LIN, S. J.; CHEN, J. H.; HARRIS, L. M.; CHEN, X.; REES, S. L. Toward convective-sale prediction within the next generation global prediction system. **Bulletin of the American Meteorological Society**, v. 100, n. 7, p. 1225–1243, 2019.

GLOSSARY

Some terms commonly used in natural disasters

Alert/warning	A tool indicating that the disaster risk situation is predictable in the short term.
Capacity	The combination of all the strengths, attributes and resources available within an organization, community or society to manage and reduce disaster risks and strengthen resilience.
Disaster risk	The potential loss of life, injury, or destroyed or damaged assets which could occur to a system, society or a community in a specific period of time, determined probabilistically as a function of hazard, exposure, vulnerability and capacity.
Exposure	The situation of people, infrastructure, housing, production capacities and other tangible human assets located in hazard-prone areas.
Hazard	A potentially damaging physical event, phenomenon or human activity that may cause the loss of life or injury, property damage, social and economic disruption or environmental degradation.
Occurrence records	When it is confirmed that the warned severe weather system has generated some kind of social or physical disturbance.
Resilience	The ability of a system, community or society exposed to hazards to resist, absorb, accommodate to and recover from the effects of a hazard in a timely and efficient manner, including through the preservation and restoration of its essential basic structures and functions
Vulnerability	The conditions determined by physical, social, economic and environmental factors or processes, which increase the susceptibility of a community to the impact of hazards.

APPENDIX A - SEVERE RAINFALL EVENTS STUDIED

Synthesis of the synoptic and mesoscale, rainfall and radar characteristics for the cases studied. "N° cities" is the number of municipalities affected by the natural disaster; "Type" refers to the main mechanism for system formation identified; "MRR" is the maximum rain rate (mm/10min); "Total rainfall" is the highest accumulated rainfall recorded in a rain gauge; "Total time" is the total rain duration; "Rain type" is the temporal classification of rainfall; "Max dBZ" is the highest observed reflectivity; and "Radar type" is the classification according to the observed reflectivity cells.

Event	N° cities	Type	MRR	Total rainfall	Total time	Rain type	Max dBZ	Radar type
20170303 (a)	2	HPS+	20	115	21	CT	48	UNI
20170412 (b)	2	HPS+	12	107	24	SO	48	MULT
20170507 (c)	1	HPS+	9	72	30	SO	42	UNI
20170524 (d)	10	HPS+	10	137	21	CT	48	UNI+
20170527 (e)	16	HPS	10	366	48	CT	42	MULT
20170614 (f)	2	EWD	8	193	204	SO	42	UNI+
20170623 (g)	1	HPS	11	95	36	SO	35	MULT
20170627 (h)	5	HLF	14	130	48	CT	56	UNI+
20170719 (i)	17	MLF	23	264	72	CT	48	UNI+
20170724 (j)	1	MLF	9	110	98	SO	36	MULT
20180118 (k)	4	HPS	14	84	17	SO	48	UNI+
20180217 (l)	4	HLF+	15	181	56	SO	48	MULT
20180306 (m)	1	HPS	15	75	15	CT	56	MULT
20180405 (n)	1	UTCV	20	142	41	SO	50	MULT
20180410 (o)	1	ITCZ	10	99	17	SO	48	UNI+
20180412 (p)	1	HPS+	14	78	42	SO	48	MULT
20180421 (q)	5	ITCZ	13	193	84	SO	56	UNI+
20190203 (r)	1	ITCZ+	20	143	14	SO	56	MULT
20190205 (s)	2	ITCZ+	17	82	39	SO	56	MULT
20190412 (t)	4	ITCZ	21	93	15	CT	60	UNI+
20190527 (u)	2	HPS	16	224	44	SO	56	MULT
20190612 (v)	7	MLF	18	237	54	CT	48	UNI+
20190614 (w)	3	HPS	9	179	93	CT	36	UNI
20190801 (x)	1	HPS	5	108	45	CT	42	MULT

HPS – high pressure on the surface, HPS+ – high pressure on the surface associated with another mechanism, HLF – high-level flow, MLF – medium-level flow, CT – continuous, SO – spaced out, UNI – single-celled isolated nuclei, UNI+ – large-single-celled nucleus plus small cells, MULT – small multicellular nuclei.

APPENDIX B – FIRST SCIENTIFIC PAPER PUBLISHED

https://doi.org/10.3390/w14193135

water

MDPI

Article

Extreme Precipitation Events on the East Coast of Brazil's Northeast: Numerical and Diagnostic Analysis

Saulo Barros Costa [1,2], Dirceu Luís Herdies [1,*] and Diego Oliveira de Souza [2]

[1] National Institute for Space Research, Cachoeira Paulista 12630-000, Brazil
[2] National Center for Monitoring and Early Warning of Natural Disasters, São José dos Campos 12247-016, Brazil
* Correspondence: dirceu.herdies@inpe.br

Abstract: The Northeast of Brazil (NEB) is the region with the highest number of municipal decrees of emergency situation declaration caused by weather events in the period from 2013 to 2022 and with the highest rate of natural disasters per risk area. In the NEB, the city of Recife and its metropolitan region are the biggest localities with populations in risk areas. Focusing on this region, five events of extreme precipitation were chosen for simulations using the WRF model and diagnostics analyses. First, a set of configurations of the model was tested, including 11 microphysics (MPH) schemes, 9 planetary boundary layer (PBL) schemes, 5 cumulus (CUM), and 7 surface layer (SFC) schemes. Then, through diagnostic analysis, the conditional instability, the moisture supply at low levels, and the support of the medium and high levels in storm formation were verified. The model's configurations were verified by 298 rain gauges with hourly registrations through statistical metrics such as bias, MSE, standard deviation, and Pearson's correlation, and demonstrated that the MPH schemes of Thompson Aerosol-Aware and NSSL + CCM, ACM2, MYJ for the PBL, KFCuP for CUM, and RUC for SFC were considered the best. All the cases were better with CUM parametrizations turned on. In all cases, diagnostics analyses highlighted the strong moisture flux convergence at the low levels, the presence of wind shear on the middle layer, weak cyclonic vorticity advection at high levels, and CAPE values around 1500 J/kg, in addition to an inverse relationship between wind shear action and CAPE values. This work is part of the national strategy for monitoring, diagnosis, and modeling of information that can minimize or even prevent damage caused by severe precipitation events.

Keywords: WRF configurations; weather analyses; natural disasters

Citation: Costa, S.B.; Herdies, D.L.; Souza, D.O. d. Extreme Precipitation Events on the East Coast of Brazil's Northeast: Numerical and Diagnostic Analysis. *Water* 2022, *14*, 3135. https://doi.org/10.3390/w14193135

Academic Editor: Guido Paliaga

Received: 17 August 2022
Accepted: 30 September 2022
Published: 4 October 2022

Publisher's Note: MDPI stays neutral with regard to jurisdictional claims in published maps and institutional affiliations.

1. Introduction

The history of socioeconomic development of Brazil is characterized by different uses of land and different patterns of land occupation, revealing a heterogeneous population distribution. This disorderly occupation when exposed to natural climate variability and the natural susceptibility of the regions leads to landslides and floods [1], which are disasters that cause the maximum number of deaths in Brazil [2]. Numerous studies have investigated the occurrence of floods, flash floods, and landslides triggered by severe weather events delivering large amounts of rainfall [3–8]. Extreme hydrometeorological events, responsible for large amounts of precipitation, have become more frequent and intense in recent decades [9]. Extreme events are also components of natural climate variability, and their periodicity and intensity, whether natural or induced by human activities, may change [10]. Such phenomena can impact society, causing natural disasters, depending on site vulnerabilities.

To respond to the growing number of natural disasters, the Brazilian government has implemented the National Plan for Risk Management and Disaster Response [11]. Following a dialogue among the three spheres of public administration (federal, state, and

APPENDIX C – SECOND SCIENTIFIC PAPER (SUBMITTED)

Weather and Climate Extremes

Extreme precipitation events on the east coast of Brazil's Northeast: an observational analysis

--Manuscript Draft--

Manuscript Number:	WACE-D-22-00267
Article Type:	VSI: moisture transport
Keywords:	natural disasters; severe weather; radar; gauge analysis
Corresponding Author:	Dirceu Luis Herdies, Ph.D. National Institute for Space Research Weather Forecast and Climate Studies Centre BRAZIL
First Author:	Saulo Barros Costa, M.Sc.
Order of Authors:	Saulo Barros Costa, M.Sc.
	Dirceu Luis Herdies, Ph.D.
Abstract:	Three years of natural disaster alert issuance data, 2017 to 2019, were used to analyze and characterize severe rainfall events in the eastern state of Pernambuco/Brazil. The analyses were performed using GOES-16 satellite data, GFS/NCEP model data with 0.25-degree resolution, radar data and data from 298 rainfall stations in the region. The warnings were concentrated during the rainy season and in a narrow coastal belt. The main systems responsible for the heavy precipitation were the ITCZ and a high pressure on the surface responsible for blocking the trade winds and favoring convection. Small-sized multicells were the type of radar reflectivity core that caused the most as well as systems lasting longer than 24 h and with heavy precipitation.